Novel approaches to plasmonic enhancement applications: upconverters, 2D materials and tweezers

by

Mirali Seyed Shariatdoust

B.Sc., University of Tabriz, 2013

M.Sc., Sharif University of Technology, 2015

A Dissertation Submitted in Partial Fulfillment of the

Requirements for the Degree of

DOCTOR OF PHILOSOPHY

in the Department of Electrical Engineering and Computer Sciences

University of Victoria

Novel approaches to plasmonic enhancement applications: upconverters, 2D materials and tweezers

by

Mirali Seyed Shariatdoust

B.Sc., University of Tabriz, 2013

M.Sc., Sharif University of Technology, 2015

Supervisory Committee

Dr. Reuven Gordon , Supervisor

(Department of Electrical Engineering and Computer Sciences)

Dr. Makhsud Saidaminov, Departmental Member

(Department of Electrical Engineering and Computer Sciences)

Dr. Mohsen Akbari, Outside Member

(Department of Mechanical Engineering)

Abstract

In this thesis, the local field enhancement from multiple plasmonic structures were studied in different experiments. A new approach was applied to enhance the emission from upconverting nanoparticles to harvest energy from photons below the bandgap. A novel nanofabrication method was introduced to make double nanoholes for use in optical trapping, which was implemented to observe the nonlinear response from 2D materials and the enhanced emission from upconverting single nanoparticles. This method makes a large amount of apertures and is inexpensive. Selective plasmon-enhanced emission from erbium-doped nanoparticles using gold nanorods was demonstrated. Upconversion nanoparticles were excited with a dual-wavelength source of 1520 nm and 1210 nm simultaneously. The power dependence of the observed upconversion emission confirmed the contribution of both excitation bands in the upconversion process. Gold nanorods with resonances at 980 nm and 808 nm were implemented to selectively enhance the upconversion emission in order to harvest light with Si and GaAs solar cells, respectively. I also used colloidal lithography to fabricate double nanoholes which were plasmonic structures used for protein and nanoparticle trapping. This bottom-up technique enabled the fabrication of a large number of structures at low cost. Plasma etching of polystyrene nanoparticles using this technique tuned the cusp separation of double nanoholes down to 10 nm. The smaller cups separation enables to have more confined field in the gap which can be used in plasmonic sensing and plasmon enhanced upconversion processes. This technique

can be used to fabricate plasmonic structures for nanoparticle trapping, spectroscopy, and sensing. In the next project, hexagonal boron nitride nanoflakes were trapped in a double nanohole fabricated with the colloidal lithography method. A second harmonic signal was detected at 486.5 nm where the particle was trapped and pumped with an ultra-low power laser at 973 nm. The power dependence measurements supported the second order process for second harmonic generation. Finite-difference time-domain (FDTD) simulations showed a 500-fold field intensity enhancement at the fundamental wavelength and a 450-fold enhancement in the Purcell factor at the second harmonic generation wavelength. This scheme is promising for ultra-fast imaging nonlinear optics technologies. In the last project, colloidal lithography double nanoholes were used to trap upconverting nanocrystals. Colloidal lithography double nanoholes with 32 nm cusp separation achieved 50 times larger emission compared to rectangular apertures. FDTD simulations showed the largest field enhancement in the aperture with the largest upconversion enhancement. 1550 nm emission from the trapped nanoparticle can be used as single-photon source.

Table of Contents

List of Figures

ACKNOWLEDGEMENTS

I would like to express my gratitude to my supervisor, Prof. Reuven Gordon, for his support, and mentoring. His dedication and availability throughout my Ph.D. studies were beyond helpful. I would also like to thank my supervisory committee, Dr. Mohsen Akbari and Dr. Makhsud Saidaminov for their help in shaping my dissertation path.

I would also like thank all of my peers in the nanoplasmonics lab for their valuable encouragement and suggestions during my Ph.D. especially Dr. Ali Khademi, Dr. Ghazal Hajisalem, Adarsh Lalitha Ravindranath, Elham Babaei, Ryan Peck, Jeffrey Mark Burkhartsmeyer, and Michael Dobinson.

Last but not least, I would like thank my wonderful family for their support and motivation.

DEDICATION

To my wonderful family

Glossary

Common Abbreviations

Abbreviation	Meaning
APD	avalanche photodiode
BE	beam expander
BPF	bandpass filter
CCD	charge-coupled device
CW	continuous wave
DNH	double nanohole
EBL	electron beam lithography
EM	electromanetic
FDTD	finite-difference time-domain
FIB	focused ion beam
HWP	half-wave plate
LP	linear polarizer
LSP	localized surface plasmon
LPF	longpass filter
MO	microscope objective
ODF	optical density filter
OI	oil immersion
PBC	periodic boundary condition
PEC	perfect electric conductor
PMC	perfect magnetic conductor
PML	perfectly matched layer
SEM	scanning electron microscope
SHG	second harmonic generation
SPF	shortpass filter
SPP	surface plasmon polariton
TFSF	total-filed scattered-field
UCNC	upconversion nanocrystal
UCNP	upconversion nanoparticle

Glossary

Common Abbreviations

Symbols	Meaning
β	propagation constant
γ	transition rate
γ_{rad}	radiative decay
γ_{nonrad}	nonradiative decay
Γ	reflection
ϵ_0	vacuum permittivity
ϵ_d	dielectric permittivity
ϵ_m	metal permittivity
η	quantum yield
Φ	phase of reflection
λ	wavelength
ρ	electron density
ω	angular frequency

Chapter 1

Introduction

In this thesis, a novel method to fabricate double nanohole structures was achieved using colloidal lithography. Implementing this technique opened a new avenue for preparing double nanohole (DNH) plasmonic structures with cusp separations down to 10 nm in an inexpensive way. Obtaining these structures provided the opportunity to look at the light-matter interaction using an optical trapping setup. Many particles and proteins like polystyrene beads, bovine serum albumin (BSA) and rubisco were trapped. Nonlinear responses from 2D materials were studied using the fabricated structures and their field enhancement were analyzed using numerical simulations. A similar investigation was performed for upconverting nanocrystals. In another separate work, gold nanorods were used to enhance the upconversion emission from upconversion nanoparticles (UCNPs) when they were pumped with dual solar bands, which silicon and GaAs solar cells were not able to harvest.

1.1 Motivation

The interaction between light and a metal enables the electromagnetic field to be confined in a sub-wavelength volume where the metal is fabricated. Electromagnetic (EM) waves can couple to free electrons of a metal. While the propagating excitation of an electron plasma at the interface of a metal and an insulator is known as surface plasmon polaritons (SPP), localized surface plasmons (LSP) are defined as non-propagating excited free electrons of a metal. Knowing the physics behind plasmonics allows us to design nanosturctures that confine EM fields in a nanoscale region which permits the investigation of nonlinear properties of materials, emission enhancement, and trapping single-digit nanometer particles in size, to name a few [1]. Plasmonic structures are fabricated using techniques such as focused ion beam (FIB) milling and are used for trapping and characterizing dielectric nanoparticles since they can increase the gradient force during trapping by the self-induced back action technique [2, 3, 4, 5, 6, 7]. However, fabricating nanostructures like double nanoholes using previous techniques can be time consuming and are expensive. In this Ph.D. dissertation, I demonstrate a new colloidal lithography technique accompanied with plasma etching that can be used to fabricate numerous double nanoholes and control aperture size and cusp separation to trap nanoparticles [8]. The next project in this thesis uses the double nanoholes fabricated with this method to trap upconverting nanoparticles and enhance their visible light emission even more than the emission

obtained from rectangular apertures [9]. The large field enhancement of the double nanoholes also show plasmon enhanced 1550 nm emission from erbium doped nanocrystals. Plasmon enhanced 1550 nm emission from a nanocrystal with a single erbium ion can be used as a single-photon source. The colloidal lithography double nanoholes are used in another project to trap single hexagonal boron nitride to obtain second harmonic generation with a low power continuous laser for use in nonlinear optics applications. Finite difference time domain (FDTD) simulations are performed to characterize the field enhancement and Purcell factor in the fabricated nanostructures. Finally, gold nanorods are used to enhance the upconversion emission from two solar bands to be absorbed in silicon and GaAs solar cells [10].

1.2 Organization of the Dissertation

This is a paper-based dissertation, consisting of four papers. Two papers are major contributions of the author and his colleagues to the field, and the other two papers are submitted and published as minor contributions. In the following sections, the major and minor contributions are listed and the authors' contributions to the projects are defined.

1.3 Major Contributions

1.3.1 Harvesting Dual-Wavelength Excitation with Plasmon-Enhanced Emission from Upconverting Nanoparticles [10]

M.S.S. prepared and measured the samples. A.K. and A.A. assisted in the measurements. A.L.F. synthesized and characterized the nanoparticles under the supervision of F.v.V. R.G. supervised the project, providing ideas and facilities and performed the simulations. All authors contributed to writing the manuscript.

1.3.2 Colloidal lithography double nanohole optical trapping of nanoparticles and proteins [8]

A.L.R. and M.S.S. contributed equally to the project. They prepared the samples and measured them. S.M. assisted in writing. R.G. conceived the idea, provided the facilities and supervised the project. All authors contributed to writing the manuscript.

1.4 Minor Contributions

1.4.1 Single Nanoflake hexagonal boron nitride harmonic generation with ultralow pump power [11]

G.H. performed the measurements. G.H. and R.G. identified the effect together. M.S.S. fabricated the nanostructures and worked on finite difference time domain simulations. R.F.A and B.D.G. provided the lithium niobate nanoparticles. R.G. and P.B. came up with the idea, provided the facilities, other nanoparticles and supervised the project. All authors contributed to writing the paper.

1.4.2 Isolating and Enhancing Single Photon Emitters for 1550 nm Quantum Light Sources using Double Nanohole Optical Tweezers [12]

Z.S. and M.D. performed the trapping experiments. Z.S. analyzed the data. A.L.F. and F.C.J.M.v.V. were responsible for nanocrystal synthesis and characterization. M.S.S. performed the finite difference time domain simulations. R.G. conceived the experiment. All authors assisted in writing the manuscript.

Chapter 2

Methods and Review

In this chapter, a brief review is presented on the methods and phenomena involved in the author's experimental and numerical analysis. First, the upconversion and plasmon enhanced upconversion are discussed. Then, a method to obtain plasmonic resonance of spherical and nanorod plasmonic particles are reviewed using the circuit description of plasmonic resonances. The chapter is continued with sections about optical tweezers and nanofabrication methods for different structures. Finally, it ends with principles of finite difference time domain simulations.

2.1 Upconversion

In photonics, upconversion is the process of absorbing multiple low energy photons and combining their energy in order to emit a photon with greater energy [13]. This unique characteristic can be implemented for bioimaging [14], solar absorption [15] spectrum increase and single-molecule microscopy [16] to name a few. It is well-known that near infra-red (NIR) photons are better candidates to penetrate into soft tissue of the body rather than visible light [17, 18, 19]. Upconverting nanoparticles attached to cancer cells for example can help cancer tissue to be imaged by absorbing NIR and emitting visible light which can be easily detected by inexpensive visible sensors [14]. Upconverting particles can also be used to absorb low energy photons which commercial silicon solar cells cannot absorb and convert them to shorter wavelength photons [10]. Multiple harmonic generation or multiple photon absorption as nonlinear optical processes benefit from virtual intermediate states to populate and get an electron excited. Relaxation of this electron produces a photon with higher energy. Unlike the given processes, the upconversion process using lanthanides takes advantage of having multiple long lifetime real intermediate states. Long lifetime energy states provides the opportunity for lanthanides to show 11 times more efficiency than other processes like second harmonic generation [20].

Figure 2.1 shows the electron energy levels in erbium (Er) doped nanoparticles. Since Er does not absorb 980 nm photons efficiently, ytterbium (Yb) is used to ease

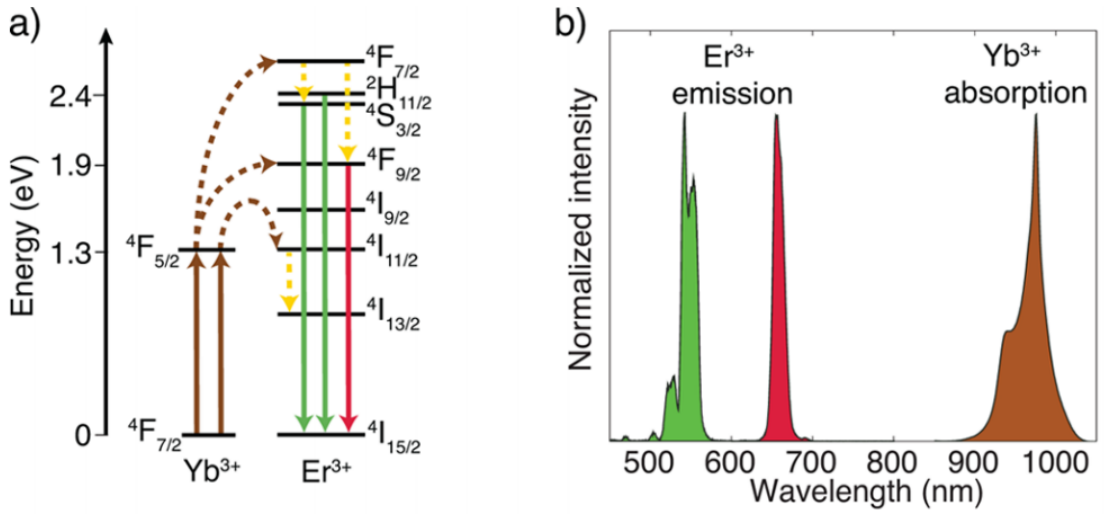

Figure 2.1: (a)upconversion process and energy states in erbium as well as ytterbium (b)normalized absorption and emission bands in erbium [21]. Copyright 2014, American Chemical Society.

upconversion due to its greater absorption. Yb electrons from level $F_{7/2}$, get excited with 980 nm (1.3 eV) photons to level $F_{5/2}$, which F is orbital quantum number and 7/2 as well as 5/2 are total angular momentum quantum numbers. Electrons from level $F_{5/2}$ of Yb transfer to $I_{11/2}$ of Er. This process populates the $I_{11/2}$ intermediate level then these electrons get excited by 980 nm photons to the $F_{7/2}$ level in Er atoms. At the same time, populated electrons at the $F_{5/2}$ of Yb get excited and transfer to the $F_{7/2}$ level of Er. After some nonradiative relaxations, the Er ion emits 650 nm and 545 nm upconverted photons.

Figure 2.2 shows the proposed mechanism of upconversion of 10% Er doped LiYF4 Nanoparticles excited at 1490 nm [22]. In this scheme, 1490 nm wavelength photons excite electrons in the ground state of $I_{15/2}$ to $I_{13/2}$ in Er ions and populates that level

with electrons. Successive absorption of incident photons excite electrons from level $I_{13/2}$ to $I_{9/2}$ and $H_{11/2}$. Similar to excitation of Er doped nanoparticles with presence of Yb ions at 980 nm excitation, these nanoparticles emit 545 nm and 655 nm photons with radiative decay. Since here it can be seen three photon absorption processes in the upconversion mechanism, electrons also excite to $I_{9/2}$ which enables 800 nm radiative decay.

Long-lived metastable levels in lanthanides are associated with 4f orbitals which do not participate in bonding and are isolated by 6s and 6p orbitals. In this situation transition of electric dipoles are parity-forbidden. Thanks to characteristic of host lattice which suppresses nonradiative decay, radiative decay is more probable. All mentioned parameters together create metastable energy levels in the lanthanides [21].

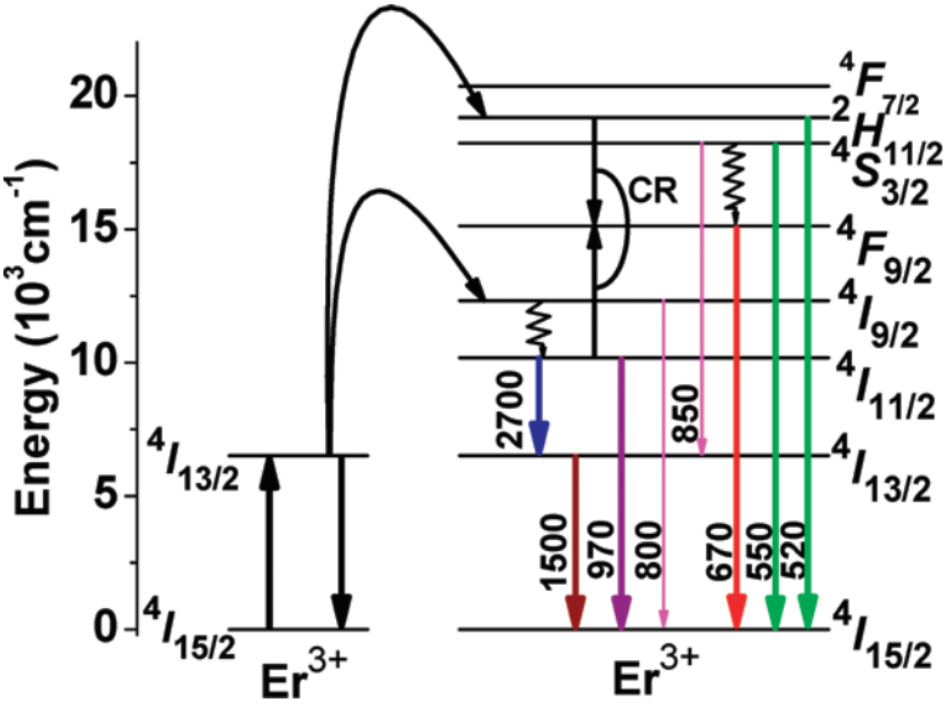

Figure 2.2: Enery states in Er ion and electron transmissions in its upconversion process at 1490 nm [22]. Copyright 2011, American Chemical Society.

2.2 Plasmon enhanced upconversion

Surface plasmon polaritons (SPPs) are electromagnetic waves formed by oscillation of free electrons at the interface of a metal and a dielectric. SPPs propagate along the interface of a metal and a dielectric. They decay quickly perpendicular to the propagation direction [1, 23]. Incident electromagnetic wave can couple to oscillating free electrons at the surface (surface plasmons) which enables confinement of the electric field in a small volume. Considering a gold nanosphere smaller than its skin depth (≈25 nm) at a given optical frequency, the electric field can penetrate in the nanopar-

ticle. This electric field eventuate in displacement of electrons in the particle forming electromachanical oscillator which can resonate at the surface plasmon frequency and form confined field at its surface [24]. Plasmonic nanostructures play the role of nanoantennas helping the rate of receiving and transmitting incident electromagnetic waves. Confined fields can be useful in emission enhancement in upconversion processes [25]. Plasmonic nanoantennas work like regular antennas (radio antennas) but at optical frequencies. Excited plasmon resonances in plasmonic nanoparticles with dimenstions much smaller than incident optical frequencies are able to go beyond the limits of diffraction and refraction of the light in order to control the light and matter interaction at a such small media [26]. Plasmon enhanced emission in upconversion processes is affected through three different mechanisms [27].

- Enhancing upconversion emission by increasing radiative decay rate.
- Enhancing the incident photon absorption through the confined local field near the plasmonic structure
- Decreasing upconversion emission by enhancing nonradiative decay at populated energy states.

2.2.1 Plasmonic absorption increase

Plasmonic nanoantennas can be used for upconversion emission enhancement in two ways [27]. They can increase the local field in order to increase the absorption. The

other mechanism is to increase the decay rate. Maximum field enhancement happens for absorption when plasmonic resonance of the structure matches the absorption wavelength of upconverting nanoparticles. For example, if we want to increase the absorption rate of 980 nm photon in Yb sensitized Er doped nanoparticles, it is recommended to tune the plasmonic resonance to 980 nm. This results in high 980 nm field enhancement near the upconverting nanoparticle which can eventuate in higher upconversion rates due to Fermi's golden rule mentioned below [28]:

$$\gamma_{if} = \frac{2\pi}{\hbar}|\langle f|E.p|i\rangle|^2\rho_f \tag{2.1}$$

where γ_{if} is the transition rate from state $|i\rangle$ to state $\langle f|$, $\hbar$ is the reduced Plank constant, E is the local electric field and p is the transition dipole moment and ρ_f is the electron density in the final states. Since plasmonic nanoantenna confines electric field in very small areas, the magnitude of the electric field increases. This increase, enhances the populating rate of the final energy state, subsequently, the decay rate also increases. In n-photon processes, emission is related to E^{2n}. It can be concluded that processes with a greater number of photons absorbed are more sensitive to incident field confinement. It is also worth mentioning that there is more than one energy state involved in the upconversion process. Plasmonic nanoantennas may affect the populating rate of all of the energy states. This may result in a difference between the calculated and measured emission.

2.2.2 Plasmonic decay rate increase

When the resonance of plasmonic nanoantenna is tuned for upconversion emission wavelength, it alters quantum yield of emitting nanoparticle. In upconverting nanoparticles quantum yield is [21]:

$$\eta = \frac{\gamma_{rad}}{\gamma_{rad} + \gamma_{nonrad}} \tag{2.2}$$

where η is the quantum yield, γ_{rad} is the radiative decay and γ_{nonrad} is nonradiative decay rate. As it was mention before, plasmonic nanoantenna amends both γ_{rad} and γ_{nonrad}. Plasmon-modified radiative decay is the sum of intrinsic radiative decay and the effects of plasmon resonance in the radiative decay rate. Similar statements can be made for plasmon-modified nonradiative decay. If we assume radiative and nonradiative enhancement to be $F_{rad} = \gamma^p_{rad}/\gamma^0_{rad}$ and $F_{nonrad} = \gamma^p_{nonrad}/\gamma^0_{nonrad}$, respectively. The final relation of plasmon-modified quantum yield will be [21]:

$$\eta' = \frac{\eta_0(1 + F_{rad})}{1 + F_{nonrad} + \eta_0(F_{rad} - F_{nonrad})} \tag{2.3}$$

Equation 2.8 shows that emission enhancement happens when $F_{rad} > F_{nonrad}$.

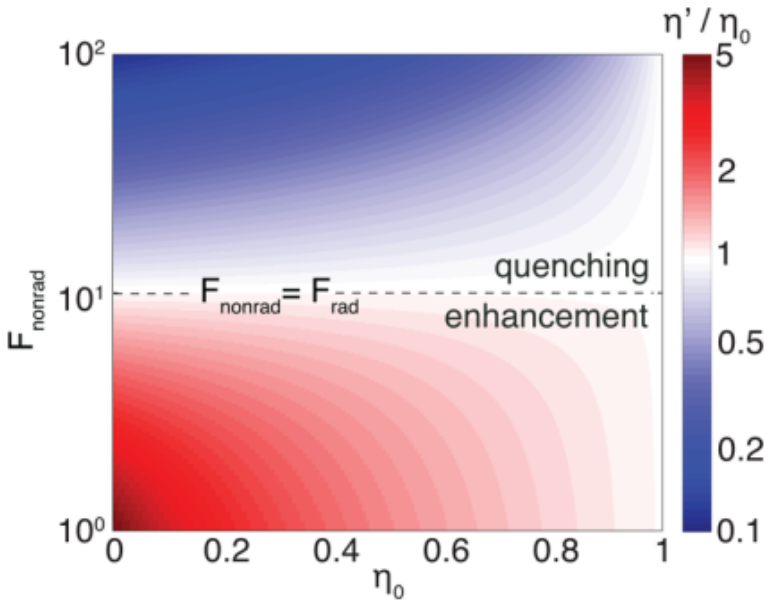

Figure 2.3: The enhancement caused by nonradiative decay map versus intrinsic quantum yield and the ratio of plasmon modified quantum yield and intrinsic quantum yield [21]. Copyright 2014, American Chemical Society.

Figure 2.2 shows a noticeable dependence of quantum yield enhancement on the intrinsic quantum yield. It can be seen that to obtain large quantum yield enhancement in a emitter, the intrinsic quantum yield should be considerably less than 1. The intrinsic quantum yield of lanthanides reach to 0.5 [21].

2.2.3 Circuit description of plasmonic resonance

Dielectric materials have positive permittivity. In electronics, positive permittivity can be described as a capacitor. Similarly, metals with negative permittivity behave like negative capacitors or inductors. Plasmonic nanostructures like gold spheres

in dielectric media like air produce metal-dielectric interfaces which, using a circuit model, can show an inductor-capacitor resonance.

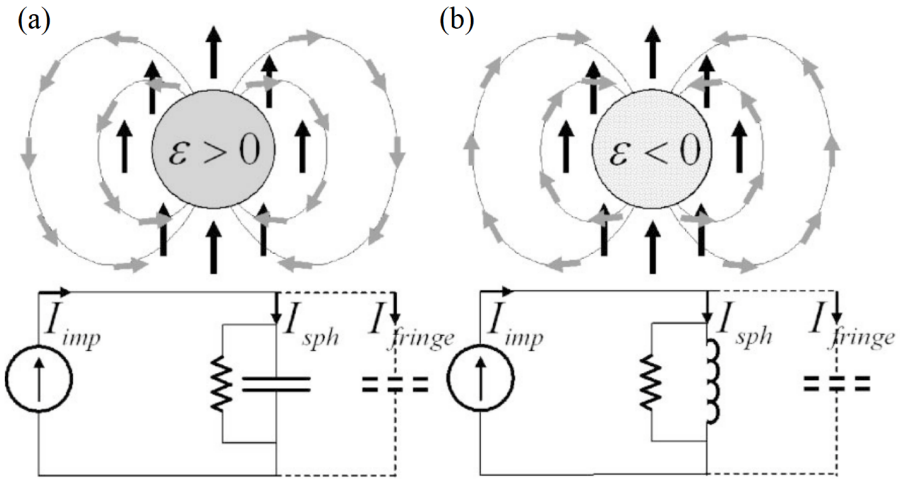

Figure 2.4: Circuit description of (a) nanosphere with positive permittivity (b) plasmonic nanosphere with negative permittivity [29]. Copyright 2005, American Physical Society.

Figure 2.4 (a) and (b) show the dielectric sphere with positive permittivity and the negative permitivity metallic nanoparticle in the dielectric media as well as the modelled electric circuit for each of them, respectively. According to the circuit description for nanospheres, impedance can be calculated for half of the sphere [29, 30]:

$$Z_{sph} = (-i\pi\omega\epsilon_0\epsilon_m r)^{-1} \tag{2.4}$$

$$Z_{fringe} = (-i2\pi\omega\epsilon_0\epsilon_d r)^{-1} \tag{2.5}$$

where ω is angular frequency, ϵ_0, ϵ_d and ϵ_m are permittivity of vacuum, dielectric and metal, respectively.

Similarly, we can model gold nanorods with the circuit description as two half spheres connected with a cylinder as a transmission line. According to microwave antenna theory, the length of an antenna can be used as a parameter to change the operating wavelength of that antenna. Here, change in the length of the gold nanorod tunes its resonance due to meeting the Fabry-Pérot condition for multiple reflections in a simple transmission line.

$$\beta(L - 2r) + \Phi = m\pi \tag{2.6}$$

where β is the propagation constant, L is the nanorod length, r is the radius of sphere, m is the whole-number resonance order and Φ is the phase of the reflection. The propagation constant is calculated using cylindrical waveguide theory:

$$\frac{K_0(p_d r)I_1(p_m r)}{K_1(p_d r)I_0(p_m r)} = -\frac{\epsilon_d p_m}{\epsilon_m p_d} \tag{2.7}$$

$$p_{m,d} = \sqrt{\beta^2 - k_0^2 \epsilon_{m,d}} \tag{2.8}$$

k_n and I_n are modified Bessel functions of second and first order of n [31]. It is worth mentioning that precise estimation of the phase of reflection at both ends of

the double nanohole play important role in obtaining the nanorod's resonances.

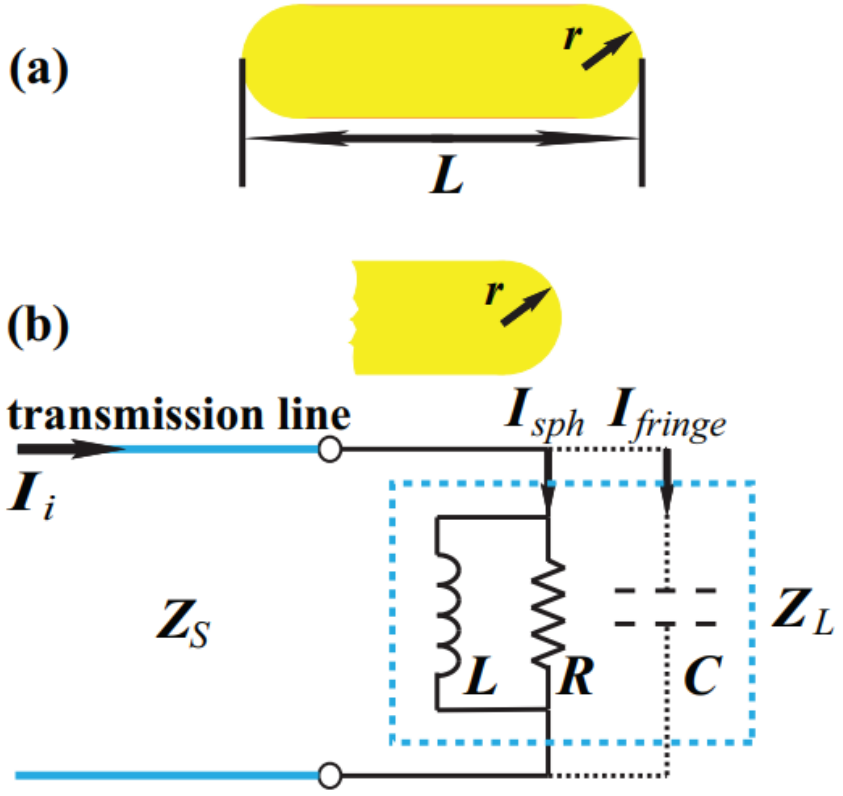

Figure 2.5: Circuit description of resonance of a gold nanorod [31]. Copyright 2015, American Physical Society.

By implementing Equation 2.4 and Equation 2.5 results in the following equation which is obeying transmission line theory in microwave scheme one can obtain phase of reflection. Note that the load impedance Z_L and the transmission line impedance Z_T were calculated for the nanorod using equations [31]:

$$\frac{1}{Z_L} = \frac{1}{Z_{sphere}} + \frac{1}{Z_{fringe}} \tag{2.9}$$

$$Z_T = \sqrt{\frac{\mu_0}{\epsilon_0}} \frac{k_0}{\beta} \tag{2.10}$$

Γ is reflection at the ends of a nanorod was obtained using eq. 2.9 and eq. 2.10

$$\Gamma = \frac{Z_L - Z_T}{Z_L + Z_T} \tag{2.11}$$

$$\Phi = arctan(\frac{Im[\Gamma]}{Re[\Gamma]}) \tag{2.12}$$

2.3 Optical tweezers

In 1986, Arthur Ashkin used a single beam to trap viruses and single nanoparticles [32, 33]. Using light for trapping small particles and manipulating them found many applications for which Ashkin received the Nobel prize in 2018. It is pertubative framework when the effect of particle in surrounding electromagnetic field is minuscule. In the perturbative framework, two main optical forces appear when a particle is exposed to an electromagnetic wave. The force appears as a result of the force exerted on the nanoparticle from the applied photons direction. This force eventuates from the transferred momentum from photons in the same direction. The scattering force on a particle in the Rayleigh regime (particle size is much smaller than incident light wavelength) can be calculated as:

$$F_{scat} = \frac{I_0}{c}\frac{128\pi^5 r^6}{3\lambda^4}(\frac{{n_p}^2 - {n_m}^2}{{n_p}^2 + 2{n_m}^2})^2 n_m \tag{2.13}$$

where I_0 is incident beam intensity, r is the radius of the particle, λ is the incident beam's wavelength, n_p and n_b are the refractive indices of the particle and its background material, respectively. If we consider the role of particle size and beam wavelength on scattering force with the same

$$F_{scat} \propto \frac{r^6}{\lambda^4} \tag{2.14}$$

Gradient force is another optical force applied on a particle in a trap. The gradient force is caused by a gradient of electric field intensity.

$$F_{grad} = \frac{1}{2} n_m \alpha \nabla \mid E \mid^2 = \frac{n_m^3 r^3}{2} \left(\frac{{n_p}^2 - {n_m}^2}{{n_p}^2 + 2{n_m}^2} \right) \nabla \mid E \mid^2 \tag{2.15}$$

where α is the polarizability of the particle and $\mid E \mid^2$ is the intensity of the electric field. It is obvious that the gradient force on a particle obeys the following relation [32]:

$$F_{grad} \propto r^3 \tag{2.16}$$

From Equation 2.14 and Equation 2.16 it can be concluded that in the Rayleigh regime, as the size of the particle shrinks, the gradient force plays a more important role than the scattering force.

Considering the gradient force and scattering force of a nanoparticle trap, it is not applicable to trap a nanoparticle smaller than 100 nm stably. Nanoparticles smaller than 100 nm which are not in Rayleigh regime, gradient force plays the most important role in trapping process. To increase the gradient force, it is needed to use larger beam power to meet appropriate gradient force. The large beam power can cause a damage to the nanoparticle [34]. To overcome this problem, self-induced back-action (SIBA) trapping was suggested by Juan et al. [35]. In this technique, a subwavelength aperture was used to trap the nanoparticle. According to Bethe's

theory [3]:

$$T \propto (\frac{r}{\lambda})^4 \tag{2.17}$$

where T is transmission through the aperture, r is the radius of the aperture, and λ is the incident beam's wavelength in the free space. Since the refractive index of the particle is larger than the the refractive index of the aperture used for the trapping, new λ can be obtained as following:

$$\lambda = \frac{\lambda_0}{n_p} \tag{2.18}$$

where λ_0 is free space wavelength of incident beam, λ is the wavelength of transmitted light through aperture after the particle is trapped and n_p is refractive index of the nanoparticle. Equation 2.17 and Equation 2.18 show when the particle is trapped, the transmission through the aperture increases. SIBA trapping technique benefits from restoring force on the trapped particle which does not allow the particle leave the trap. If the nanoparticle tries to leave the trap the amount of transmistted light through the aperture changes. This changes the total momentum of transmitted photons which exerts a restoring force on the particle which keeps the nanoparticle in the equilibrium situation [36, 35].

2.4 Structure nanofabrication methods

As it is mentioned in the previous section, aperture trapping of nanoparticles using optical tweezers opened a huge door for trapping small nanoparticles. This enabled the characterization and manipulation of those particles in a way that was not possible using traditional optical tweezers. Fabrication of nanostructures for use in nanoparticle trapping gained lots of attention. In this section, some of these techniques are reviewed.

Figure 2.6 shows a small nanohole in an aluminium film with a thickness of 89 nm which was fused on silica coverslips using electron beam lithography. It was also etched using reactive ions after the hole pattern was formed. The obtained structures were less than 100 nm diameter in size [37].

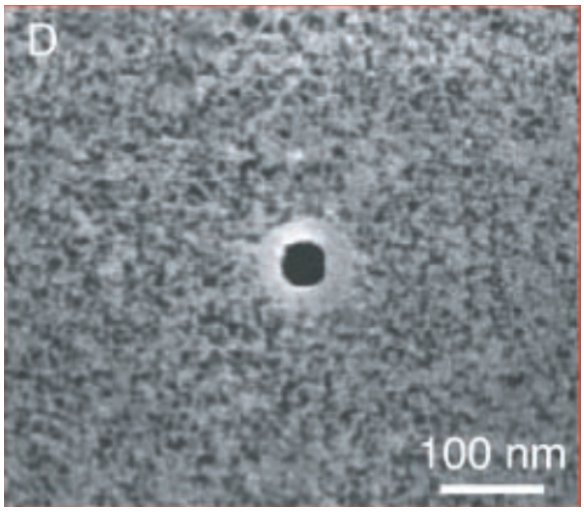

Figure 2.6: A nano hole fabricated using electron beam lithography [37]. Copyright 2013, American Association for the Advancement of Science.

Focused ion beam milling is another powerful method that uses gallium ions to make structures in metals. This technique is favourable due to its flexibility in making different shapes. Figure 2.7 shows a bull's eye [38], double nanohole [4] and bowtie apertures fabricated into thin metal films [39].

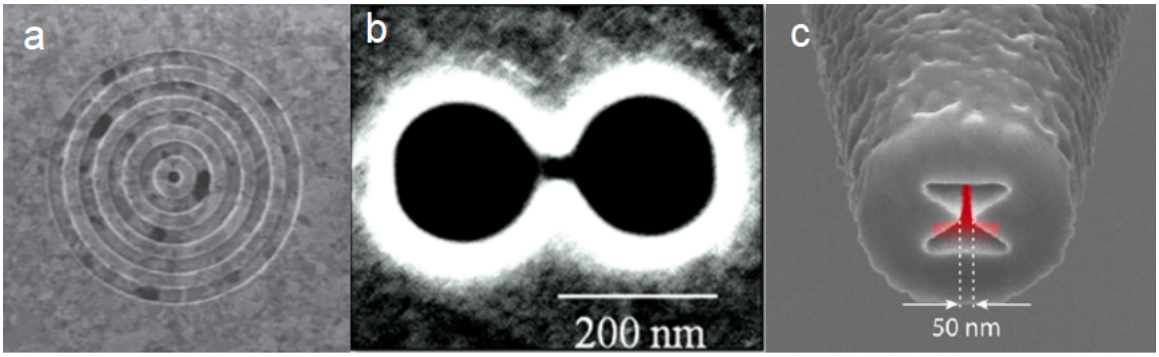

Figure 2.7: Structures fabricated with focused ion beam (a): A bull's eye [38] Copyright 2002, American Association for the Advancement of Science, (b) a double nanohole [4] Copyright 2014, American Chemical Society, (c) a bowtie [39]. Copyright 2012, American Chemical Society.

To fabricate thin gaps, atomic layer deposition (ALD) is used. In this method, large gaps are made, then a thin layer of dielectric such as aluminium oxide is deposited uniformly on top of the gap using the ALD method. This process is followed by the deposition of a metal with a similar thickness to the initial metal film. The tape stripping or milling, then, removes the excess metal in order to obtain narrow gaps [40].

The colloidal lithography method is applied in order to fabricate apertures like nanoholes and double nanoholes. In one of the latest works, colloidal lithography

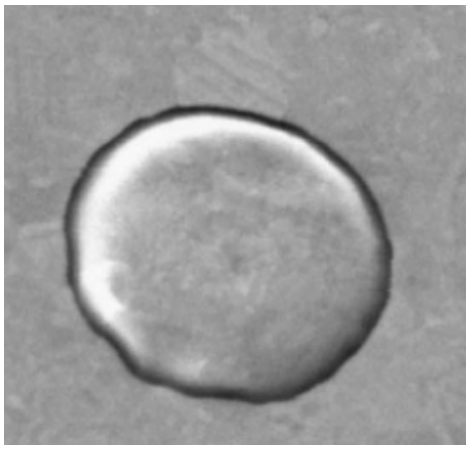

Figure 2.8: A coaxical aperture with narrow gap [40]. Copyright 2013, Nature Publishing Group.

was implemented with plasma etching of the polystyrene beads in order to tune gap size in double nanoholes, which is going to be explained in the following sections as original research in this dissertation.

2.5 Finite difference time domain (FDTD) method

Maxwell's curl equations which are known as Faraday's law and Ampere's law can be solved using the method of finite difference time domain. These equation are listed below:

$$\nabla \times \vec{E} = -\mu \frac{\partial \vec{H}}{\partial t} \tag{2.19}$$

$$\nabla \times \vec{H} = \epsilon \frac{\partial \vec{E}}{\partial t} \tag{2.20}$$

Using the FDTD method, the space in which the equations are solved is discretized into cells. These discretized cells which are rectangular grids are known as Yee cells. Using the Yee cell approach enables us to calculate electric and magnetic fields in time and space. One of the advantages of this method is obtaining impulse responses in single simulations. Figure 2.9 shows a Yee cell. Each facet of a Yee cell has an electric field component normal to the surface with four magnetic field components adjacent to the facet circulating the electric component. Differential equations are solved to obtain electric and magnetic components using a technique known as the leap-frog integration method. Electric and magnetic fields calculated at each time step are used as input data for the next time step in the calculations.

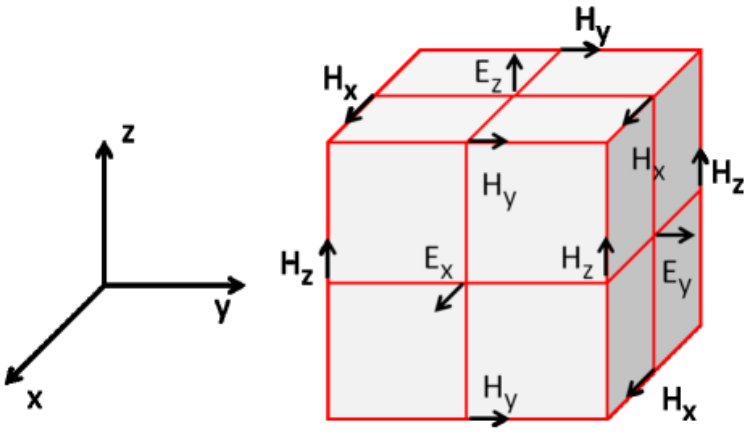

Figure 2.9: A Yee cell with electric field and magnetic field components at each facet[41].

In order to obtain reasonable results, certain measurements need to be applied in FDTD calculations. The size of a Yee cell should be chosen carefully. They should

be smaller than 1/5 of shortest wavelength applied in the calculation. It is worth mentioning that smaller mesh sizes are needed when FDTD calculations are applied on plasmonic nanostructures since they produce smaller wavelengths due to the larger propagation constants. To make sure that the structure is resolvable by the FDTD calculations, the cells' size should be smaller than at least 1/3 of the smallest geometry applied in the simulations. Choosing an appropriate time step in FDTD calucations is the parameter that guarantees the simulation stability. The stability condition is bounded to the cell size according to the following equation in x, y, and z direction as well as the velocity of largest wave propagation, c [41]:

$$\Delta t \leq (c\sqrt{\frac{1}{\Delta x^2} + \frac{1}{\Delta y^2} + \frac{1}{\Delta z^2}})^{-1} \tag{2.21}$$

It is necessary to define a simulation volume for any FDTD calculation. The boundaries of this volume are defined as the boundary conditions. Multiple boundary conditions can be applied to a FDTD simulation depending on the simulation properties:

- **PML** or perfectly matched layer: It is also known as absorbing boundary condition (ABC). PML layers absorbs incident electromagnetic waves where they are applied. It is worth mentioning that some reflection from PML layers could be introduced to FDTD calculation volume with this boundary condition that cause errors in final results. to avoid this larger number of PML layers is needed.

- **PEC** or perfect electric conductor and **PMC** or perfect magnetic conductor: These boundary conditions are designed to reflect electrical and magnetic waves at the boundary where the calculation area is terminated.

- **PBC** or periodic boundary condition: This boundary condition is ideal for periodic structure and electromagnetic waves.

In conclusion, erbium upconversion with and without a sensitizer was reviewed. The mechanisms of plasmon enhanced upconversion were discussed using plasmonic absorption increase and plasmonic decay rate increase. The circuit description of plasmonic resonance was presented in order to understand a method for calculating resonances of sphere and rod schemes. The forces involved in trapping a particle with optical tweezers were explained. The chapter ended with reviewing some useful methods of nanofabrication of structures and finite difference time domain calculations for simulating nanophotonics.

Chapter 3

Contribution

This chapter presents the contributions of the author through four published and submitted papers. In the following section, an overview of each paper is discussed separately. The full manuscripts are attached to the dissertation as Appendices. In the first subsection, the spectroscopy of the gold nanorods with UCNPs is discussed. Then the summary of the colloidal lithography technique for fabricating the double nanoholes and tuning their size follows. In the last subsections, trapping and obtaining the second harmonic generation of hBN nanoflakes and trapping UCNPs in different double nanoholes to enhance the visible and telecommunication emissions are presented.

3.1 Harvesting Dual-Wavelength Excitation with Plasmon-Enhanced Emission from Upconverting Nanoparticles [10].

In this project, we used UCNPs to convert and harvest photons which have considerable energy in the solar spectrum [42, 15]. These photons cannot be harvested by silicon and GaAs solar cells as they are not able to absorb them due to their bandgap. The real intermediate energy states are responsible for the photon upconversion process in erbium doped nanoparticles, like other lanthanides. Intermediate energy levels are filled with electrons by absorbing the energy of incident photons from the ground level of the erbium atoms. While this energy level is populated with the excited electrons, subsequent photons excite those electrons to higher levels. When there are upconverting ions close to each other in the lattice of host, an ion act as donor and the other behaves as an acceptor. The donor ion absorbs incident photon; then, transfers the excited electron energy to the acceptor in the ion pair. This energy transfer is independent of the process of emission and reabsorption. Energy transfer between the pair ions follows the Forster resonance energy transfer (FRET) process which involves dipole-dipole interaction of energy states in both donor and acceptor ions. This happens when the energy gap in the excited donor has resonance with the energy gap of the acceptor in the ground state. The energy transfer be-

tween the donor and acceptor inversely scales with the sixth power of the distance between the ions [43, 44]. This process attracted the attention of researchers due to its higher efficiency compared to other similar processes like multiple harmonic generation. There are a lot of works that applied dual excitation wavelengths on upconverting materials. In one work, dual excitation accompanied with plasmonic enhancement. erbium doped nanoparticles were placed in silver nanowires net and excited with dual wavelengths of 1550 nm and 980 nm. UCNPs doped with erbium mixed with silver nanowires showed 350 times enhanced upconversion emission where UCNPs doped with erbium and ytterbium showed 50 times enhancement [45]. Since most of the research on erbium upconversion has been focused on using a 980 nm excitation wavelength, it appears that it is not beneficial for silicon or GaAs solar cells. However, considering the erbium energy levels, there is a possibility of absorbing two energy bands in the solar spectrum to upconvert the photons energy to be absorbed in silicon or GaAs solar cells. These bands are 1520 nm and 1210 nm.

A supercontinuum laser (Fianium SC400) with a 1200 nm long pass filter was used to to excite the $NaYF_4$ doped with 2 percent erbium nanoparticles in hexane. Upconversion emissions were resolved at 980, 808, 826, 655 and 545 nm wavelengths. Emission intensity from UCNPs at 980 nm and 808 nm wavelengths were measured by altering the excitation band from 1204 to 1230 nm using a prism and a slit, while maintaining the 1520 nm excitation. No upconversion emission was measured in the absence of the 1520 nm excitation band.

The contribution of the 1210 nm band excitation to the upconversion also showed larger upconversion emissions compared to excitation with > 1500 nm alone. Power dependence measurements showed a slope of one for the > 1500 nm excitation which suggests three-step excitation from the ground energy level of the erbium atom. A multi-step process was supported with a slope between 2 and 3 in the power dependence where the excitation band was > 1200 nm. The slope of more than two means three photons are involved in the upconversion process. Depletion of intermediate states are responsible for the decrease of slope in log-log power dependence figure where linear decay from the intermediate states and upconversion processes compete with each other and affect the whole process. This competition eventuates in smaller slopes in the log-log scale which is known as "saturation" [46, 47].

In order to enhance the emission from the UCNPs, they were drop-coated on top of a slide coated with gold. An enhancement of 13 times was observed at 980 nm. Figure 3.1 show the schematic of the setup that was used to measure the emission enhancement from the UCNPs.

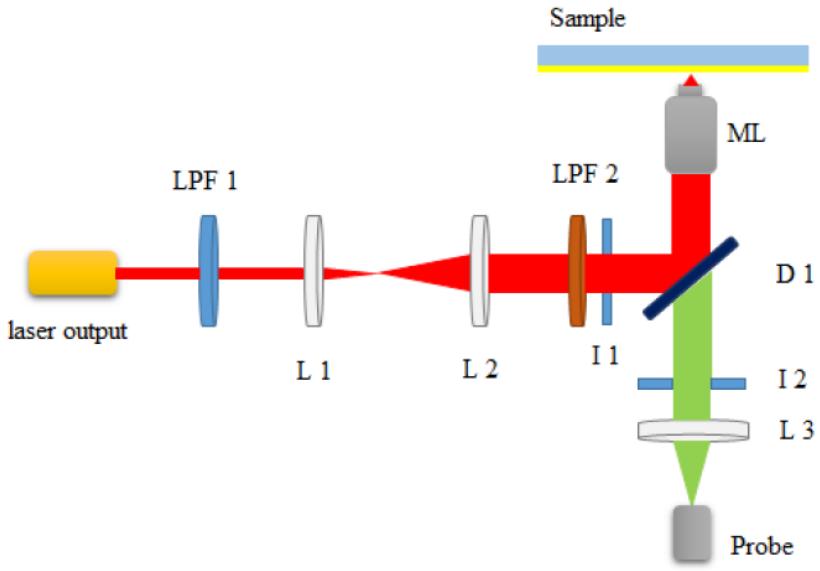

Figure 3.1: Schematics of the setup used for the experiment. LPF1 and LPF2 were 870 and 1200 nm long pass filters. D1 was 1180 nm short pass dichroic mirror [48]. Copyright 2018, Institute of Electrical and Electronics Engineers.

Finally, gold nanorods with resonance at 980 nm and 808 nm were added to the drop-coated layer to enhance the upconverted emission separately. Figure 3.2 shows that the gold nanorods with resonance at 980 nm enhance the emission by 55 percent and that the nanorods with resonance at 808 nm enhanced the emission by 32 percent, with a ratio of UCNPs to gold nanorods of 15000:1 [10].

The upconverter nanoparticles are able to upconvert the wavelengths that are not absorbed in the silicon and GaAs solar cells. Therefore, the upconverters accompanied with nanorods can be placed at the back of the solar cells. The nanorods are able to enhance the upconversion emission obtained from upconverting nanoparticles. The

bands of interest in solar spectrum (1520 nm and 1210 nm) are absorbed into UCNPs, then the upconverted emissions get enhanced by gold nanorods which are placed at the back of the solar cell. The enhanced emission gets absorbed into the solar cell.

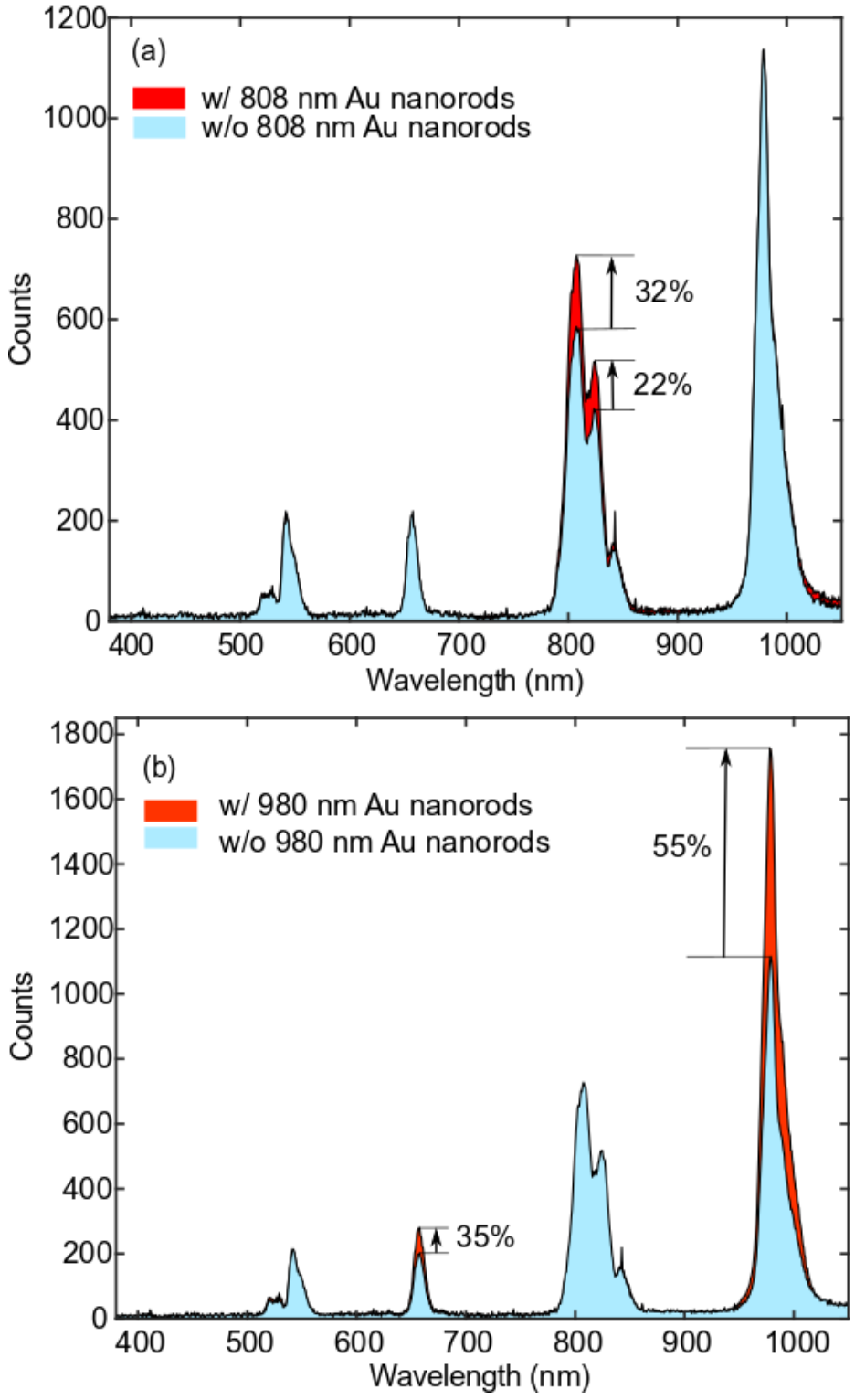

Figure 3.2: (a) Enhanced upconversion at 808 nm when using 808 nm nanorods. (b) Enhanced upconversion at 980 nm when using 980 nm nanorods [10]. Copyright 2018, American Chemical Society.

3.2 Colloidal lithography double nanohole optical trapping of nanoparticles and proteins [8]

Optical trapping of single nanoparticles made it possible to characterize and investigate their interaction. To trap the particles below 100 nm in size, it is necessary to overcome the Rayleigh limit by focusing the electric field and increasing the gradient force. The double nanohole structure is one of the successful candidates among other nanostructures like circular and rectangular apertures. Double nanoholes are used in optical trapping setups to trap, characterize and study the interactions between DNA and proteins. Probing the vibrational modes of the single nanoparticles is one the prominent works that stands out among other similar techniques [2, 4, 49, 50].

We were motivated to come up with a novel, easy, reproducible, and inexpensive method to fabricate double nanoholes in thin gold films as the focused ion beam (FIB) machine in our nanofabrication facility was down. Top-down techniques like FIB are expensive and one can fabricate only limited amounts in a relatively long process (4-5 hours).

Here, we used a colloidal lithography technique to fabricate the double nanoholes in a thin metal film for trapping single nanoparticles and proteins. In this technique, 200 nm polystyrene beads were diluted in ethanol solution at 0.01% w/v. A volume of 30μL of the obtained solution was drop-coated on a glass slide which was sonicated

in an ethanol bath and plasma cleaned beforehand. Then, the particles were left for drying overnight. The samples were placed in the plasma etching machine with multiple time steps to decrease the size of the polystyrene beads. This process was followed by first coating with 5 nm of Ti as an adhesive layer and then with 70 nm of gold using PVD sputtering machine. To remove the polystyrene beads after the deposition, the samples were sonicated in ethanol for 5 minutes.

The fabricated apertures were randomly distributed. They needed to be able to be located when being used in the trapping setup. Multiple unique patterns of apertures were found using the SEM and were verified in the trapping setup to find the aperture of interest [8, 51]. Once the double nanohole structures were fabricated in gold film, SEM figures of the surface of the sample were taken. The magnification of the SEM figures were comparable to the optical trapping setup's imaging magnification. A fiduciary mark on the sample was applied by making a scratch which helped us find the structures under the Trapping setup. It is known that assemblies larger than dimers fabricated with colloidal lithography method have larger cut-off transmitting larger amount of light through them helped us in locating structures under the trapping setup. Using the fiduciary mark and larger assemblies in both the SEM figure and the image of sample enabled us to assign unique patterns that can be found under the trapping setup. In this fabrication method, the fabricated structures were far enough from each other (around 1-2 microns) which allowed one to easily locate the apertures under the trapping setup. Once one had the SEM figure and the unique

pattern of fabricated structures, it was easy and quite fast to find the structure of interest if one used a fiduciary mark and larger apertures on the sample. This process took less than 10 minutes for the samples used in this thesis.

Figure 3.3 (a) shows the effect of plasma etching time on the aperture size and the cusp separation. Figure 3.3 (b) shows the APD voltage resulting from transmitted 980 nm light using the apertures made by this technique.

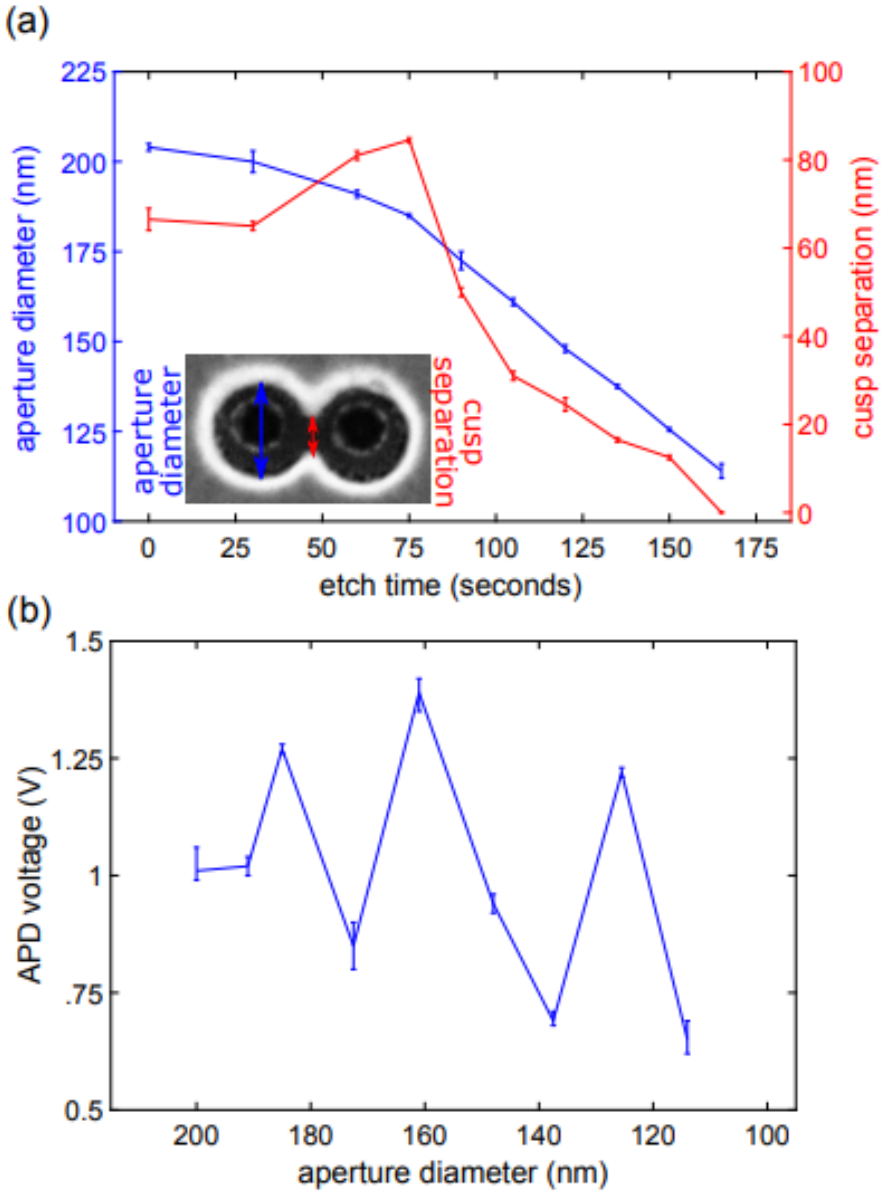

Figure 3.3: (a) Effect of plasma etching on the dimensions of the double nanohole aperture diameter and cusp separation indicated in inset (b) Transmission (APD voltage) through double nanohole apertures with dimensions varying according to respective etch times [8]. Copyright 2019, Optical Society of America.

Figure 3.4(a) shows the trapping of 30 nm polystyrene nanoparticles. Figures 3.4(b)

and (c) show the trapping of single rubisco and bovine serum albumine (BSA) in the double nanoholes fabricated by the colloidal lithography method. The concentration of the solutions used for trapping of 30 nm polystyrene, Rubisco, and BSA were 1% w/v, 0.6% w/v, and 2% w/v, respectively. It is worth to mention that polystyrene particles were dissolved in deionized water. The BSA and Rubisco were diluted in PBS buffer solution. The repeatability in trapping process was ensured by observation of 20 trapping events of same nanoparticle or protein.

3.3 Single Nanoflake hexagonal boron nitride harmonic generation with ultralow pump power

In this project, nonlinear response from a single hexagonal boron nitride nanoflake was resolved while trapped in double nanohole plasmonic tweezer.

The studies toward the second harmonic generation from two dimensional materials suggest that using ultra fast-lasers are essential to obtain nonlinear responses [52, 53, 54]. These ultra-fast lasers deliver a specific amount of laser power in short time (on the order of 100 fs). This provides approximately 1000 W of peak power in the pulse window while the average laser power is 10 mW.

Using plasmonic sturctures enabled us to focus the electric field in a small area. This provided an opportunity to investigate the second harmonic generation from hBN nanoflakes which they were smaller than the diffraction limit. Here, we used an

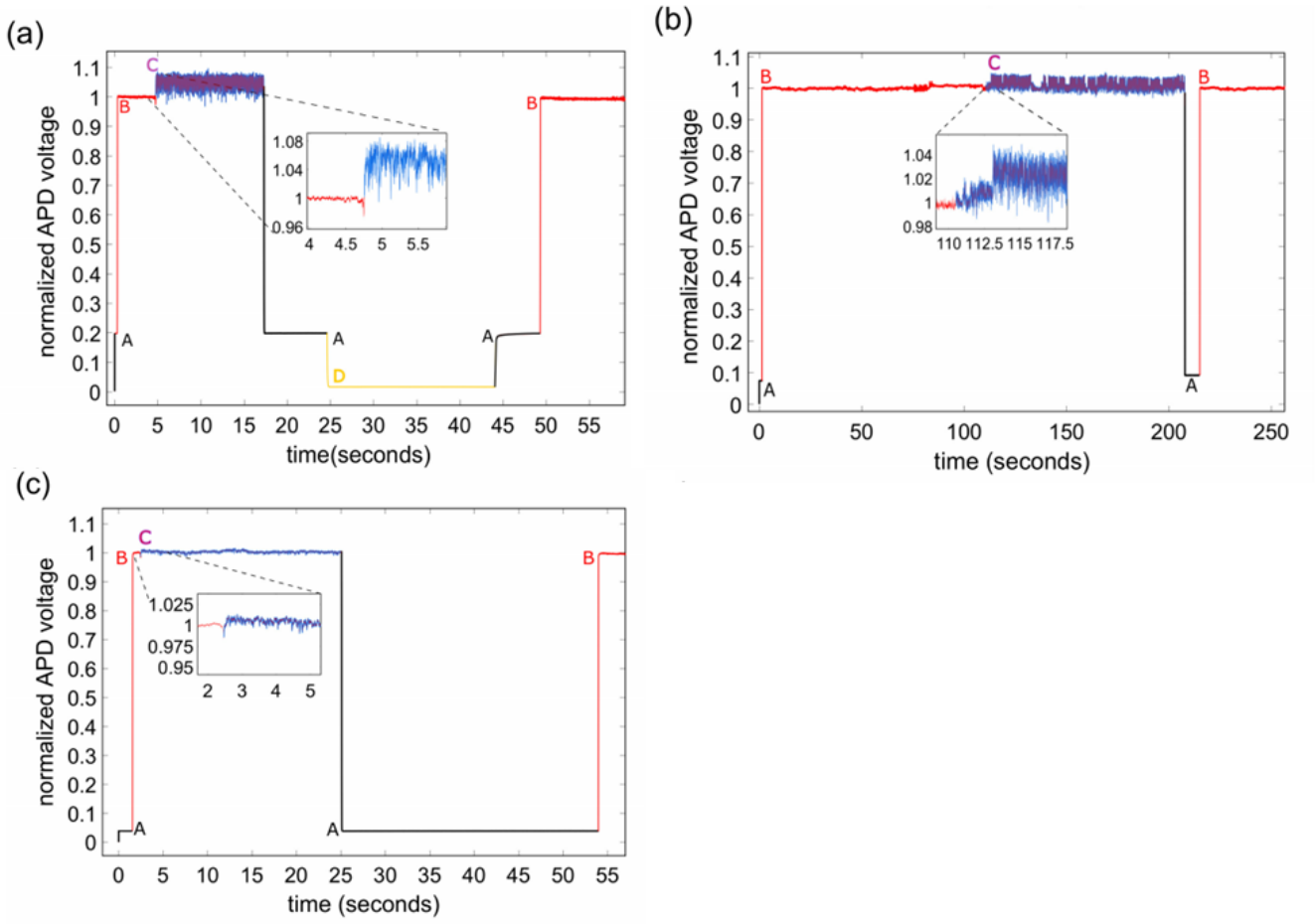

Figure 3.4: Trapping of (a) 30 nm polystyrene nanosphere (b) rubisco and (c) BSA. The cusp spearation was 60 nm for (a) and (b) and 10 nm for (c) [8]. Copyright 2019, Optical Society of America.

optical tweezer with a gold double nanohole structure to trap a single hBN particle. These double nanoholes were fabricated using the colloidal lithography technique.

Figure 3.5(a) shows the SEM image of the double nanohole used for trapping the nanoflakes. The aperture diameter was around 300 nm and the cusp separation was around 90 nm. In this figure, the schematic of the optical setup was presented. The setup was modified by adding an Ocean Optics QE65000 spectrometer, shortpass and bandpass filters to be able to measure the incident wavelength and second harmonic signal. Figure 3.5(b) shows the transmitted power from the double nanohole for the hBN particle's trapped and untrapped states. The transmission through the double nanohole increases when the particle was trapped due to refractive index change in the aperture. Figure 3.5(c) shows the spectrum of the incident wavelength, 973 nm, and the second harmonic signal at 486.5 nm. No second harmonic signal was detected when there was no hBN particles in the trapping solution or when a polystyrene particle with point symmetry was trapped in the double nanohole.

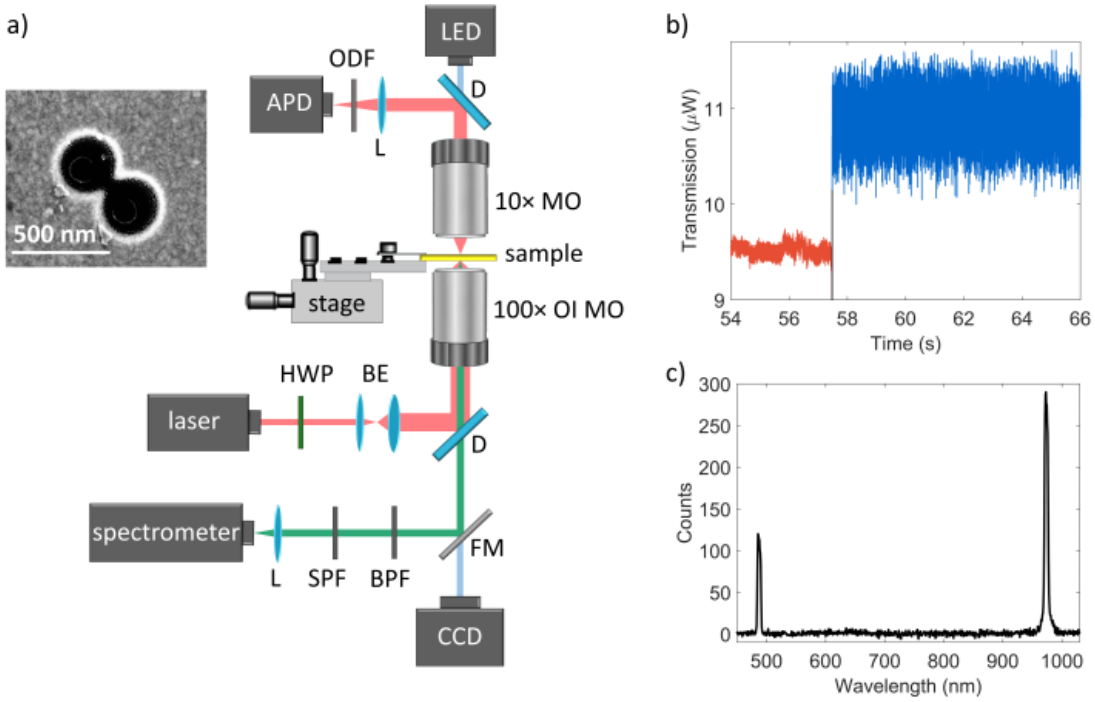

Figure 3.5: Experimental setup. (a) Schematic of the DNH laser tweezer setup: charge-coupled device (CCD) camera, flip mirror (FM), shortpass filter (SPF), band-pass filter (BPF), lens (L), half-wave plate (HWP), beam expander (BE), shortpass dichroic mirror (D), 100 × oil immersion microscope objective (OI MO), piezo stage (stage), 10 ×microscope objective (MO), optical density filter (ODF), and avalanche photodetector (APD). Inset: scanning electron microscope (SEM) image of a typical DNH with aperture diameter of 300 ± 10 nm and gap size of 90 ± 10 nm. (b) Typical one-step trapping event of hBN nanoflakes: untrapped state (red), transition from untrapped to trapped (black), and trapped state (blue). Data is plotted in three colors to indicate the trapping state. (c) The spectrum of the fundamental beam at 973 nm and the SHG signal at 486.5 nm measured in a trapping event with a 3 s acquisition time. With filters, the fundamental peak was attenuated by 2×10^8 and the SHG peak was attenuated by 4. Background counts were subtracted.

Power dependence measurements were also carried out for hBN, WS_2, MoS_2 and

lithium niobate nanoparticles. The power was altered in two different paths for hBN. In the first path, it started from 7.5 mW and increased to 13.25 mW. In the second one, it decreased from 13.25 mW to 3.5 mW. The results showed a slope of 2.1 on a log-log scale which supported the second harmonic generation here. Slopes of 2.14 and 2.1 were observed for WS_2 and MoS_2 when lower powers were applied. Similar results were found for lithium niobate particles power dependence.

Finite difference time domain (FDTD) simulations were implemented to calculate the electric field intensity profile in the double nanohole. Figure 3.6 shows a 500 times enhancement in electric field intensity at the tips of the cusps of the double nanohole. In this simulation, a total field scattering field (TFSF) source with a wavelength range from 400 to 1100 nm was used and a 2 nm uniform mesh was also chosen. Purcell factor was also calculated through FDTD simulations. The maximum Purcell factor occurs at 450 nm for the double nanohole used in this experiment. The Purcell factor was calculated by dividing the local density of states of a dipole source when the plasmonic structure was present by the dipole source without the structure.

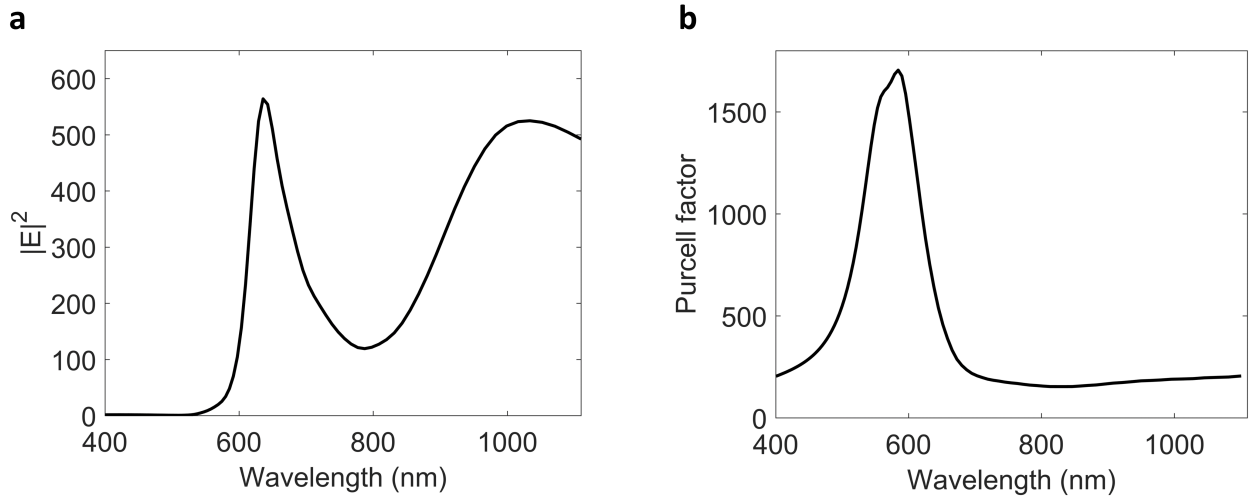

Figure 3.6: Local field intensity spectrum and Purcell factor. a, The electric field enhancement spectrum in the gap region of a DNH with 90 nm gap size and 300 nm diameter in 70 nm gold film. b, Purcell factor enhancement obtained by finite difference time domain simulations in the gap region.

3.4 Isolating and Enhancing Single Photon Emitters for 1550 nm Quantum Light Sources using Double Nanohole Optical Tweezers

In this project, double nanoholes with different aperture sizes and cusp separations fabricated with colloidal lithography method [8]were used to trap and isolate upconversion nanocrystals. Using double nanohole apertures made it possible to increase the trapping force due to incident field enhancement and increased the upconversion

emission since plasmonic structures are able to alter the radiative and non-radiative decay rate in quantum emitters.

Previously, our group enhanced the emission from the upconversion nanocrystals using the optical trapping setup with rectangular apertures, achieving 400 times enhancement [9]. Here, we trapped $NaYF_4$ nanoparticles doped with 18 percent ytterbium and 2 percent erbium in the double nanohole plasmonic structures. Since the double nanohole structures can provide larger field enhancement in comparison with the rectangular apertures, it was expected to observe larger enhancement of upconversion emission from the UCNPs. We observed around 50 times larger enhancement in upconversion emission than the emissions obtained from UCNPs trapped in rectangular apertures.

Since the apertures were fabricated using the colloidal lithography technique, aperture and cusp separation sizes could be tuned with plasma etching time when the polystyrene particles were drop-coated on glass slides, before coating with 70 nm of gold by PVD sputtering [8]. The size change in the aperture and cusp separation allowed for tuning the multiple resonances of the double nanohole apertures to obtain maximum enhancement from the UCNPs. Cusp separation in the double nanoholes was chosen as the principle parameter of the fabricated structures, since the largest field enhancement occurs at the tips of the cusps. The cusp separations were varied between 23 to 95 nm. In this experiment, peaks at approximately 400 nm and 1550 nm were detected due to larger enhancement of the upconversion emission with

the double nanohole structure. Peaks at 550 nm and 650 nm were also observed, which were previously seen with the rectangular apertures.

Figure 3.7 shows the effect of changing the cusp separation on the upconversion emission intensities of 400, 550 and 650 nm wavelengths. The UCNPs' sizes were chosen to be 26.2 nm and 16.9 nm to trap them in apertures with cusp separations from 32 to 95 nm and smaller than 32 nm. The full lines and dashed lines are showing the upconversion emission counts from 26.2 nm and 16.9 nm, respectively. This arrangement was chosen due to appropriate trapping capability of those nanoparticles in the apertures. The largest enhancement was observed for the aperture with 32 nm cusp separation for both nanoparticle sizes.

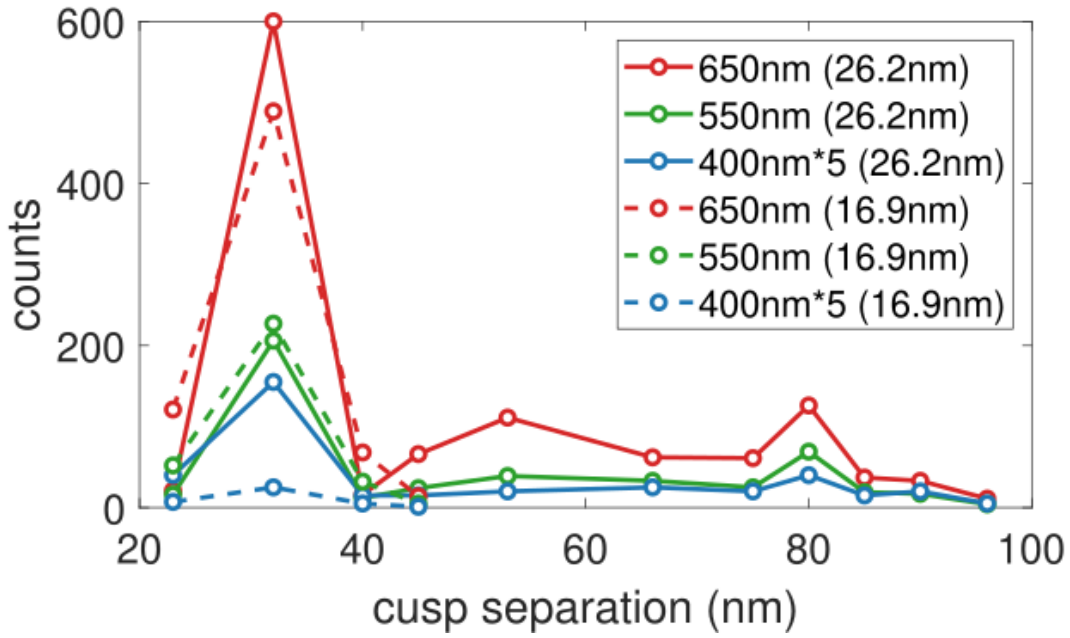

Figure 3.7: Investigating the influence of the DNH cusp separation on emission enhancement. Emission from 17 nm and 26 nm nanocrystals at 400 nm, 550 nm, 650 nm for varying DNH cusp separations. Emission counts at 400 nm are multiplied by 5 for visibility [12]. Copyright 2021, AIP Publishing LLC.

FDTD simulations were carried out to investigate the aperture resonances and field enhancements in the double nanoholes of interest. Figure 3.8 (b) shows the spectra of the field enhancement in the apertures with cusp separations from 23 to 45 nm. The largest field enhancement was observed in the aperture with 32 nm enhancement at the 980 nm wavelength, which agreed well with experimental results.

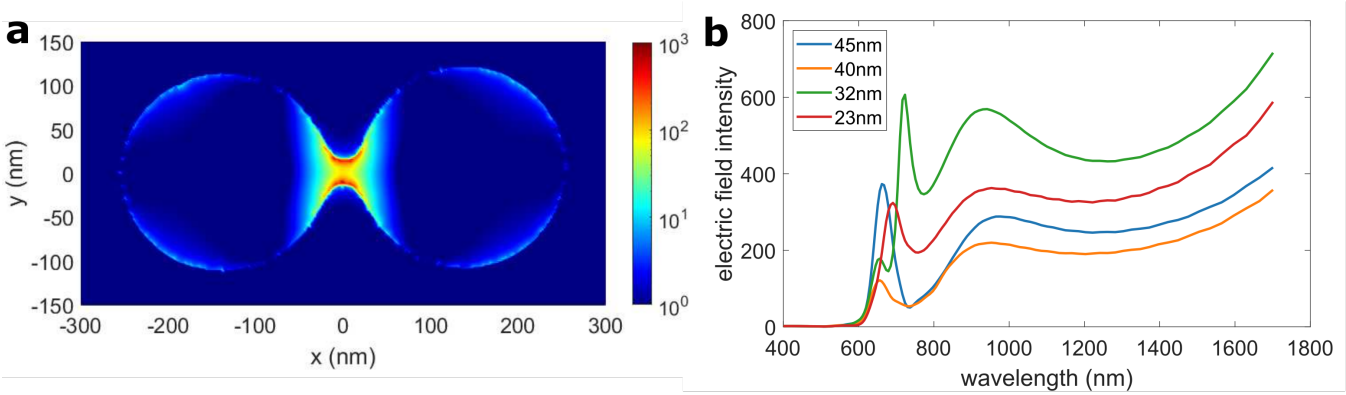

Figure 3.8: Simulated electric field intensity. (a) Visualization of the electric field intensity inside of a DNH with 32 nm cusp separation. (b) Electric field intensity for DNHs with 22.7 nm, 32 nm, 40 nm, and 45 nm cusp separations. Normalized to the incident intensity [12]. Copyright 2021, AIP Publishing LLC.

Finding the aperture with largest enhancement provided the opportunity to investigate the emission from single erbium ion emitters. Discrete levels of emission at 650 nm were resolved which correlated with the number of emitters in the upconversion nanoparticle. The trapping rates of the UCNPs were also measured. This showed faster trapping for both upconverter sizes for the aperture with largest field enhancement at 980 nm wavelength [12].

Chapter 4

Conclusions and future works

4.1 Conclusions

In this dissertation, plasmonic structures such as gold nanorods and double nanoholes were used to enhance emission from upconverting nanoparticles and produce second harmonic generation from 2D meterials and nanoparticles. The fabricated double nanoholes were also used in optical trapping projects.

In the first project, gold nanorods with resonances at 980 nm and 808 nm selectively enhanced upconverted emission from two excitation bands at 1210 nm and 1520 nm which exist in the solar spectrum. Commercial silicon solar cells and GaAs solar cells are not able to absorb these bands due to their band gap limitations. Erbium doped nanoparticles were drop coated on top of a gold layer and showed thirteen-fold enhancement at 980 nm. Adding the gold nanorods with resonances at

980 nm eventuated in 55% enhancement in the 980 nm emission. The same process was carried out for the gold nanorods with resonance at 808 nm which showed 32% enhancement for 808 nm emission.

In the second project, a colloidal lithography technique was used to fabricate double nanohole structures which were implemented in nanoparticle trapping. These double nanoholes were fabricated in gold films by drop coating a solution of polystyrene beads. Their sizes were tuned by plasma etching before coating with gold. The 30 nm polystyrene beads, rubisco protein and BSA protein were successfully trapped using these double nanoholes.

In the third project, hBN nanoflakes and other 2D nanoparticles were trapped using the colloidal lithography double nanoholes. A second harmonic signal was resolved from a single nanoflake while it was trapped and excited with a low power continuous laser. The FDTD simulation calculated around a 500-fold enhancement in the electric field intensity near the double nanohole cusps. FDTD simulations also showed the Purcell factor was enhanced 450-fold at the second harmonic wavelength.

In the last project, erbium doped UCNC were trapped and excited at 980 nm. Maximum upconversion enhancement was reached from UCNCs detected in the double nanohole with a 32 nm cusp separation. This was achieved by obtaining the maximum field enhancement at the fundamental wavelength where the cusp separation in colloidal lithography double nanoholes were varied from 90 to 20 nm. FDTD simulation results agreed well with the experiments. The maximum enhanced emission

from the UCNCs in double nanoholes were 50 time greater than plasmon enhanced emission from rectangular apertures. 1550 nm emission was resolved while trapping due to large field enhancement in double nanoholes in comparison to the experiment done with rectangular apertures.

4.2 Future works

4.2.1 Probing bright and dark mode resonances in a gold nanorod

While performing the experiments for "Harvesting dual-wavelength excitation with plasmon-enhanced emission from upconverting nanoparticles", a 35 percent enhancement of upconversion emission at 658 nm was observed, which was not related to the resonances of the short and long axes of the used nanorods. We believe this enhancement comes from the dark mode of the nanorod [10].

A model that can predict the nanorod resonances using a circuit description and the quasistatic approximation, at the two tips of nanorod, can pave the road to obtaining the electric and magnetic fields around the nanorod without large numerical calculations. A numerical model to achieve this for the dark mode resonances of a nanorod is presented in Appendix E, yet developing a model to estimate the bright mode resonance of a nanorod is needed to be investigated.

4.2.2 Finding best colloidal lithography double nanohole for 1550 nm emission enhancement

Colloidal lithography is a method to fabricate large amounts of nanoapertures with inexpensive facilities [55]. Using the plasma etching technique provides a means of altering the size of polystyrene nanoparticles before the coating process. This makes colloidal lithography a powerful fabrication method with the ability to tune aperture size and cusp separation in fabricated double nanoholes [8]. The double nanoholes fabricated with this technique can be used as plasmonic nanoantennas to enhance 1550 nm emission from erbium emitters as possible single-photon sources. It is essential to explore different sizes of double nanoholes in order to tune the resonances of these apertures and to enhance the upconversion emission at the 1550 nm telecom band.

Bibliography

[1] Stefan Alexander Maier. *Plasmonics: fundamentals and applications*. Springer Science & Business Media, 2007.

[2] Yuanjie Pang and Reuven Gordon. Optical trapping of 12 nm dielectric spheres using double-nanoholes in a gold film. *Nano Letters*, 11(9):3763–3767, 2011.

[3] Yuanjie Pang and Reuven Gordon. Nanophotonics using a subwavelength aperture in a metal film. *Nanotechnology Reviews*, 1(4):339–362, 2012.

[4] Abhay Kotnala and Reuven Gordon. Quantification of high-efficiency trapping of nanoparticles in a double nanohole optical tweezer. *Nano Letters*, 14(2):853–856, 2014.

[5] Abhay Kotnala and Reuven Gordon. Double nanohole optical tweezers visualize protein p53 suppressing unzipping of single dna-hairpins. *Biomedical Optics Express*, 5(6):1886–1894, 2014.

[6] Skyler Wheaton, Ryan M Gelfand, and Reuven Gordon. Probing the raman-active acoustic vibrations of nanoparticles with extraordinary spectral resolution. *Nature Photonics*, 9(1):68, 2015.

[7] Paul J Campagnola, Andrew C Millard, Mark Terasaki, Pamela E Hoppe, Christian J Malone, and William A Mohler. Three-dimensional high-resolution second-harmonic generation imaging of endogenous structural proteins in biological tissues. *Biophysical Journal*, 82(1):493–508, 2002.

[8] Adarsh Lalitha Ravindranath, Mirali Seyed Shariatdoust, Samuel Mathew, and Reuven Gordon. Colloidal lithography double-nanohole optical trapping of nanoparticles and proteins. *Optics Express*, 27(11):16184–16194, 2019.

[9] Amirhossein Alizadehkhaledi, Adriaan L Frencken, Mohsen Kamandar Dezfouli, Stephen Hughes, Frank CJM van Veggel, and Reuven Gordon. Cascaded plasmon-enhanced emission from a single upconverting nanocrystal. *ACS Photonics*, 6(5):1125–1131, 2019.

[10] Mirali Seyed Shariatdoust, Adriaan L Frencken, Ali Khademi, Amirhossein Alizadehkhaledi, Frank CJM van Veggel, and Reuven Gordon. Harvesting dual-wavelength excitation with plasmon-enhanced emission from upconverting nanoparticles. *ACS Photonics*, 5(9):3507–3512, 2018.

[11] Ghazal Hajisalem, Mirali Seyed Shariatdoust, Rana Faryad Ali, Byron D Gates, Paul E Barclay, and Reuven Gordon. Single nanoflake hexagonal boron nitride harmonic generation with ultralow pump power. *ACS Photonics*, 2021.

[12] Zohreh Sharifi, Michael Dobinson, Ghazal Hajisalem, Mirali Seyed Shariatdoust, Adriaan L Frencken, Frank CJM van Veggel, and Reuven Gordon. Isolating and enhancing single-photon emitters for 1550 nm quantum light sources using double nanohole optical tweezers. *The Journal of Chemical Physics*, 154(18):184204, 2021.

[13] Richard Scheps. Upconversion laser processes. *Progress in Quantum Electronics*, 20(4):271–358, 1996.

[14] Guanying Chen, Hailong Qiu, Paras N Prasad, and Xiaoyuan Chen. Upconversion nanoparticles: design, nanochemistry, and applications in theranostics. *Chemical Reviews*, 114(10):5161–5214, 2014.

[15] Xiaoyong Huang, Sanyang Han, Wei Huang, and Xiaogang Liu. Enhancing solar cell efficiency: the search for luminescent materials as spectral converters. *Chemical Society Reviews*, 42(1):173–201, 2013.

[16] Daniel J. Gargas, Emory M. Chan, Alexis D. Ostrowski, Shaul Aloni, M. Virginia P. Altoe, Edward S. Barnard, Babak Sanii, Jeffrey J. Urban, Delia J. Milliron, Bruce E. Cohen, and P. James Schuck. Engineering bright sub-10-nm

upconverting nanocrystals for single-molecule imaging. *Nature Nanotechnology*, 9(4):300, 2014.

[17] MV Padalkar and N Pleshko. Wavelength-dependent penetration depth of near infrared radiation into cartilage. *Analyst*, 140(7):2093–2100, 2015.

[18] Si Wu and Hans-Jürgen Butt. Near-infrared-sensitive materials based on upconverting nanoparticles. *Advanced Materials*, 28(6):1208–1226, 2016.

[19] Petras Juzenas, Asta Juzeniene, Olav Kaalhus, Vladimir Iani, and Johan Moan. Noninvasive fluorescence excitation spectroscopy during application of 5-aminolevulinic acid in vivo. *Photochemical & Photobiological Sciences*, 1(10):745–748, 2002.

[20] François Auzel. Upconversion and anti-stokes processes with f and d ions in solids. *Chemical Reviews*, 104(1):139–174, 2004.

[21] Di M Wu, Aitzol García-Etxarri, Alberto Salleo, and Jennifer A Dionne. Plasmon-enhanced upconversion. *The Journal of Physical Chemistry Letters*, 5(22):4020–4031, 2014.

[22] Guanying Chen, Tymish Y Ohulchanskyy, Aliaksandr Kachynski, Hans Ågren, and Paras N Prasad. Intense visible and near-infrared upconversion photoluminescence in colloidal $LiYF_4$: Er3+ nanocrystals under excitation at 1490 nm. *ACS Nano*, 5(6):4981–4986, 2011.

[23] Stefan A Maier, Mark L Brongersma, Pieter G Kik, Sheffer Meltzer, Ari AG Requicha, and Harry A Atwater. Plasmonics—a route to nanoscale optical devices. *Advanced Materials*, 13(19):1501–1505, 2001.

[24] Mark I Stockman. Nanoplasmonics: past, present, and glimpse into future. *Optics Express*, 19(22):22029–22106, 2011.

[25] Lukas Novotny and Niek Van Hulst. Antennas for light. *Nature Photonics*, 5(2):83–90, 2011.

[26] Vincenzo Giannini, Antonio I Fernández-Domínguez, Susannah C Heck, and Stefan A Maier. Plasmonic nanoantennas: fundamentals and their use in controlling the radiative properties of nanoemitters. *Chemical Reviews*, 111(6):3888–3912, 2011.

[27] Matthew Pelton, Javier Aizpurua, and Garnett Bryant. Metal-nanoparticle plasmonics. *Laser & Photonics Reviews*, 2(3):136–159, 2008.

[28] Lukas Novotny and Bert Hecht. *Principles of nano-optics*. Cambridge university press, 2012.

[29] Nader Engheta, Alessandro Salandrino, and Andrea Alu. Circuit elements at optical frequencies: nanoinductors, nanocapacitors, and nanoresistors. *Physical Review Letters*, 95(9):095504, 2005.

[30] Nader Engheta. Circuits with light at nanoscales: optical nanocircuits inspired by metamaterials. *Science*, 317(5845):1698–1702, 2007.

[31] Wei Su, Xiangyin Li, Jens Bornemann, and Reuven Gordon. Theory of nanorod antenna resonances including end-reflection phase. *Physical Review B*, 91(16):165401, 2015.

[32] Arthur Ashkin, James M Dziedzic, JE Bjorkholm, and Steven Chu. Observation of a single-beam gradient force optical trap for dielectric particles. *Optics Letters*, 11(5):288–290, 1986.

[33] Arthur Ashkin and James M Dziedzic. Optical trapping and manipulation of viruses and bacteria. *Science*, 235(4795):1517–1520, 1987.

[34] Faegheh Hajizadeh and S Nader S Reihani. Optimized optical trapping of gold nanoparticles. *Optics Express*, 18(2):551–559, 2010.

[35] Mathieu L Juan, Reuven Gordon, Yuanjie Pang, Fatima Eftekhari, and Romain Quidant. Self-induced back-action optical trapping of dielectric nanoparticles. *Nature Physics*, 5(12):915, 2009.

[36] Ahmed A Al Balushi, Abhay Kotnala, Skyler Wheaton, Ryan M Gelfand, Yashaswini Rajashekara, and Reuven Gordon. Label-free free-solution nanoaperture optical tweezers for single molecule protein studies. *Analyst*, 140(14):4760–4778, 2015.

[37] Michael J Levene, Jonas Korlach, Stephen W Turner, Mathieu Foquet, Harold G Craighead, and Watt W Webb. Zero-mode waveguides for single-molecule analysis at high concentrations. *Science*, 299(5607):682–686, 2003.

[38] Henri J Lezec, A Degiron, E Devaux, RA Linke, L Martin-Moreno, FJ Garcia-Vidal, and TW Ebbesen. Beaming light from a subwavelength aperture. *science*, 297(5582):820–822, 2002.

[39] Mathieu Mivelle, Thomas S van Zanten, Lars Neumann, Niek F van Hulst, and Maria F Garcia-Parajo. Ultrabright bowtie nanoaperture antenna probes studied by single molecule fluorescence. *Nano Letters*, 12(11):5972–5978, 2012.

[40] Xiaoshu Chen, Hyeong-Ryeol Park, Matthew Pelton, Xianji Piao, Nathan C Lindquist, Hyungsoon Im, Yun Jung Kim, Jae Sung Ahn, Kwang Jun Ahn, Namkyoo Park, et al. Atomic layer lithography of wafer-scale nanogap arrays for extreme confinement of electromagnetic waves. *Nature Communications*, 4(1):1–7, 2013.

[41] Allen Taflove and Susan C Hagness. *Computational electrodynamics: the finite-difference time-domain method*. Artech house, 2005.

[42] Di M. Wu, Aitzol García-Etxarri, Alberto Salleo, and Jennifer A. Dionne. Plasmon-Enhanced Upconversion. *The Journal of Physical Chemistry Letters*, 5(22):4020–4031, November 2014.

[43] TC Cheam and Samuel Krimm. Transition dipole interaction in polypeptides: ab initio calculation of transition dipole parameters. 1984.

[44] Th Förster. Zwischenmolekulare energiewanderung und fluoreszenz. *Annalen der physik*, 437(1-2):55–75, 1948.

[45] Wen Xu, Tae Kyung Lee, Byeong-Seok Moon, Hongwei Song, Xu Chen, Byungae Chun, Young-Jin Kim, Sang Kyu Kwak, Peng Chen, and Dong-Hwan Kim. Broadband plasmonic antenna enhanced upconversion and its application in flexible fingerprint identification. *Advanced Optical Materials*, 6(6):1701119, 2018.

[46] Markus Pollnau, D R Gamelin, SR Lüthi, HU Güdel, and MP Hehlen. Power dependence of upconversion luminescence in lanthanide and transition-metal-ion systems. *Physical Review B*, 61(5):3337, 2000.

[47] Xiaogang Liu, Chun-Hua Yan, and John A Capobianco. Photon upconversion nanomaterials. *Chemical Society Reviews*, 44(6):1299–1301, 2015.

[48] Mirali Seyed Shariatdoust, Adriaan L Frencken, Ali Khademi, Amirhossein Alizadehkhaledi, Frank CJM van Veggel, and Reuven Gordon. Plasmon enhanced dual band upconverters. In *2018 IEEE 13th Nanotechnology Materials and Devices Conference (NMDC)*, pages 1–4. IEEE, 2018.

[49] Abhay Kotnala, Skyler Wheaton, and Reuven Gordon. Playing the notes of dna with light: extremely high frequency nanomechanical oscillations. *Nanoscale*, 7(6):2295–2300, 2015.

[50] Noa Hacohen, Candice JX Ip, and Reuven Gordon. Analysis of egg white protein composition with double nanohole optical tweezers. *ACS Omega*, 3(5):5266–5272, 2018.

[51] Adarsh Lalitha Ravindranath, Mirali Seyed Shariatdoust, Samuel Mathew, and Reuven Gordon. Colloidal lithography for trapping 10 nm enzymes. 11083:1108313, 2019.

[52] Dawei Li, Wei Xiong, Lijia Jiang, Zhiyong Xiao, Hossein Rabiee Golgir, Mengmeng Wang, Xi Huang, Yunshen Zhou, Zhe Lin, Jingfeng Song, Stephen Ducharme, Jean-Francois Jiang, Lan Silvain, and Yongfeng Lu Lu. Multimodal nonlinear optical imaging of MoS_2 and MoS_2-based van der Waals heterostructures. *ACS Nano*, 10(3):3766–3775, 2016.

[53] Haitao Chen, Vincent Corboliou, Alexander S Solntsev, Duk-Yong Choi, Maria A Vincenti, Domenico De Ceglia, Costantino De Angelis, Yuerui Lu, and Dragomir N Neshev. Enhanced second-harmonic generation from two-dimensional $MoSe_2$ on a silicon waveguide. *Light: Science & Applications*, 6(10):e17060–e17060, 2017.

[54] Sejeong Kim, Johannes E Fröch, Augustine Gardner, Chi Li, Igor Aharonovich, and Alexander S Solntsev. Second-harmonic generation in multilayer hexagonal boron nitride flakes. *Optics Letters*, 44(23):5792–5795, 2019.

[55] Eun-Soo Kwak, Tiberiu-Dan Onuta, Dragos Amarie, Radislav Potyrailo, Barry Stein, Stephen C Jacobson, WL Schaich, and Bogdan Dragnea. Optical trapping with integrated near-field apertures. *The Journal of Physical Chemistry B*, 108(36):13607–13612, 2004.

[56] Anna L Hagstrom, Fan Deng, and Jae-Hong Kim. Enhanced triplet–triplet annihilation upconversion in dual-sensitizer systems: translating broadband light absorption to practical solid-state materials. *ACS Photonics*, 4(1):127–137, 2016.

[57] Laszlo Frazer, Joseph K Gallaher, and TW Schmidt. Optimizing the efficiency of solar photon upconversion. *ACS Energy Letters*, 2(6):1346–1354, 2017.

[58] Guan Sun, Ruolin Chen, Yujie J Ding, and Jacob B Khurgin. Upconversion due to optical-phonon-assisted anti-stokes photoluminescence in bulk gan. *ACS Photonics*, 2(5):628–632, 2015.

[59] John-Christopher Boyer, Fiorenzo Vetrone, Louis A Cuccia, and John A Capobianco. Synthesis of colloidal upconverting $NaYF_4$ nanocrystals doped with

Er^{3+}, Yb^{3+} and Tm^{3+}, Yb^{3+} via thermal decomposition of lanthanide trifluoroacetate precursors. *ACS Photonics*, 128(23):7444–7445, 2006.

[60] Michael D Wisser, Stefan Fischer, Peter C Maurer, Noah D Bronstein, Steven Chu, A Paul Alivisatos, Alberto Salleo, and Jennifer A Dionne. Enhancing quantum yield via local symmetry distortion in lanthanide-based upconverting nanoparticles. *ACS Photonics*, 3(8):1523–1530, 2016.

[61] David J Garfield, Nicholas J Borys, Samia M Hamed, Nicole A Torquato, Cheryl A Tajon, Bining Tian, Brian Shevitski, Edward S Barnard, Yung Doug Suh, Shaul Aloni, et al. Enrichment of molecular antenna triplets amplifies upconverting nanoparticle emission. *Nature Photonics*, 12(7):402–407, 2018.

[62] Jian Hung Lin, Hao Yu Liou, Chen-Dao Wang, Chun-Yen Tseng, Ching-Ting Lee, Chu-Chi Ting, Hung-Chih Kan, and Chia Chen Hsu. Giant enhancement of upconversion fluorescence of $NaYF_4$: Yb^{3+}, Tm^{3+} nanocrystals with resonant waveguide grating substrate. *ACS Photonics*, 2(4):530–536, 2015.

[63] Emory M Chan, Daniel J Gargas, P James Schuck, and Delia J Milliron. Concentrating and recycling energy in lanthanide codopants for efficient and spectrally pure emission: the case of $NaYF_4$: Er^{3+}/Tm^{3+} upconverting nanocrystals. *The Journal of Physical Chemistry B*, 116(35):10561–10570, 2012.

[64] Freddy T Rabouw, P Tim Prins, and David J Norris. Europium-doped $NaYF_4$ nanocrystals as probes for the electric and magnetic local density of optical states throughout the visible spectral range. *Nano Letters*, 16(11):7254–7260, 2016.

[65] A Podhorodecki, J Misiewicz, J Wójcik, E Irving, and P Mascher. 1.54 μm room temperature emission from Er-doped Si nanocrystals deposited by ecr-pecvd. *Journal of Luminescence*, 121(2):230–232, 2006.

[66] Artur Podhorodecki, Grzegorz Zatryb, Lukasz W Golacki, Jan Misiewicz, Jacek Wojcik, and Peter Mascher. On the origin of emission and thermal quenching of srso: Er^{3+} films grown by ecr-pecvd. *Nanoscale Research Letters*, 8(1):98, 2013.

[67] Kianoosh Poorkazem, Amelia V Hesketh, and Timothy L Kelly. Plasmon-enhanced triplet–triplet annihilation using silver nanoplates. *The Journal of Physical Chemistry C*, 118(12):6398–6404, 2014.

[68] T Trupke, MA Green, and P Würfel. Improving solar cell efficiencies by up-conversion of sub-band-gap light. *Journal of Applied Physics*, 92(7):4117–4122, 2002.

[69] Gui Han, Min Wang, Danyang Li, Jingyi Bai, and Guowang Diao. Novel up-conversion Er, Yb-CeO_2 hollow spheres as scattering layer materials for efficient

dye-sensitized solar cells. *Solar Energy Materials and Solar Cells*, 160:54–59, 2017.

[70] D Ramachari, D Esparza, T López-Luke, VH Romero, L Perez-Mayen, E De la Rosa, and CK Jayasankar. Synthesis of co-doped Yb^{3+}-Er^{3+}: ZrO_2 upconversion nanoparticles and their applications in enhanced photovoltaic properties of quantum dot sensitized solar cells. *Journal of Alloys and Compounds*, 698:433–441, 2017.

[71] Xu Chen, Wen Xu, Hongwei Song, Cong Chen, Haiping Xia, Yongsheng Zhu, Donglei Zhou, Shaobo Cui, Qilin Dai, and Jiazhong Zhang. Highly efficient $LiYF_4$: Yb^{3+}, Er^{3+} upconversion single crystal under solar cell spectrum excitation and photovoltaic application. *ACS Applied Materials & Interfaces*, 8(14):9071–9079, 2016.

[72] Chenglin Yan, Afshin Dadvand, Federico Rosei, and Dmitrii F Perepichka. Near-ir photoresponse in new up-converting CdSe/$NaYF_4$: Yb, Er nanoheterostructures. *Journal of the American Chemical Society*, 132(26):8868–8869, 2010.

[73] Yue Huang, Eva Hemmer, Federico Rosei, and Fiorenzo Vetrone. Multifunctional liposome nanocarriers combining upconverting nanoparticles and anticancer drugs. *The Journal of Physical Chemistry B*, 120(22):4992–5001, 2016.

[74] A Shalav, BS Richards, T Trupke, KW Krämer, and Hans-Ulrich Güdel. Application of $NaYF_4$: Er^{3+} up-converting phosphors for enhanced near-infrared silicon solar cell response. *Applied Physics Letters*, 86(1):013505, 2005.

[75] Svetlana Ivanova and Fabienne Pellé. Strong 1.53 μm to NIR-VIS-UV up-conversion in Er-doped fluoride glass for high-efficiency solar cells. *JOSA B*, 26(10):1930–1938, 2009.

[76] Stefan Fischer, Noah JJ Johnson, Jothirmayanantham Pichaandi, Jan Christoph Goldschmidt, and Frank CJM van Veggel. Upconverting core-shell nanocrystals with high quantum yield under low irradiance: On the role of isotropic and thick shells. *Journal of Applied Physics*, 118(19):193105, 2015.

[77] Wei Shao, Guanying Chen, Jossana Damasco, Xianliang Wang, Aliaksandr Kachynski, Tymish Y Ohulchanskyy, Chunhui Yang, Hans Ågren, and Paras N Prasad. Enhanced upconversion emission in colloidal ($NaYF_4$: Er^{3+})/$NaYF_4$ core/shell nanoparticles excited at 1523 nm. *Optics letters*, 39(6):1386–1389, 2014.

[78] Seng C Goh. Red, green and blue upconversions in erbium-doped fluorozirconate glass. *Journal of Non-Crystalline Solids*, 161:227–230, 1993.

[79] Kunta Yoshikawa, Hayato Kawasaki, Wataru Yoshida, Toru Irie, Katsunori Konishi, Kunihiro Nakano, Toshihiko Uto, Daisuke Adachi, Masanori Kanematsu, Hisashi Uzu, and Kenji Yamamoto. Silicon heterojunction solar cell with interdigitated back contacts for a photoconversion efficiency over 26%. *Nature Energy*, 2:17032, 2017.

[80] Daisuke Adachi, José Luis Hernández, and Kenji Yamamoto. Impact of carrier recombination on fill factor for large area heterojunction crystalline silicon solar cell with 25.1% efficiency. *Applied Physics Letters*, 107(23):233506, 2015.

[81] Martin A Green, Yoshihiro Hishikawa, Ewan D Dunlop, Dean H Levi, Jochen Hohl-Ebinger, and Anita WY Ho-Baillie. Solar cell efficiency tables (version 52). *Progress in Photovoltaics: Research and Applications*, 26(7):427–436, 2018.

[82] Mark Wanlass. Systems and methods for advanced ultra-high-performance inp solar cells, March 7 2017. US Patent 9,590,131.

[83] PJ Schuck, DP Fromm, A Sundaramurthy, GS Kino, and WE Moerner. Improving the mismatch between light and nanoscale objects with gold bowtie nanoantennas. *Physical Review Letters*, 94(1):017402, 2005.

[84] Pascal Anger, Palash Bharadwaj, and Lukas Novotny. Enhancement and quenching of single-molecule fluorescence. *Physical Review Letters*, 96(11):113002, 2006.

[85] Ngoc-Vu Hoang, Antonio Pereira, Hai Son Nguyen, Emmanuel Drouard, Bernard Moine, Thierry Deschamps, Regis Orobtchouk, Anne Pillonnet, and Christian Seassal. Giant enhancement of luminescence down-shifting by a doubly resonant rare-earth-doped photonic metastructure. *ACS Photonics*, 4(7):1705–1712, 2017.

[86] Niccolò T Michieli, Boris Kalinic, Carlo Scian, Tiziana Cesca, and Giovanni Mattei. Emission rate modification and quantum efficiency enhancement of Er^{3+} emitters by near-field coupling with nanohole arrays. *ACS Photonics*, 2018.

[87] Ali Rafiei Miandashti, Martin E Kordesch, and Hugh H Richardson. Effect of temperature and gold nanoparticle interaction on the lifetime and luminescence of $NaYF_4$: Yb^{3+}: Er^{3+} upconverting nanoparticles. *ACS Photonics*, 4(7):1864–1869, 2017.

[88] Yue Huang, Federico Rosei, and Fiorenzo Vetrone. A single multifunctional nanoplatform based on upconversion luminescence and gold nanorods. *Nanoscale*, 7(12):5178–5185, 2015.

[89] Hua Zhang, Yujing Li, Ivan A Ivanov, Yongquan Qu, Yu Huang, and Xiangfeng Duan. Plasmonic modulation of the upconversion fluorescence in $NaYF_4$: Yb/Tm hexaplate nanocrystals using gold nanoparticles or nanoshells. *Angewandte Chemie*, 122(16):2927–2930, 2010.

[90] Gururaj V Naik, Alex J Welch, Justin A Briggs, Michelle L Solomon, and Jennifer A Dionne. Hot-carrier-mediated photon upconversion in metal-decorated quantum wells. *Nano letters*, 17(8):4583–4587, 2017.

[91] Huanjun Chen, Lei Shao, Qian Li, and Jianfang Wang. Gold nanorods and their plasmonic properties. *Chemical Society Reviews*, 42(7):2679–2724, 2013.

[92] Tim F Schulze and Timothy W Schmidt. Photochemical upconversion: present status and prospects for its application to solar energy conversion. *Energy & Environmental Science*, 8(1):103–125, 2015.

[93] John-Christopher Boyer and Frank CJM Van Veggel. Absolute quantum yield measurements of colloidal $NaYF_4$: Er^{3+}, Yb^{3+} upconverting nanoparticles. *Nanoscale*, 2(8):1417–1419, 2010.

[94] J Kalkman, L Kuipers, A Polman, and H Gersen. Coupling of er ions to surface plasmons on ag. *Applied Physics Letters*, 86(4):041113, 2005.

[95] Sinan Karaveli and Rashid Zia. Strong enhancement of magnetic dipole emission in a multilevel electronic system. *Optics letters*, 35(20):3318–3320, 2010.

[96] Sinan Karaveli and Rashid Zia. Spectral tuning by selective enhancement of electric and magnetic dipole emission. *Physical Review Letters*, 106(19):193004, 2011.

[97] Dongfang Li, Mingming Jiang, Sébastien Cueff, Christopher M Dodson, Sinan Karaveli, and Rashid Zia. Quantifying and controlling the magnetic dipole contribution to 1.5- μ m light emission in erbium-doped yttrium oxide. *Physical Review B*, 89(16):161409, 2014.

[98] H Mertens and A Polman. Plasmon-enhanced erbium luminescence. *Applied Physics Letters*, 89(21):211107, 2006.

[99] Liang-Chieh Ma, Ramkumar Subramanian, Hong-Wen Huang, Vishva Ray, Choong-Un Kim, and Seong Jin Koh. Electrostatic funneling for precise nanoparticle placement: a route to wafer-scale integration. *Nano letters*, 7(2):439–445, 2007.

[100] Kohei Imura, Hiromi Okamoto, Mohammad K Hossain, and Masahiro Kitajima. Visualization of localized intense optical fields in single gold- nanoparticle assemblies and ultrasensitive raman active sites. *Nano letters*, 6(10):2173–2176, 2006.

[101] Felicia Toderas, Monica Baia, Lucian Baia, and Simion Astilean. Controlling gold nanoparticle assemblies for efficient surface-enhanced raman scattering and localized surface plasmon resonance sensors. *Nanotechnology*, 18(25):255702, 2007.

[102] Marjan Saboktakin, Xingchen Ye, Soong Ju Oh, Sung-Hoon Hong, Aaron T Fafarman, Uday K Chettiar, Nader Engheta, Christopher B Murray, and Cherie R Kagan. Metal-enhanced upconversion luminescence tunable through metal nanoparticle–nanophosphor separation. *ACS Nano*, 6(10):8758–8766, 2012.

[103] Stefan Schietinger, Thomas Aichele, Hai-Qiao Wang, Thomas Nann, and Oliver Benson. Plasmon-enhanced upconversion in single $NaYF_4$: Yb^{3+}/Er^{3+} codoped nanocrystals. *Nano letters*, 10(1):134–138, 2009.

[104] Weihua Zhang, Fei Ding, and Stephen Y Chou. Large enhancement of upconversion luminescence of $NaYF_4$: Yb^{3+}/Er^{3+} nanocrystal by 3d plasmonic nano-antennas. *Advanced Materials*, 24(35), 2012.

[105] Ewold Verhagen, L Kuipers, and Albert Polman. Field enhancement in metallic subwavelength aperture arrays probed by erbium upconversion luminescence. *Optics Express*, 17(17):14586–14598, 2009.

[106] Zhengquan Li and Yong Zhang. An efficient and user-friendly method for the synthesis of hexagonal-phase $NaYF_4$: Yb, Er/Tm nanocrystals with controllable shape and upconversion fluorescence. *Nanotechnology*, 19(34):345606, 2008.

[107] K Okamoto and S Kawata. Radiation force exerted on subwavelength particles near a nanoaperture. *Physical Review Letters*, 83(22):4534, 1999.

[108] Weihua Zhang, Lina Huang, Christian Santschi, and Olivier JF Martin. Trapping and sensing 10 nm metal nanoparticles using plasmonic dipole antennas. *Nano Letters*, 10(3):1006–1011, 2010.

[109] Brian J Roxworthy, Kaspar D Ko, Anil Kumar, Kin Hung Fung, Edmond KC Chow, Gang Logan Liu, Nicholas X Fang, and Kimani C Toussaint Jr. Application of plasmonic bowtie nanoantenna arrays for optical trapping, stacking, and sorting. *Nano Letters*, 12(2):796–801, 2012.

[110] Maurizio Righini, Anna S Zelenina, Christian Girard, and Romain Quidant. Parallel and selective trapping in a patterned plasmonic landscape. *Nature Physics*, 3(7):477, 2007.

[111] Maurizio Righini, Giovanni Volpe, Christian Girard, Dmitri Petrov, and Romain Quidant. Surface plasmon optical tweezers: tunable optical manipulation in the femtonewton range. *Physical Review Letters*, 100(18):186804, 2008.

[112] M Righini, P Ghenuche, S Cherukulappurath, Viktor Myroshnychenko, Francisco Javier Garcia de Abajo, and Romain Quidant. Nano-optical trapping of rayleigh particles and escherichia coli bacteria with resonant optical antennas. *Nano Letters*, 9(10):3387–3391, 2009.

[113] Haitian Xu, Steven Jones, Byoung-Chul Choi, and Reuven Gordon. Characterization of individual magnetic nanoparticles in solution by double nanohole

optical tweezers. *Nano Letters*, 16(4):2639–2643, 2016.

[114] Russell A Jensen, I-Chun Huang, Ou Chen, Jennifer T Choy, Thomas S Bischof, Marko Loncar, and Moungi G Bawendi. Optical trapping and two-photon excitation of colloidal quantum dots using bowtie apertures. *ACS Photonics*, 3(3):423–427, 2016.

[115] J Berthelot, SS Aćimović, ML Juan, MP Kreuzer, J Renger, and R Quidant. Three-dimensional manipulation with scanning near-field optical nanotweezers. *Nature Nanotechnology*, 9(4):295, 2014.

[116] Chang Chen, Mathieu L Juan, Yi Li, Guido Maes, Gustaaf Borghs, Pol Van Dorpe, and Romain Quidant. Enhanced optical trapping and arrangement of nano-objects in a plasmonic nanocavity. *Nano Letters*, 12(1):125–132, 2011.

[117] Skyler Wheaton and Reuven Gordon. Molecular weight characterization of single globular proteins using optical nanotweezers. *Analyst*, 140(14):4799–4803, 2015.

[118] Thomas W Ebbesen, Henri J Lezec, HF Ghaemi, Tineke Thio, and Peter A Wolff. Extraordinary optical transmission through sub-wavelength hole arrays. *Nature*, 391(6668):667, 1998.

[119] Daehan Yoo, Kargal L Gurunatha, Han-Kyu Choi, Daniel A Mohr, Christopher T Ertsgaard, Reuven Gordon, and Sang-Hyun Oh. Low-power optical trapping of nanoparticles and proteins with resonant coaxial nanoaperture using 10 nm gap. *Nano Letters*, 18(6):3637–3642, 2018.

[120] Prashant Nagpal, Nathan C Lindquist, Sang-Hyun Oh, and David J Norris. Ultrasmooth patterned metals for plasmonics and metamaterials. *Science*, 325(5940):594–597, 2009.

[121] Ana Zehtabi-Oskuie, Aurora A Zinck, Ryan M Gelfand, and Reuven Gordon. Template stripped double nanohole in a gold film for nano-optical tweezers. *Nanotechnology*, 25(49):495301, 2014.

[122] Jean-François Masson, Marie-Pier Murray-Méthot, and Ludovic S Live. Nanohole arrays in chemical analysis: manufacturing methods and applications. *Analyst*, 135(7):1483–1489, 2010.

[123] John C Hulteen and Richard P Van Duyne. Nanosphere lithography: A materials general fabrication process for periodic particle array surfaces. *Journal of Vacuum Science & Technology A: Vacuum, Surfaces, and Films*, 13(3):1553–1558, 1995.

[124] Marie-Pier Murray-Méthot, Mathieu Ratel, and Jean-Francois Masson. Optical properties of au, ag, and bimetallic au on ag nanohole arrays. *The Journal of*

Physical Chemistry C, 114(18):8268–8275, 2010.

[125] Si Hoon Lee, Kyle C Bantz, Nathan C Lindquist, Sang-Hyun Oh, and Christy L Haynes. Self-assembled plasmonic nanohole arrays. *Langmuir*, 25(23):13685–13693, 2009.

[126] Seung-Man Yang, Se Gyu Jang, Dae-Geun Choi, Sarah Kim, and Hyung Kyun Yu. Nanomachining by colloidal lithography. *Small*, 2(4):458–475, 2006.

[127] Alfred Plettl, Fabian Enderle, Marc Saitner, Achim Manzke, Christian Pfahler, Stefan Wiedemann, and Paul Ziemann. Non-close-packed crystals from self-assembled polystyrene spheres by isotropic plasma etching: Adding flexibility to colloid lithography. *Advanced Functional Materials*, 19(20):3279–3284, 2009.

[128] Renee R Frontiera, Natalie L Gruenke, and Richard P Van Duyne. Fano-like resonances arising from long-lived molecule-plasmon interactions in colloidal nanoantennas. *Nano Letters*, 12(11):5989–5994, 2012.

[129] Gang Zhang and Dayang Wang. Fabrication of heterogeneous binary arrays of nanoparticles via colloidal lithography. *Journal of the American Chemical Society*, 130(17):5616–5617, 2008.

[130] Arika Pravitasari, Maelani Negrito, Kristin Light, Wei-Shun Chang, Stephan Link, Matthew Sheldon, and James D Batteas. Using particle lithography

to tailor the architecture of au nanoparticle plasmonic nanoring arrays. *The Journal of Physical Chemistry B*, 122(2):730–736, 2017.

[131] Tiberiu-Dan Onuta, Matthias Waegele, Christopher C DuFort, William L Schaich, and Bogdan Dragnea. Optical field enhancement at cusps between adjacent nanoapertures. *Nano Letters*, 7(3):557–564, 2007.

[132] Kaili Jiang, Qunqing Li, and Shoushan Fan. Nanotechnology: spinning continuous carbon nanotube yarns. *Nature*, 419(6909):801, 2002.

[133] Cyriaque Genet and Thomas W Ebbesen. Light in tiny holes. In *Nanoscience And Technology: A Collection of Reviews from Nature Journals*, pages 205–212. World Scientific, 2010.

[134] Maxim Belkin, Shu-Han Chao, Magnus P Jonsson, Cees Dekker, and Aleksei Aksimentiev. Plasmonic nanopores for trapping, controlling displacement, and sequencing of dna. *ACS Nano*, 9(11):10598–10611, 2015.

[135] Daniel Verschueren, Xin Shi, and Cees Dekker. Nano-optical tweezing of single proteins in plasmonic nanopores. *Small Methods*, page 1800465, 2019.

[136] Zachary Roelen, José A Bustamante, Autumn Carlsen, Aidan Baker-Murray, and Vincent Tabard-Cossa. Instrumentation for low noise nanopore-based ionic current recording under laser illumination. *Review of Scientific Instruments*, 89(1):015007, 2018.

[137] Erik C Yusko, Jay M Johnson, Sheereen Majd, Panchika Prangkio, Ryan C Rollings, Jiali Li, Jerry Yang, and Michael Mayer. Controlling protein translocation through nanopores with bio-inspired fluid walls. *Nature Nanotechnology*, 6(4):253, 2011.

[138] Erik C Yusko, Brandon R Bruhn, Olivia M Eggenberger, Jared Houghtaling, Ryan C Rollings, Nathan C Walsh, Santoshi Nandivada, Mariya Pindrus, Adam R Hall, David Sept, Jiali Li, Devendra S Kalonia, and Michael Mayer. Real-time shape approximation and fingerprinting of single proteins using a nanopore. *Nature Nanotechnology*, 12(4):360, 2017.

[139] Wenhong Li, Nicholas AW Bell, Silvia Hernandez-Ainsa, Vivek V Thacker, Alana M Thackray, Raymond Bujdoso, and Ulrich F Keyser. Single protein molecule detection by glass nanopores. *ACS Nano*, 7(5):4129–4134, 2013.

[140] Stefan Howorka, Stephen Cheley, and Hagan Bayley. Sequence-specific detection of individual dna strands using engineered nanopores. *Nature Biotechnology*, 19(7):636, 2001.

[141] Grégory F Schneider, Stefan W Kowalczyk, Victor E Calado, Grégory Pandraud, Henny W Zandbergen, Lieven MK Vandersypen, and Cees Dekker. Dna translocation through graphene nanopores. *Nano Letters*, 10(8):3163–3167, 2010.

[142] Peng Chen, Jiajun Gu, Eric Brandin, Young-Rok Kim, Qiao Wang, and Daniel Branton. Probing single dna molecule transport using fabricated nanopores. *Nano Letters*, 4(11):2293–2298, 2004.

[143] Stijn Van Dorp, Ulrich F Keyser, Nynke H Dekker, Cees Dekker, and Serge G Lemay. Origin of the electrophoretic force on dna in solid-state nanopores. *Nature Physics*, 5(5):347, 2009.

[144] Grégory F Schneider and Cees Dekker. Dna sequencing with nanopores. *Nature Biotechnology*, 30(4):326, 2012.

[145] Kyle Briggs, Harold Kwok, and Vincent Tabard-Cossa. Automated fabrication of 2-nm solid-state nanopores for nucleic acid analysis. *Small*, 10(10):2077–2086, 2014.

[146] Paolo Cadinu, Giulia Campolo, Sergii Pud, Wayne Yang, Joshua B Edel, Cees Dekker, and Aleksandar P Ivanov. Double barrel nanopores as a new tool for controlling single-molecule transport. *Nano Letters*, 18(4):2738–2745, 2018.

[147] Breton Hornblower, Amy Coombs, Richard D Whitaker, Anatoly Kolomeisky, Stephen J Picone, Amit Meller, and Mark Akeson. Single-molecule analysis of dna-protein complexes using nanopores. *Nature Methods*, 4(4):315, 2007.

[148] Stefan W Kowalczyk, Adam R Hall, and Cees Dekker. Detection of local protein structures along dna using solid-state nanopores. *Nano Letters*, 10(1):324–328, 2009.

[149] Benjamin N Miles, Aleksandar P Ivanov, Kerry A Wilson, Fatma Doğan, Deanpen Japrung, and Joshua B Edel. Single molecule sensing with solid-state nanopores: novel materials, methods, and applications. *Chemical Society Reviews*, 42(1):15–28, 2013.

[150] Sergii Pud, Daniel Verschueren, Nikola Vukovic, Calin Plesa, Magnus P Jonsson, and Cees Dekker. Self-aligned plasmonic nanopores by optically controlled dielectric breakdown. *Nano Letters*, 15(10):7112–7117, 2015.

[151] Dayang Wang and Helmuth Möhwald. Template-directed colloidal self-assembly–the route to 'top-down'nanochemical engineering. *Journal of Materials Chemistry*, 14(4):459–468, 2004.

[152] Brian Stern, Xingchen Ji, Yoshitomo Okawachi, Alexander L Gaeta, and Michal Lipson. Battery-operated integrated frequency comb generator. *Nature*, 562(7727):401–405, 2018.

[153] Alexander L Gaeta, Michal Lipson, and Tobias J Kippenberg. Photonic-chip-based frequency combs. *Nature Photonics*, 13(3):158–169, 2019.

[154] Changjun Min, Pei Wang, Chunchong Chen, Yan Deng, Yonghua Lu, Hai Ming, Tingyin Ning, Yueliang Zhou, and Guozhen Yang. All-optical switching in subwavelength metallic grating structure containing nonlinear optical materials. *Optics Letters*, 33(8):869–871, 2008.

[155] D Cotter, RJ Manning, KJ Blow, AD Ellis, AE Kelly, D Nesset, ID Phillips, AJ Poustie, and DC Rogers. Nonlinear optics for high-speed digital information processing. *Science*, 286(5444):1523–1528, 1999.

[156] Dalziel J Wilson, Katharina Schneider, Simon Hönl, Miles Anderson, Yannick Baumgartner, Lukas Czornomaz, Tobias J Kippenberg, and Paul Seidler. Integrated gallium phosphide nonlinear photonics. *Nature Photonics*, 14(1):57–62, 2020.

[157] Fritjof Helmchen and Winfried Denk. Deep tissue two-photon microscopy. *Nature Methods*, 2(12):932–940, 2005.

[158] Warren R Zipfel, Rebecca M Williams, Richard Christie, Alexander Yu Nikitin, Bradley T Hyman, and Watt W Webb. Live tissue intrinsic emission microscopy using multiphoton-excited native fluorescence and second harmonic generation. *Proceedings of the National Academy of Sciences*, 100(12):7075–7080, 2003.

[159] Paul J Campagnola and Leslie M Loew. Second-harmonic imaging microscopy for visualizing biomolecular arrays in cells, tissues and organisms. *Nature*

Biotechnology, 21(11):1356–1360, 2003.

[160] Chandriker Kavir Dass, Hoyeong Kwon, Shivashankar Vangala, Evan M Smith, Justin W Cleary, Junpeng Guo, Andrea Alù, and Joshua R Hendrickson. Gap-plasmon-enhanced second-harmonic generation in epsilon-near-zero nanolayers. *ACS Photonics*, 7(1):174–179, 2019.

[161] Kai Chen, Cemil Durak, James R Heflin, and Hans D Robinson. Plasmon-enhanced second-harmonic generation from ionic self-assembled multilayer films. *Nano Letters*, 7(2):254–258, 2007.

[162] Ryo Naraoka, Haruki Okawa, Kazuhiko Hashimoto, and Kotaro Kajikawa. Surface plasmon resonance enhanced second-harmonic generation in Kretschmann configuration. *Optics Communications*, 248(1-3):249–256, 2005.

[163] Kai-Qiang Lin, Sebastian Bange, and John M Lupton. Quantum interference in second-harmonic generation from monolayer WSe_2. *Nature Physics*, 15(3):242–246, 2019.

[164] Chiara Trovatello, Andrea Marini, Xinyi Xu, Changhwan Lee, Fang Liu, Nicola Curreli, Cristian Manzoni, Stefano Dal Conte, Kaiyuan Yao, Alessandro Ciattoni, James Hone, Xiaoyang Zhu, P. James Schuck, and Giulio Cerullo. Optical parametric amplification by monolayer transition metal dichalcogenides. *Nature Photonics*, 15(1):6–10, 2021.

[165] Nils Bernhardt, Sejeong Kim, Johannes E Fröch, Simon JU White, Ngoc My Hanh Duong, Zhe He, Bo Chen, Jin Liu, Igor Aharonovich, and Alexander S Solntsev. Large few-layer hexagonal boron nitride flakes for nonlinear optics. *Optics Letters*, 46(3):564–567, 2021.

[166] Yu Yao, Raji Shankar, Patrick Rauter, Yi Song, Jing Kong, Marko Lončar, and Federico Capasso. High-responsivity mid-infrared graphene detectors with antenna-enhanced photocarrier generation and collection. *Nano Letters*, 14(7):3749–3754, 2014.

[167] Kaiyuan Yao, Emanuil Yanev, Hsun-Jen Chuang, Matthew R Rosenberger, Xinyi Xu, Thomas Darlington, Kathleen M McCreary, Aubrey T Hanbicki, Kenji Watanabe, Takashi Taniguchi, et al. Continuous wave sum frequency generation and imaging of monolayer and heterobilayer two-dimensional semiconductors. *ACS Nano*, 14(1):708–714, 2019.

[168] Kaiyuan Yao, Nathan R Finney, Jin Zhang, Samuel L Moore, Lede Xian, Nicolas Tancogne-Dejean, Fang Liu, Jenny Ardelean, Xinyi Xu, Dorri Halbertal, et al. Enhanced tunable second harmonic generation from twistable interfaces and vertical superlattices in boron nitride homostructures. *Science Advances*, 7(10):eabe8691, 2021.

[169] Yilei Li, Yi Rao, Kin Fai Mak, Yumeng You, Shuyuan Wang, Cory R Dean, and Tony F Heinz. Probing symmetry properties of few-layer MoS_2 and h-BN

by optical second-harmonic generation. *Nano Letters*, 13(7):3329–3333, 2013.

[170] Rana Faryad Ali and Byron D Gates. Synthesis of lithium niobate nanocrystals with size focusing through an ostwald ripening process. *Chemistry of Materials*, 30(6):2028–2035, 2018.

[171] Rana Faryad Ali, Matthew Bilton, and Byron D Gates. One-pot synthesis of sub-10 nm linbo 3 nanocrystals exhibiting a tunable optical second harmonic response. *Nanoscale Advances*, 1(6):2268–2275, 2019.

[172] Zhe Xu, Wuzhou Song, and Kenneth B Crozier. Direct particle tracking observation and brownian dynamics simulations of a single nanoparticle optically trapped by a plasmonic nanoaperture. *ACS Photonics*, 5(7):2850–2859, 2018.

[173] Amirhossein Alizadehkhaledi, Adriaan L Frencken, Frank CJM van Veggel, and Reuven Gordon. Isolating nanocrystals with an individual erbium emitter: A route to a stable single-photon source at 1550 nm wavelength. *Nano Letters*, 20(2):1018–1022, 2019.

[174] Abhay Kotnala, Pavana Siddhartha Kollipara, Jingang Li, and Yuebing Zheng. Overcoming diffusion-limited trapping in nanoaperture tweezers using opto-thermal-induced flow. *Nano Letters*, 20(1):768–779, 2019.

[175] Quanbo Jiang, Benoît Rogez, Jean-Benoît Claude, Guillaume Baffou, and Jérôme Wenger. Quantifying the role of the surfactant and the thermophoretic force in plasmonic nano-optical trapping. *Nano Letters*, 20(12):8811–8817, 2020.

[176] Xiaobo Han, Kai Wang, Patrick D Persaud, Xiangyuan Xing, Weiwei Liu, Hua Long, Fang Li, Bing Wang, Mahi R Singh, and Peixiang Lu. Harmonic resonance enhanced second-harmonic generation in the monolayer WS_2–Ag nanocavity. *ACS Photonics*, 7(3):562–568, 2020.

[177] Murat Sivis, Nicolas Pazos-Perez, Renwen Yu, Ramon Alvarez-Puebla, F Javier García de Abajo, and Claus Ropers. Continuous-wave multiphoton photoemission from plasmonic nanostars. *Communications Physics*, 1(1):1–6, 2018.

[178] Nicola Palombo Blascetta, Matz Liebel, Xiaobo Lu, Takashi Taniguchi, Kenji Watanabe, Dmitri K Efetov, and Niek F van Hulst. Nanoscale imaging and control of hexagonal boron nitride single photon emitters by a resonant nanoantenna. *Nano Letters*, 20(3):1992–1999, 2020.

[179] Peter B Johnson and R-WJPrB Christy. Optical constants of the noble metals. *Physical Review B*, 6(12):4370, 1972.

[180] Akash Laturia, Maarten L Van de Put, and William G Vandenberghe. Dielectric properties of hexagonal boron nitride and transition metal dichalcogenides:

from monolayer to bulk. *NPJ 2D Materials and Applications*, 2(1):1–7, 2018.

[181] Guokui Liu and Bernard Jacquier, editors. *Spectroscopic Properties of Rare Earths in Optical Materials*. Springer Series in Materials Science. Springer-Verlag, Berlin Heidelberg, 2005.

[182] R Kolesov, K Xia, R Reuter, R Stöhr, A Zappe, J Meijer, PR Hemmer, and J Wrachtrup. Optical detection of a single rare-earth ion in a crystal. *Nature Communications*, 3(1):1–7, 2012.

[183] Roman Kolesov, Kangwei Xia, Rolf Reuter, Mohammad Jamali, Rainer Stöhr, Tugrul Inal, Petr Siyushev, and Jörg Wrachtrup. Mapping spin coherence of a single rare-earth ion in a crystal onto a single photon polarization state. *Physical Review Letters*, 111(12):120502, 2013.

[184] Kangwei Xia, Roman Kolesov, Ya Wang, Petr Siyushev, Rolf Reuter, Thomas Kornher, Nadezhda Kukharchyk, Andreas D Wieck, Bruno Villa, Sen Yang, et al. All-optical preparation of coherent dark states of a single rare earth ion spin in a crystal. *Physical Review Letters*, 115(9):093602, 2015.

[185] Nicolas Gisin. How far can one send a photon? *Frontiers of Physics*, 10(6):1–8, 2015.

[186] Matthew D Eisaman, Jingyun Fan, Alan Migdall, and Sergey V Polyakov. Invited review article: Single-photon sources and detectors. *Review of Scientific Instruments*, 82(7):071101, 2011.

[187] Yu-Ao Chen, Qiang Zhang, Teng-Yun Chen, Wen-Qi Cai, Sheng-Kai Liao, Jun Zhang, Kai Chen, Juan Yin, Ji-Gang Ren, Zhu Chen, Sheng-Long Han, Qing Yu, Ken Liang, Fei Zhou, Xiao Yuan, Mei-Sheng Zhao, Tian-Yin Wang, Xiao Jiang, Liang Zhang, Wei-Yue Liu, Yang Li, Qi Shen, Yuan Cao, Chao-Yang Lu, Rong Shu, Jian-Yu Wang, Li Li, Nai-Le Liu, Feihu Xu, Xiang-Bin Wang, Cheng-Zhi Peng, and Jian-Wei Pan. An integrated space-to-ground quantum communication network over 4,600 kilometres. *Nature*, 589(7841):214–219, 2021.

[188] Emmanuel Desurvire and Michael N Zervas. Erbium-doped fiber amplifiers: principles and applications. *Physics Today*, 48(2):56, 1995.

[189] AM Dibos, M Raha, CM Phenicie, and Jeffrey Douglas Thompson. Atomic source of single photons in the telecom band. *Physical Review Letters*, 120(24):243601, 2018.

[190] W Redjem, A Durand, T Herzig, A Benali, S Pezzagna, J Meijer, A Yu Kuznetsov, HS Nguyen, Sébastien Cueff, J-M Gérard, et al. Single artificial atoms in silicon emitting at telecom wavelengths. *Nature Electronics*, 3(12):738–743, 2020.

[191] Karin Groot-Berning, Thomas Kornher, Georg Jacob, Felix Stopp, Samuel T Dawkins, Roman Kolesov, Jörg Wrachtrup, Kilian Singer, and Ferdinand Schmidt-Kaler. Deterministic single-ion implantation of rare-earth ions for nanometer-resolution color-center generation. *Physical Review Letters*, 123(10):106802, 2019.

[192] Stefan A. Maier. *Plasmonics: Fundamentals and Applications*. Springer, New York, 2007.

[193] Ayelet Teitelboim, Bining Tian, David J Garfield, Angel Fernandez-Bravo, Adam C Gotlin, P James Schuck, Bruce E Cohen, and Emory M Chan. Energy transfer networks within upconverting nanoparticles are complex systems with collective, robust, and history-dependent dynamics. *The Journal of Physical Chemistry C*, 123(4):2678–2689, 2019.

[194] Tian Zhong, Jonathan M Kindem, John G Bartholomew, Jake Rochman, Ioana Craiciu, Varun Verma, Sae Woo Nam, Francesco Marsili, Matthew D Shaw, Andrew D Beyer, et al. Optically addressing single rare-earth ions in a nanophotonic cavity. *Physical Review Letters*, 121(18):183603, 2018.

[195] Bo Zhou, Bingyang Shi, Dayong Jin, and Xiaogang Liu. Controlling upconversion nanocrystals for emerging applications. *Nature Nanotechnology*, 10(11):924–936, 2015.

[196] Marjan Saboktakin, Xingchen Ye, Uday K Chettiar, Nader Engheta, Christopher B Murray, and Cherie R Kagan. Plasmonic enhancement of nanophosphor upconversion luminescence in au nanohole arrays. *ACS Nano*, 7(8):7186–7192, 2013.

[197] Eun-Soo Kwak, Tiberiu-Dan Onuta, Dragos Amarie, Radislav Potyrailo, Barry Stein, Stephen C Jacobson, WL Schaich, and Bogdan Dragnea. Optical trapping with integrated near-field apertures. *The Journal of Physical Chemistry B*, 108(36):13607–13612, 2004.

[198] Muhammad Usman Raza, Sai Santosh Sasank Peri, Liang-Chieh Ma, Samir M Iqbal, and George Alexandrakis. Self-induced back action actuated nanopore electrophoresis (SANE). *Nanotechnology*, 29(43):435501, 2018.

[199] J Freek Suyver, Judith Grimm, MK Van Veen, Daniel Biner, KW Krämer, and Hans-Ulrich Güdel. Upconversion spectroscopy and properties of $NaYF_4$ doped with Er^{3+}, Tm^{3+} and/or Yb^{3+}. *Journal of Luminescence*, 117(1):1–12, 2006.

[200] Antoine Lesuffleur, L Kiran Swaroop Kumar, and Reuven Gordon. Enhanced second harmonic generation from nanoscale double-hole arrays in a gold film. *Applied Physics Letters*, 88(26):261104, 2006.

[201] A Lesuffleur, LKS Kumar, AG Brolo, KL Kavanagh, and R Gordon. Apex-enhanced raman spectroscopy using double-hole arrays in a gold film. *The*

Journal of Physical Chemistry C, 111(6):2347–2350, 2007.

[202] Feng Wang, Juan Wang, and Xiaogang Liu. Direct evidence of a surface quenching effect on size-dependent luminescence of upconversion nanoparticles. *Angewandte Chemie International Edition*, 49(41):7456–7460, 2010.

[203] Abhay Kotnala, Damon DePaoli, and Reuven Gordon. Sensing nanoparticles using a double nanohole optical trap. *Lab on a Chip*, 13(20):4142–4146, 2013.

[204] Abhay Kotnala and Reuven Gordon. Quantification of High-Efficiency Trapping of Nanoparticles in a Double Nanohole Optical Tweezer. *Nano Letters*, 14(2):853–856, February 2014.

[205] Changhwan Lee, Emma Z Xu, Yawei Liu, Ayelet Teitelboim, Kaiyuan Yao, Angel Fernandez-Bravo, Agata M Kotulska, Sang Hwan Nam, Yung Doug Suh, Artur Bednarkiewicz, et al. Giant nonlinear optical responses from photon-avalanching nanoparticles. *Nature*, 589(7841):230–235, 2021.

[206] E Snoeks, A Lagendijk, and A Polman. Measuring and modifying the spontaneous emission rate of erbium near an interface. *Physical Review Letters*, 74(13):2459, 1995.

[207] John David Jackson. Classical electrodynamics, 1999.

[208] Edward M Purcell, Henry Cutler Torrey, and Robert V Pound. Resonance absorption by nuclear magnetic moments in a solid. *Physical review*, 69(1-2):37, 1946.

Appendix A

Harvesting dual-wavelength excitation with plasmon-enhanced emission from upconverting nanoparticles [10].

Originally published:

M. S. Shariatdoust, A. L. Frencken, A. Khademi, A. Alizadehkhaledi, F. C. van Veggel, R. Gordon, Harvesting dual-wavelength excitation with plasmon-enhanced emission from upconverting nanoparticles, ACS Photonics, 5(9), 3507-3512 (2018).

A.1 Harvesting dual-wavelength excitation with plasmon-enhanced emission from upconverting nanoparticles

A.1.1 Abstract

We demonstrate dual-wavelength (1210 and 1520 nm) excitation of upconverter nanoparticles (Er-doped nanoparticles) with plasmon-enhanced emission. Gold nanorods of 25 nm diameter with resonances at 808 nm and at 980 nm selectively enhance the upconversion emission of 2% erbium-doped NaYF4 nanoparticles at 808 nm and at 980 nm. No upconversion is seen for 1210 nm excitation alone, and 1520 nm excitation alone provides lower upconversion. The sequential 1520 and 1210 nm absorption yields the most upconversion, and the power dependence of emission supports the sequential absorption mechanism. This provides a promising avenue for harvesting from the two strongest infrared bands of the solar spectrum with selective emission tuned to either the Si or GaAs band gap.

A.1.2 Paper content

Upconversion is an optical process that combines the energy from low energy photons to provide higher energy photon emission. It is typically more efficient than nonlinear

harmonic generation, and so it is of interest for solar harvesting applications whereby photons that do not have sufficient energy to be absorbed can be converted into higher energy photons [15, 56, 57, 20, 58]. Lanthanides have long-lived electronic excitations that can be used as intermediate states for upconversion. While having typically lower efficiency than bulk, lanthanide doped nanoparticles are well suited for simple processing and plasmon coupling schemes [59, 21, 60, 61, 16, 62, 63, 64, 65, 66] Beside rare-earth lanthanides, dye-sensitizers using triplet-triplet annihilation is another system that benefits from plasmonic enhancement [67, 68].

Most work has focused on 980 nm excitation of Yb sensitized Er; however, for the dominant silicon based solar cell technology, upconversion for wavelengths larger than the bandgap wavelength (>1100 nm) is desired [69, 70, 71, 72, 73]. Several works have reported on ∼1520 nm upconversion of Er for emission at 980, 808, 655, 544 nm [22, 74, 75, 76, 77]. This has the disadvantage of harvesting only a small part of the IR solar spectrum. There is also the interesting possibility of sequential absorption of a 1520 nm photon from $I_{15/2}$ – $I_{13/2}$ followed by a 1210 nm photon from $I_{13/2}$ — $F_{9/2}$ and subsequent upconversion. We have found only one work where an analogous 1130 nm + 1500 nm barium vapor laser was used to achieve this sequential excitation and upconversion of Er doped fluorzirconate in a preform [78]. The excitation at 1130 nm is not ideal, however, since it is in the minimum of the solar excitation spectrum.

Figure A.1 shows the solar spectrum and the sequential excitation and upconver-

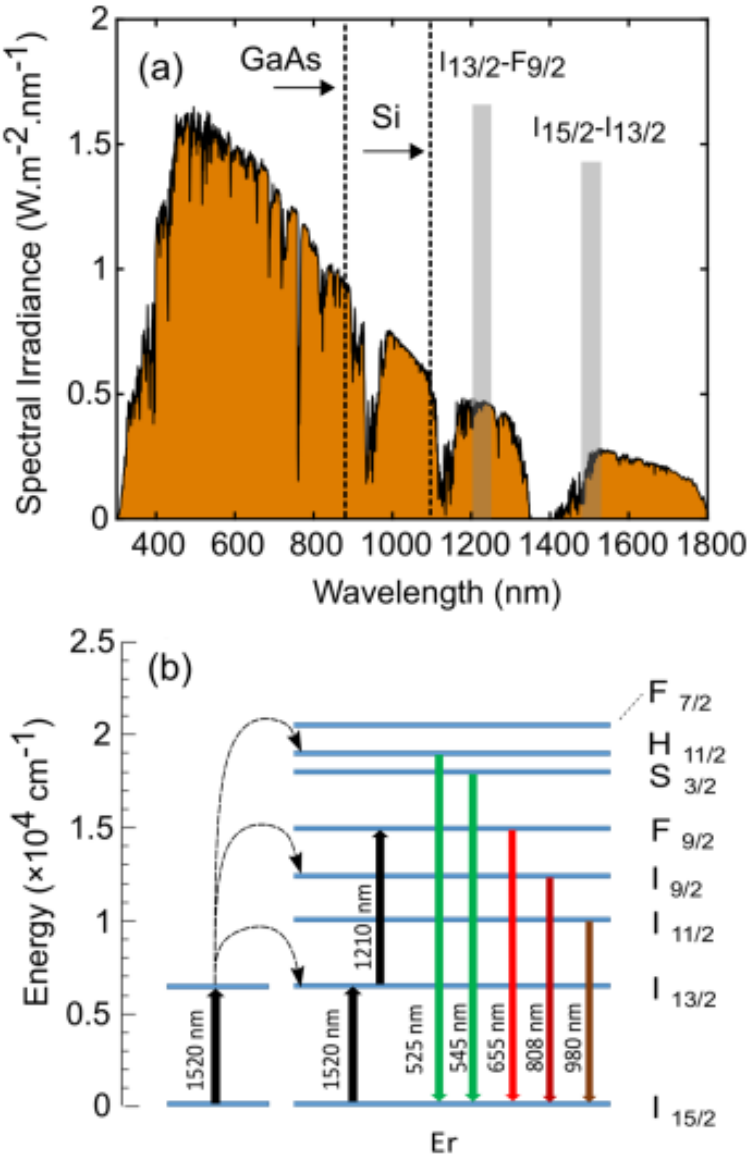

Figure A.1: (a) AM 1.5 solar spectrum with IR absorption bands of Erbium shown in grey and band-edges of Si and GaAs shown with vertical dashed lines. (b) Energy diagram for Erbium showing upconversion fluorescence for pumping at 1520 nm, and dual pumping at 1520 nm + 1210 nm [10]. Copyright 2018, American Chemical Society.

sion emission scheme of interest for dual wavelength upconversion. For Silicon solar cells, currently operating above 26% efficiency [79, 80, 81], additional upconverted photons may provide (albeit extremely modest) additional energy close to the bandedge by enhancing the 980 nm transition. This preferential enhancement will provide less heating in the bulk of the solar cell. For GaAs solar cells, currently operating close to 28.8% efficiency [82, 81], 980 nm photons are not absorbed, and so selective emission of 808 nm upconverted photons is desired. Plasmonic enhanced upconversion is one of the most promising schemes for selecting the excitation and emission wavelengths [83, 27, 84, 85, 86, 87, 88, 89, 90, 91].

In this work, we provide a proof-of-principle demonstration of dual-wavelength excitation and plasmon-enhanced selective emission from Er doped nanoparticles. We first characterize the Er doped nanoparticles in solution and then drop-coated on glass and gold. Then we drop coat different resonance gold nanorods for selectively enhanced emission.

Figure A.2 shows the upconversion emission spectrum of the Er doped nanoparticles in hexane solution with excitation at >1200 nm. The emission peaks of interest are around 980 nm and 808 nm, since these lie just below the bandedge wavelengths for Si and for GaAs.

Figure A.3 shows the emission intensity at the 808 nm and 980 nm peaks for selective excitation. The selective excitation was achieved by filtering the excitation from a supercontinuum source. The intensity of the source was 0.4 W/cm^2 and the density

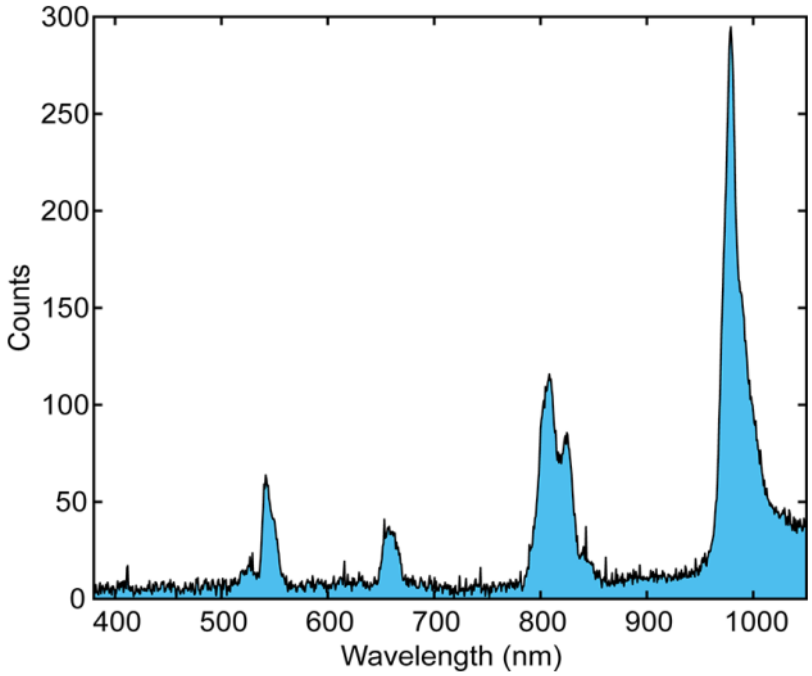

Figure A.2: Upconversion emission spectrum of Er doped nanoparticles in hexane pumped with supercontinuum source >1200 nm wavelength [10]. Copyright 2018, American Chemical Society.

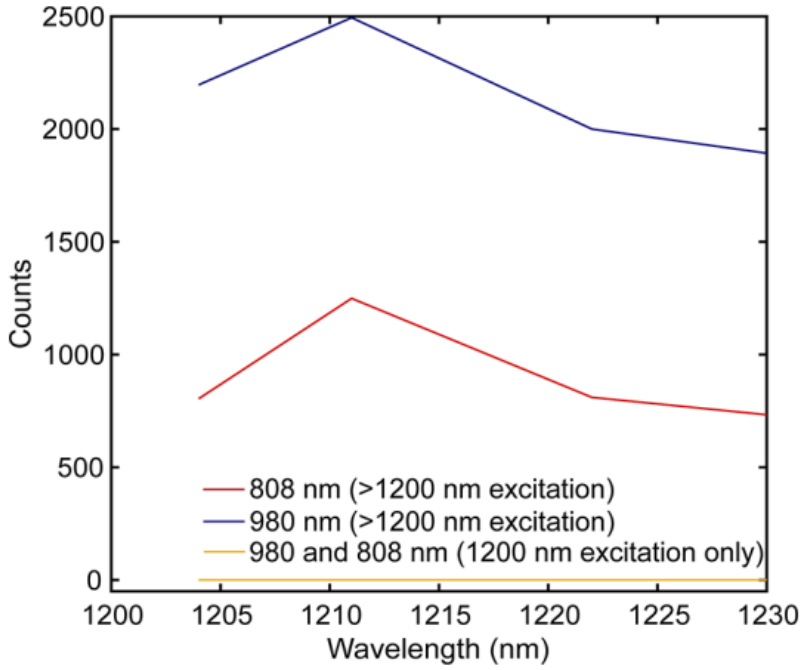

Figure A.3: Emission at 808 nm and 980 nm when tuning the ∼1200 nm excitation for the cases of simultaneous 1520 nm excitation and no 1520 nm excitation [10]. Copyright 2018, American Chemical Society.

of Er doped nanoparticles in hexane was 14 mg/ml. Upconversion is not observable without 1520 nm excitation. Figure A.3 shows upconversion emissions of 980 nm and 808 nm is increased by adding 1210 nm excitation. The >1200 nm excitation shows greater emission than the >1500 nm excitation alone. This shows that sequential absorption at 1520 nm and then 1210 nm is required to observe enhanced upconversion as shown in the scheme of Figure A.1(b). Without the 1520 nm excitation, none of the 1210 nm photons can be harvested in the upconversion scheme. (Due to the low resolution of the prism selection of excitation, an absorption bandwidth of ∼10 nm is estimated around 1210 nm).

Figure A.4 shows the power dependence for the excitation at 1520 nm and for >1200 nm (broadband). The >1500 nm excitation shows an approximately linear power dependence, whereas the >1200 nm excitation has an exponent between 2 and 3. The exponent between 2 and 3 supports that this is a multi-stage process [46]. The linear slope for the >1500 nm excitation in Figure A.4(a) suggests that the process is limited by an energy transfer step.

For one sun power density at 1210 nm and 1520 nm with 20 nm bandwidths, the accumulative power density is 0.0014 W/cm^2. With total power of 0.4 W/cm^2 for 1200-1600 nm excitation, the applied power density is 0.04 W/cm^2 for only 1200-1220 nm and 1510-1530 nm ranges. This shows our pump has approximately 28 times the sun power in that range. It is possible to increase the power via solar concentrators and have more energy harvesting of the 1210 nm and 1520 nm bands. Saturation

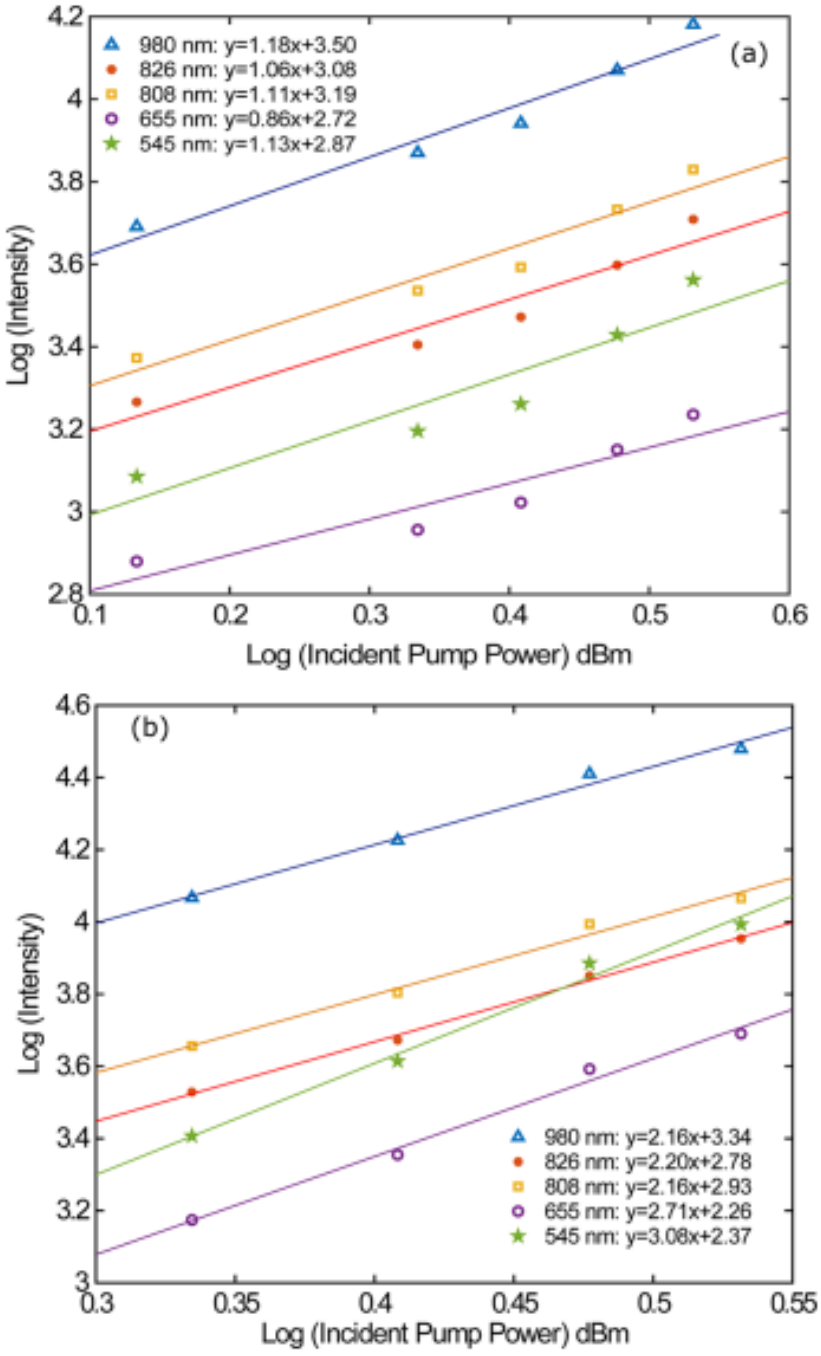

Figure A.4: Power dependence of different emission bands for excitation wavelengths (a) 1520 nm, and (b) >1200 nm. Incident laser is 1 mm diameter [10]. Copyright 2018, American Chemical Society.

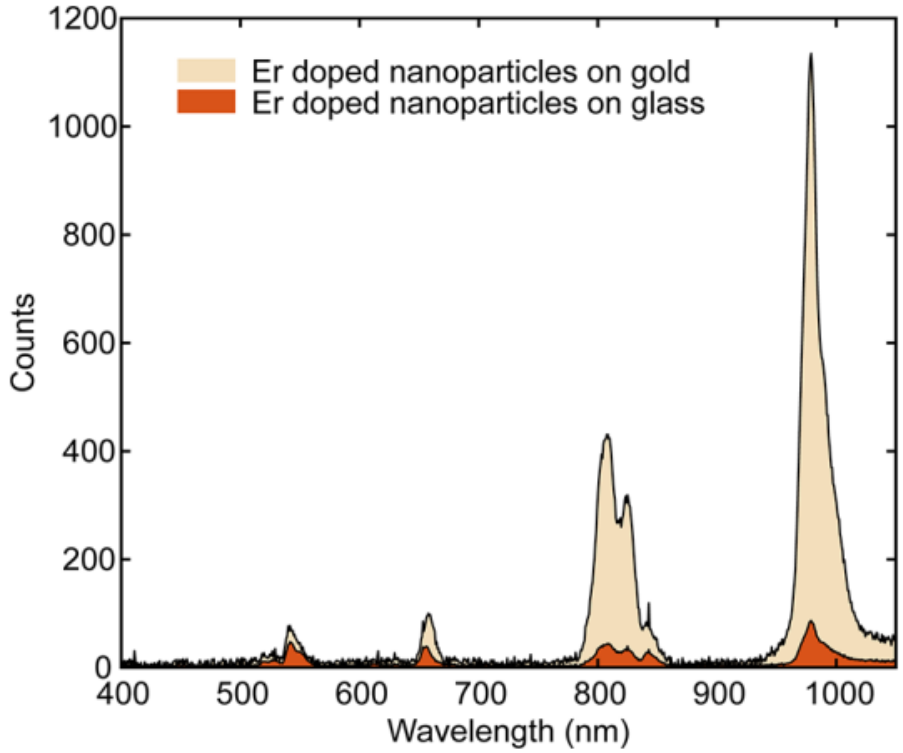

Figure A.5: Increase in upconversion emission when drop coating on gold as compared with glass [10]. Copyright 2018, American Chemical Society.

occurs when the upconversion emission changes from a second order to a first order power dependence [92]. Due to the fact that saturation for Er doped nanoparticles for 980 nm excitation happens in the range of 100-200 W/cm^2 power density [93], the applied power density in this investigation is far from saturation. Based on these findings, we believe that adding nanorods with resonances at 1210 nm and 1520 nm may provide additional near-field solar concentration and enable practical application of this scheme for enhancing solar cell performance.

Figure A.5 shows the spectra for the Er doped nanoparticles drop coated on glass and on gold for excitation >1200 nm. The gold enhances the upconverted emission by

approximately doubling the local magnetic field at the surface and reflecting photons that would have been emitted preferentially into the glass substrate [94, 95, 96, 97, 98]. The 980 nm emission increased by a factor of 13 when drop-coating on gold as compared to on glass.

Figure A.6 shows additional plasmonic enhanced upconversion when nanorods are drop-coated on top Er doped nanoparticles. Both 808 nm (E12-25-808-NPO-HEX-50, NanoPartz) and 980 nm nanorods (E12-25-980-NPO-HEX-50, NanoPartz) were used. The 980 nm nanorods selectively enhanced emission from the 980 nm band and the 808 nm Er doped nanoparticles selectively enhanced emission from the 808 nm band. (We also studied only >1500 nm excitation, and the reduction in emission is similar to found in solution of Fig. A.2, so not presented here). In Figure A.6(b), the enhancement at 980 nm is 55% with none shown at 808 nm. Detailed permutations were not attempted. We did, however, try one additional run in which the nanorod density was increased by a factor of four and the enhancement doubled for emission at 980 nm. There is a moderate enhancement at 655 nm which is interesting because the nanorods do not show a plasmonic resonance in the extinction spectrum for that wavelength. We have investigated this further by finite-difference time-domain simulation and found that there is a dark mode plasmonic resonance at that wavelength (see Supporting Information).

The nanorods have little influence for the excitation beam because the incident wavelength range is greater than 10 times the size of the nanorods (well into the

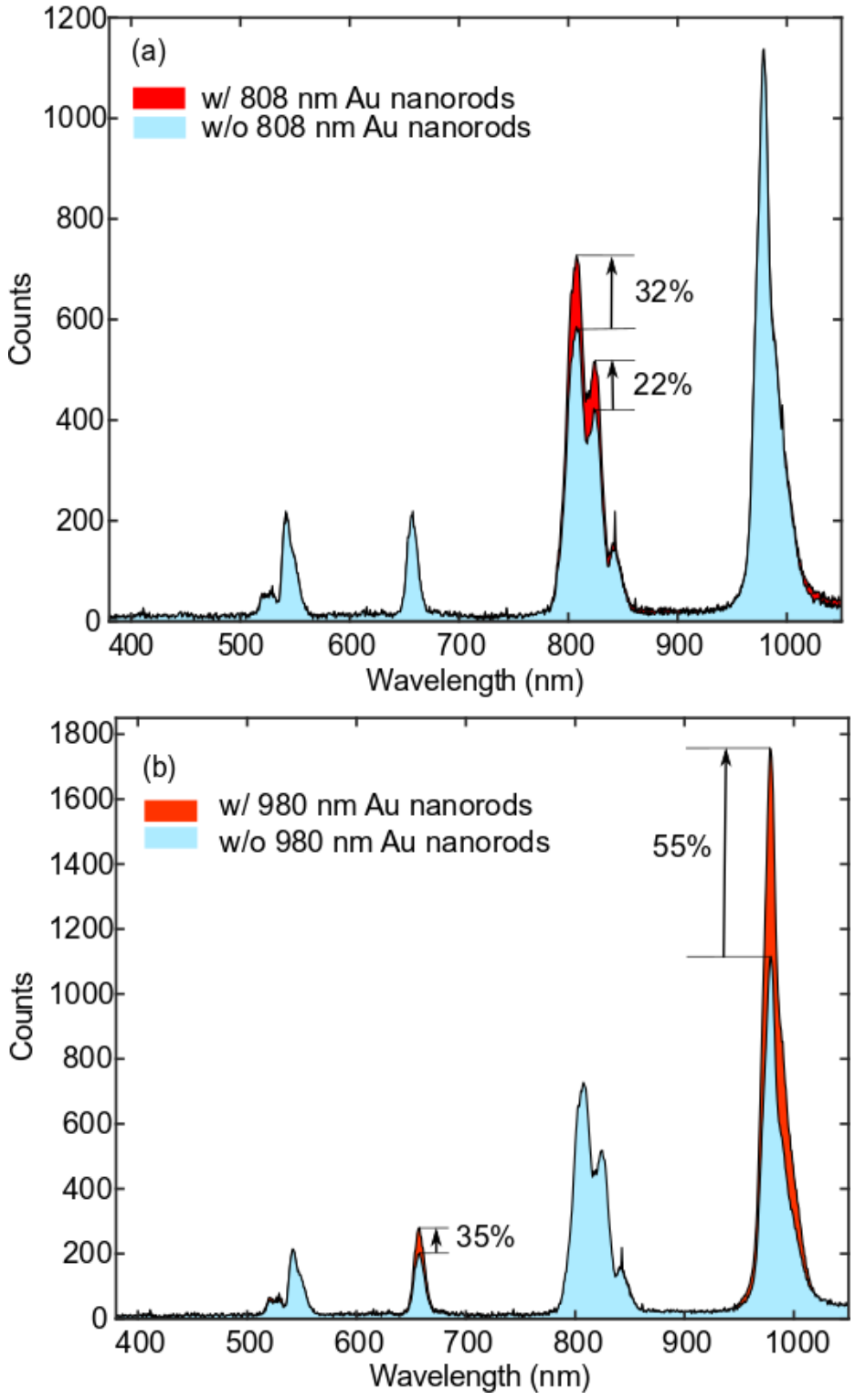

Figure A.6: (a) Enhanced upconversion at 808 nm when using 808 nm nanorods. (b) Enhanced upconversion at 980 nm when using 980 nm nanorods [10]. Copyright 2018, American Chemical Society.

Rayleigh regime) and also well away from the plasmonic resonance. Therefore, the main function of the nanorods is to selectively enhance the emission rate at the plasmonic resonance. There is also expected to be some enhancement in the outward scattering and absorption by the nanorods themselves. The relatively contributions of these different factors will require more precise control of the relative placement of the nanorods and the Er doped nanoparticles. The present scheme merely identifies that there is plasmon selective enhancement of the detected emission. We note that the ratio of Er doped nanoparticles to nanorods is ∼15000:1; therefore, we expect that most of the Er doped nanoparticles are not in the vicinity of the plasmon hotspot. Controlled placement of the Er doped nanoparticles is required to fully quantify the plasmonic enhancement [99, 100, 101, 102, 103, 104, 105].

In addition, it is possible to consider adding plasmonic resonances at 1520 nm and 1210 nm to enhance the absorption processes. We note that Figure A.4 shows we are not in the saturated regime for either of the excitation bands, and therefore greater conversion efficiency is expected by enhancing the absorption efficiency at those wavelengths as well. We also observe a small amount of blue upconversion (see Supporting Information); however, this is weak because we are not in the strong excitation regime and blue upconversion requires four photon absorption at 1520 nm.

In conclusion, we have investigated dual-band upconversion that uses two of the IR solar bands at 1210 nm and 1520 nm by sequential absorption. We demonstrated that nanorods could be used to selectively enhance the upconverted wavelengths of

980 nm and 808 nm, which is of interest to silicon and GaAs solar cell technologies. In the present scheme, we have not optimized the coupling of the plasmonic resonance to the Er doped nanoparticles, and further work is required to quantify this effect to determine whether it can provide significant benefit for solar harvesting applications. It is interesting to use this upconversion scheme because the harvested bands are outside of the region of the usual silicon solar cells, and so the upconverting material with plasmonic enhancement may be placed at the back electrode of the solar cell without degrading in-band incident photons before they interact with the absorbing region.

A.1.3 Experimental Methods

$NaYF_4$: 2% Er Chemicals

Yttrium(III) chloride hexahydrate (99.99%), erbium(III) chloride hexahydrate (99.995%), ammonium fluoride (99.99%), tech grade oleic acid (90%), tech grade 1-octadecene (90%), and hexanes were purchased from Sigma-Aldrich. Anhydrous ethanol from Commercial Alcohols, methanol from Caledon, and sodium hydroxide from Bio Basic Canada inc. were used. All chemicals were used as received.

Synthesis

A synthesis was adapted from a previously reported procedure [106]. In a 100 mL three-neck round-bottom flask, 300 mg $YCl_3{\cdot}(H_2O)_6$ and 8 mg $ErCl_3{\cdot}(H_2O)_6$ are

added to 15 mL 1-octadecene and 6 mL oleic acid. The mixture was heated to 160 °C under vacuum and kept at that temperature for 30 minutes before cooling to room temperature. Once cooled, a solution of 100 mg sodium hydroxide and 148 mg ammonium fluoride in 10 mL methanol is added dropwise while stirring. The mixture was heated to 70 °C for 60 minutes to evaporate the methanol. The mixture was put under a blanket of argon and the temperature was raised to 300 °C over 15 minutes. The temperature was kept between 295 and 305 °C for 60 minutes. The reaction mixture was then cooled, washed with 20 mL ethanol, centrifuged at 1800 g for 10 min, and washed with 20 mL ethanol again before dispersing the particles in 20 mL hexane. We have performed X-ray diffraction and transmission electron microscope for the characterization of Er doped nanoparticles, as detailed in the Supporting Information.

Measurements

For the solution-based measurements 14.4 mg/mL Er doped nanoparticles in hexane were placed in a quartz cuvette and illuminated with supercontinuum source (Fianium SC400). The maximum integrated intensity of the source was 0.4 W/cm^2. A prism and slit, neutral density filter (NE10A, Thorlabs) as well as bandpass filter (FEL 1200, Thorlabs) were used to select desired bands of excitation. The excitation spectrum was measured with a fiber-based near-IR spectrometer (Ocean Optics NIR512). The emission spectrum was measured with a fiber-based spectrometer (Ocean Optics

QE65000) with ten seconds integration. A 2.3 cm focal length lens was used for coupling to the spectrometer. For the substrate-based measurements, 8 drops of 8 μL were dropped on microslides (LAB-033, Bio Nuclear Diagnostics) and gold-on-glass (EMF CA134), allowing to dry between each drop. For the 808 nm gold nanorods in hexane (E12-25-808-NPO-HEX-50, Nanopartz), or 980 nm gold nanorods in hexane (E12-25-980-NPO-HEX-50, Nanopartz) were drop-coated after the first four drops of Er doped nanoparticles, and this was followed with 4 more drops of Er doped nanoparticles. Gentle mixing on the surface was performed after each drop. Detailed permutations were not attempted.

A.2 Supporting Information: Harvesting dual-wavelength excitation with plasmon-enhanced emission from upconverting nanoparticles [10].

Figure A.7 shows X-ray diffraction for phase analysis and confirmation of $NaYF_4$: 2% Er in nanoparticles. X-ray diffractograms with a resolution of $0.0263°2\theta$ were collected using a PANalytical Empyrean X-ray System with a Cu source (Kα radiation, λ = 1.54060 Å) operating at 45 kV and 40 mA.

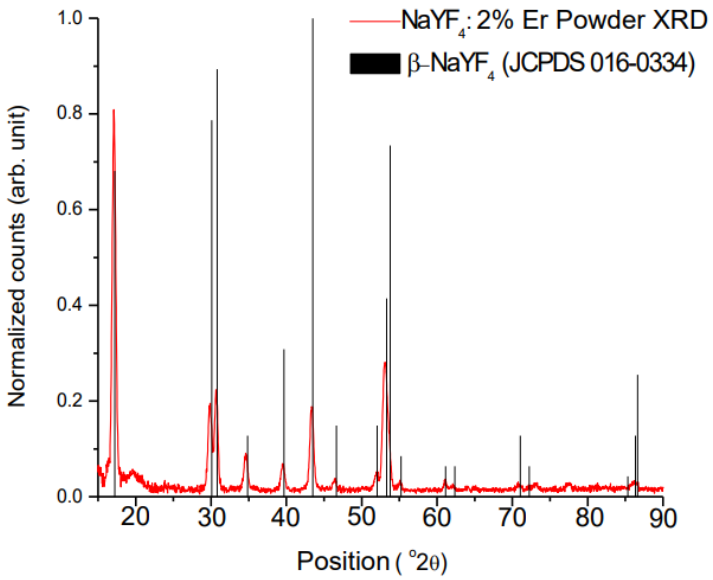

Figure A.7: Experimental x-ray diffractogram of $NaYF_4$: 2% Er doped nanoparticles and a reference pattern of hexagonal $NaYF_4$ [10]. Copyright 2018, American Chemical Society.

Figure A.8 shows transmission electron microscopy image of the spherical $NaYF_4$: 2%

Er upconverting nanoparticles under 250k× magnification. Transmission electron microscopy images were obtained using a JEOL JEM-1400 microscope operating at 80 kV. Hexane dispersions of the Er doped nanoparticles were drop-cast on a Formvar carbon-coated grid (300 mesh Cu) and air-dried before imaging.

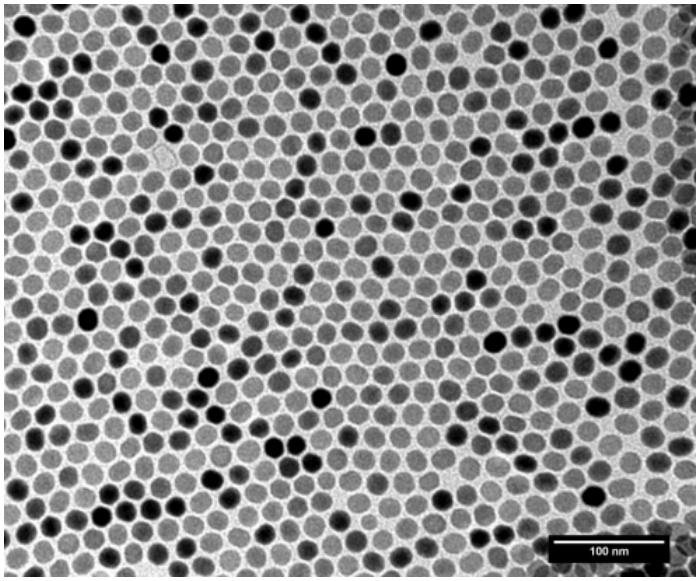

Figure A.8: Representative TEM image of $NaYF_4$: 2% Er nanoparticles magnified 250k times [10]. Copyright 2018, American Chemical Society.

Figure A.9 shows Er doped nanoparticle size distribution. Size analysis of Er doped nanoparticles from the images was performed by measuring the area of at least 800 particles.

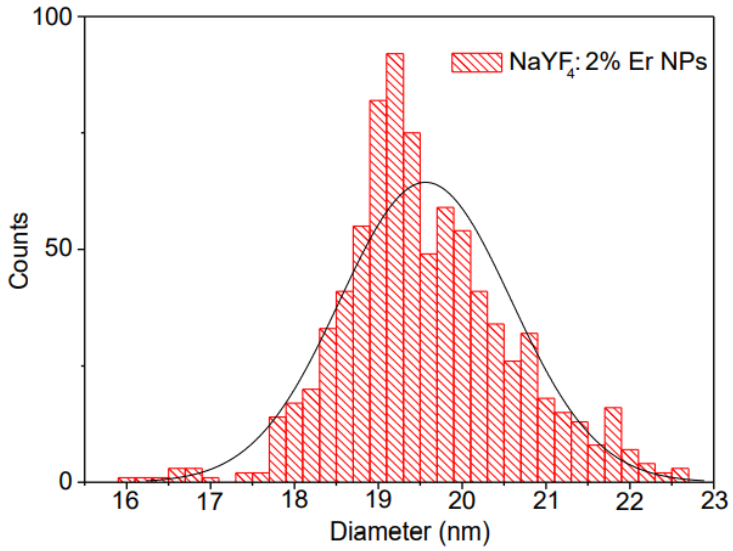

Figure A.9: Size distribution of measured $NaYF_4$: 2% Er doped nanoparticle with a mean diameter of 19.56 nm and standard deviation 1.02 nm [10]. Copyright 2018, American Chemical Society.

Figure A.10 shows the weak peak around 410 nm for Er doped Er doped nanoparticles drop coated on a gold surface. The intensity of this peak is lower than other peaks due to the requirement for four photon upconversion.

Figure A.11 shows the 3D simulation of a gold nanorod using finite-difference time-domain (FDTD) analysis, Lumerical Solutions Inc., release 2017b, version 8.18.1365. Uniform mesh type with staircase mesh refinement was chosen. The mesh size was set to 1 nm in x, y, and z directions. The FDTD simulation region had a length of 0.1 μm in the x direction, 0.2 μm in the y direction, and 0.1 μm in the z direction with PML boundary conditions. The field monitor geometry was 2D-Z normal with dimensions 0.1 μm $\times$ 0.15 μm. We used an electric dipole source with wavelength

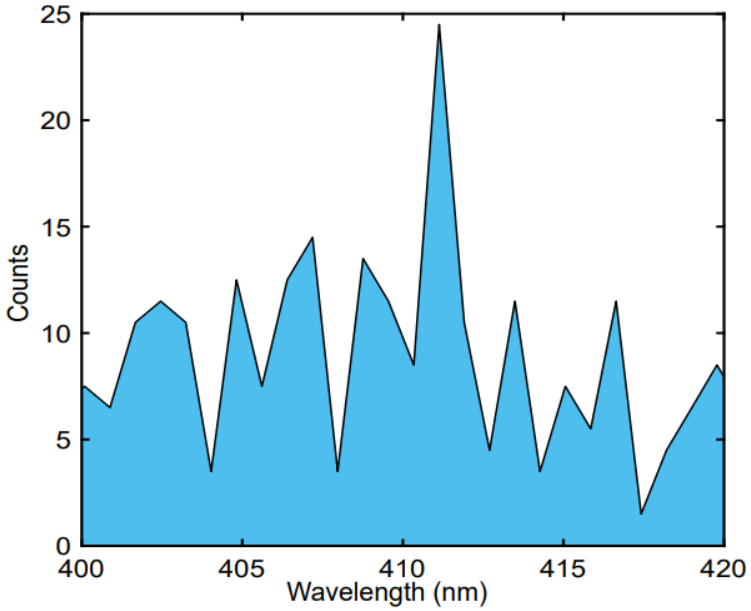

Figure A.10: Weak upconversion emission at 411 nm [10]. Copyright 2018, American Chemical Society.

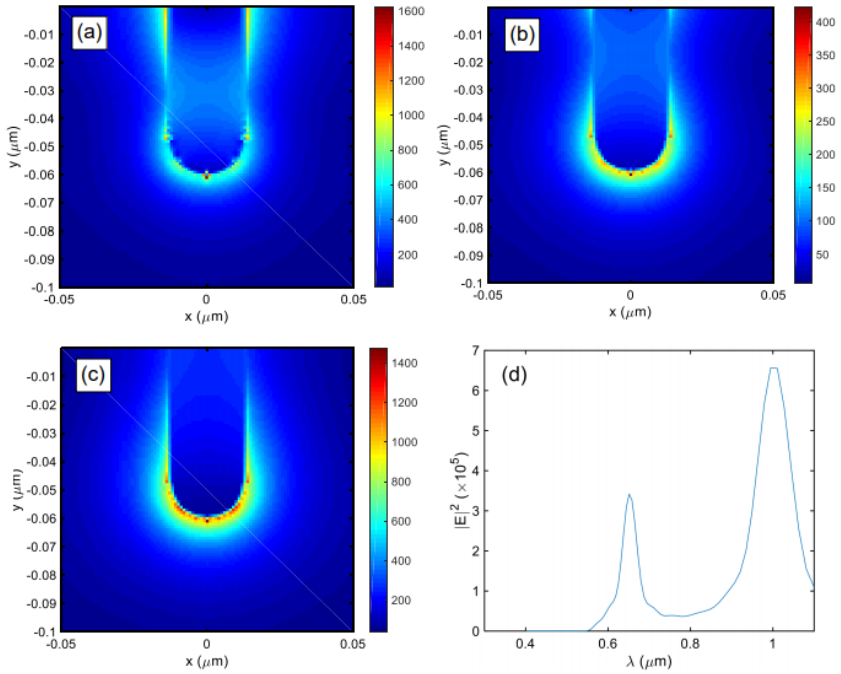

Figure A.11: Finite difference time domain modeling for electrical field intensity around gold nanorods at wavelengths of (a): 658 nm, (b): 812 nm, (c): 994 nm. (d) Field enhancement close to gold nanorods in the 400-1100 nm spectral range [10]. Copyright 2018, American Chemical Society.

range from 400 to 1100 nm, located 70 nm away from the tip of the gold nanorod. The monitor collected the data for 100 wavelength points at the other side of the nanorod. The time stability factor was 0.99 and auto shutoff condition was 1×10^{-5}. The field is enhanced at 658 nm and 994 nm, and significantly less so at 812 nm. The peak of the dark mode resonance of 980 nm gold nanorods occurs at 658 nm and it has a full width at half maximum of 45 nm. Therefore, the 655 nm emission band occurs inside this resonance region.

Appendix B

Colloidal lithography double-nanohole optical trapping of nanoparticles and proteins [8].

Originally published:

A. L. Ravindranath,[1] M. S. Shariatdoust[1], S. Mathew, R. Gordon, colloidal lithography double nanohole optical trapping of nanoparticles and proteins, Optics express, 27(11), 16184-16194 (2019).

[1]equal contribution

B.1 Colloidal lithography double nanohole optical trapping of nanoparticles and proteins

B.1.1 abstract

Double nanoholes fabricated by colloidal lithography were used for trapping single colloidal particles and single proteins. A gap separation of 60 nm between the cusps of the double nanohole was achieved in a gold film of 70 nm thickness sputter coated on glass. The cusp separation was reduced steadily down to 10 nm by plasma etching the colloidal particles prior to sputter coating. Scanning electron microscopy was used to locate a particular double nanohole and it was registered for later microscopy experiments. 30 nm polystyrene particles, the rubisco protein and bovine serum albumin were trapped using a laser focused through the aperture. Compared to other methods that require top-down nanofabrication, this approach is inexpensive and produces high-quality samples.

B.1.2 Introduction

Optical tweezers have been used to trap and manipulate small objects such as nanoparticles [32] and viruses [33]. Optical trapping of particles smaller than a tenth of the wavelength requires large intensities using conventional single beam traps. The limit of Rayleigh scattering makes it challenging to trap and characterize such small parti-

cles. To trap particles smaller than 100 nm, apertures have been investigated [107, 35]. While plasmonic antennas are able to trap 10 nm metal nanoparticles [108] they did not demonstrate trapping of dielectric nanoparticles smaller than 100 nm [109, 110, 111, 112]. Double nanohole [4, 113], bowtie [114, 115] and rectangular [116] apertures allow for trapping particles as small as a few nanometeres (including single proteins [2]). Nanoapertures at the end of an optical fiber have been used for moving particles around [115]. Additionally, optical trapping using nanoapertures have made it possible to study protein-DNA interaction [5] and understand vibrational modes of nanoparticles [6, 49] as well as estimating their molecular weight and sizes [117, 50].

A critical component of aperture-based optical trapping is the fabrication of nanoapertures in thin metallic films. Most of the existing works use focused-ion beam lithography or electron beam lithography [118, 119]. Template stripping offers an alternative method for creating apertures but this technique depends on focused ion beam milling or electron beam lithography for fabricating the initial template [120, 121]. Here we present a colloidal based method for fabricating double nanoholes with gaps of 60 nm in a 70 nm gold film and decreasing cusp size to 10 nm as well as study their use in trapping of nanoparticles and proteins. Many other works have used colloidal lithography to fabricate plasmonic sturctures and nanoparticles [122, 123, 124, 125, 126, 127, 128, 129, 130]. Single apertures have been used for trapping 200 nm polystyrene particles with this approach [55]. Also, double nanoholes have been fabricated by this approach and their nonlinear-optical properties investi-

gated [131]. That work produced gaps in excess of 180 nm, so they were likely not useful for trapping smaller particles.

B.1.3 Fabrication

Figure B.1 shows the process flow for fabricating the double nanoholes by colloidal lithography. Microscope slides (12-550-A3, Fisherband) were plasma cleaned for 15 minutes at high power (Harrick, PDC-002) and sonicated (3510, Branson) for 8 minutes in an ethanol bath. 30 μL of 200 nm 0.01% w/v polystyrene in ethanol was prepared and drop-coated uniformly on each microscopic slide. The polystyrene spheres were allowed to attach to the slides while the solution dries out through evaporation. Polystyrene solutions with lower concentrations result in predominantly single apertures (see Appendix for additional details).

The prepared slides were sputtered (MANTIS Sputtering System) with 5 nm of titanium as an adhesive layer followed by 70 nm of gold. The thickness of the sputtered layers were chosen in a way to ensure polystyrene beads could be removed later (see Appendix for apertures fabricated in thicker films that led to tearing of the gold layer). The Au-Ti coated samples were sonicated for 5 minutes in an ethanol bath to remove polystyrene beads.

Figure B.2 shows the effect of plasma etching on the aperture diameter and cusp separation of double nanoholes fabricated by colloidal lithography. Plasma etching reduces the cusp separation reliably. Error bars on each data point shows multiple

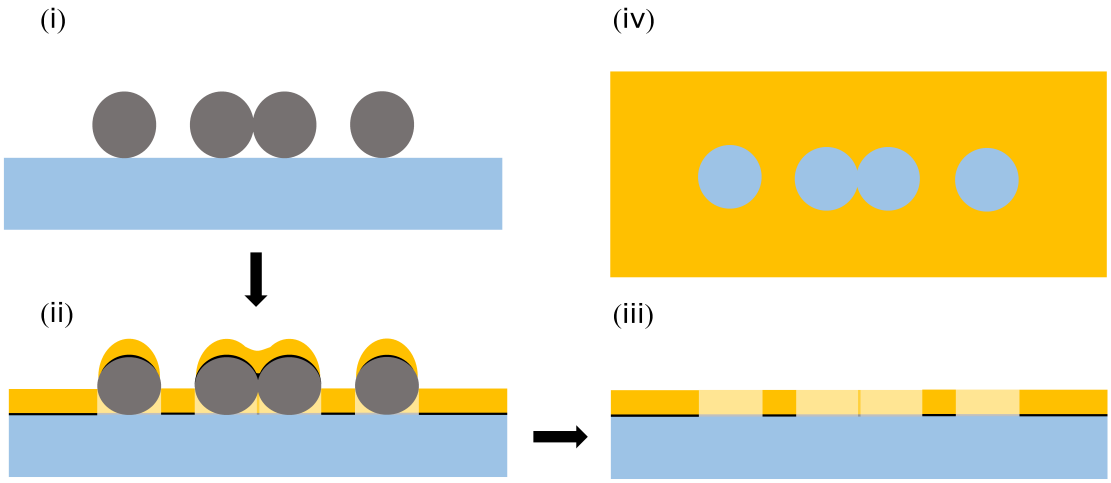

Figure B.1: Process flow diagram of the colloidal lithography fabrication procedure. i) 200 nm diameter polystyrene spheres were drop coated on a microscope slide. ii) 70 nm thick gold with a 5 nm titanium adhesion layer was sputter coated over the slide with spheres. iii) Sonication was used to remove spheres. iv) Top view shows single and double holes [8]. Copyright 2019, Optical Society of America.

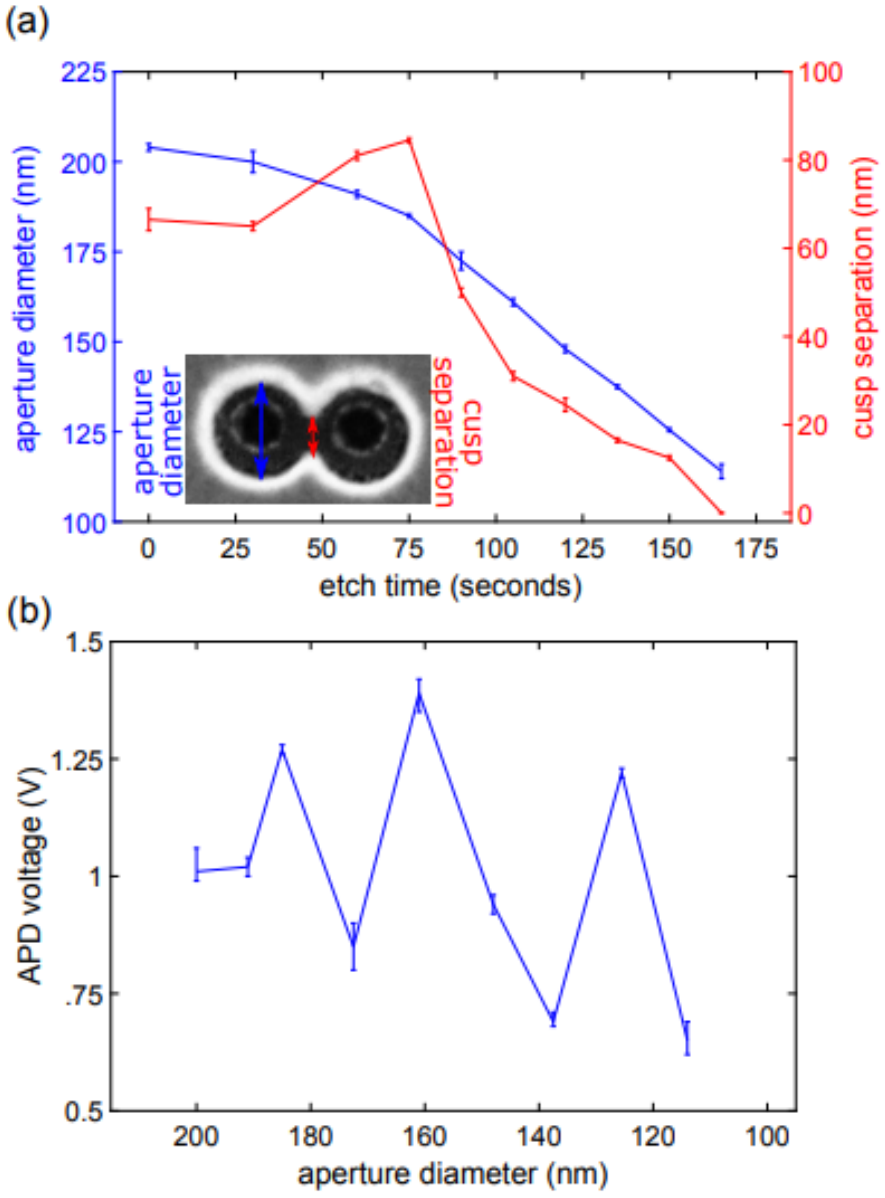

Figure B.2: (a) Effect of plasma etching on the dimensions of the double nanohole aperture diameter and cusp separation indicated in inset (b) Transmission (APD voltage) through double nanohole apertures with dimensions varying according to respective etch times [8]. Copyright 2019, Optical Society of America.

apertures measured for each sample. At the start of the plasma etching process, surface reflow between polystyrene beads increases the cusp separation. Continuing the plasma etching process eventually decreases cusp separation to the point at which they are touching. Figure B.2 shows the variation in transmission through different double nanoholes when illuminated with a 980 nm laser. This is the maximum transmission found by rotating the polarization. It is clear that the transmission shows non-monotonic behavior which may be associated with tuning the plasmonic resonances of the aperture as the cusp separation is reduced and the shape is changed.

B.1.4 Registration

Figure B.3 shows collocation of a double nanohole aperture comparing its location on a SEM image with the image seen on the trapping setup. Since larger apertures typically appear brighter because of longer wavelength cut-offs, the brighter points observed in the trapping setup image can be mapped to corresponding apertures in the SEM image. The location of the double nanohole near the tip of a fiduciary line was located in the SEM. A unique constellation was identified using the surrounding apertures. Their respective sizes translate to varying brightness levels when observed on the trapping setup. This helps with the constellation mapping and collocation of the double nanohole of interest.

Figure B.3 (c) shows a double nanohole fabricated with 200 nm polystyrene beads. The cusp size is approximately 60 nm in absence of plasma etching. Figure B.3

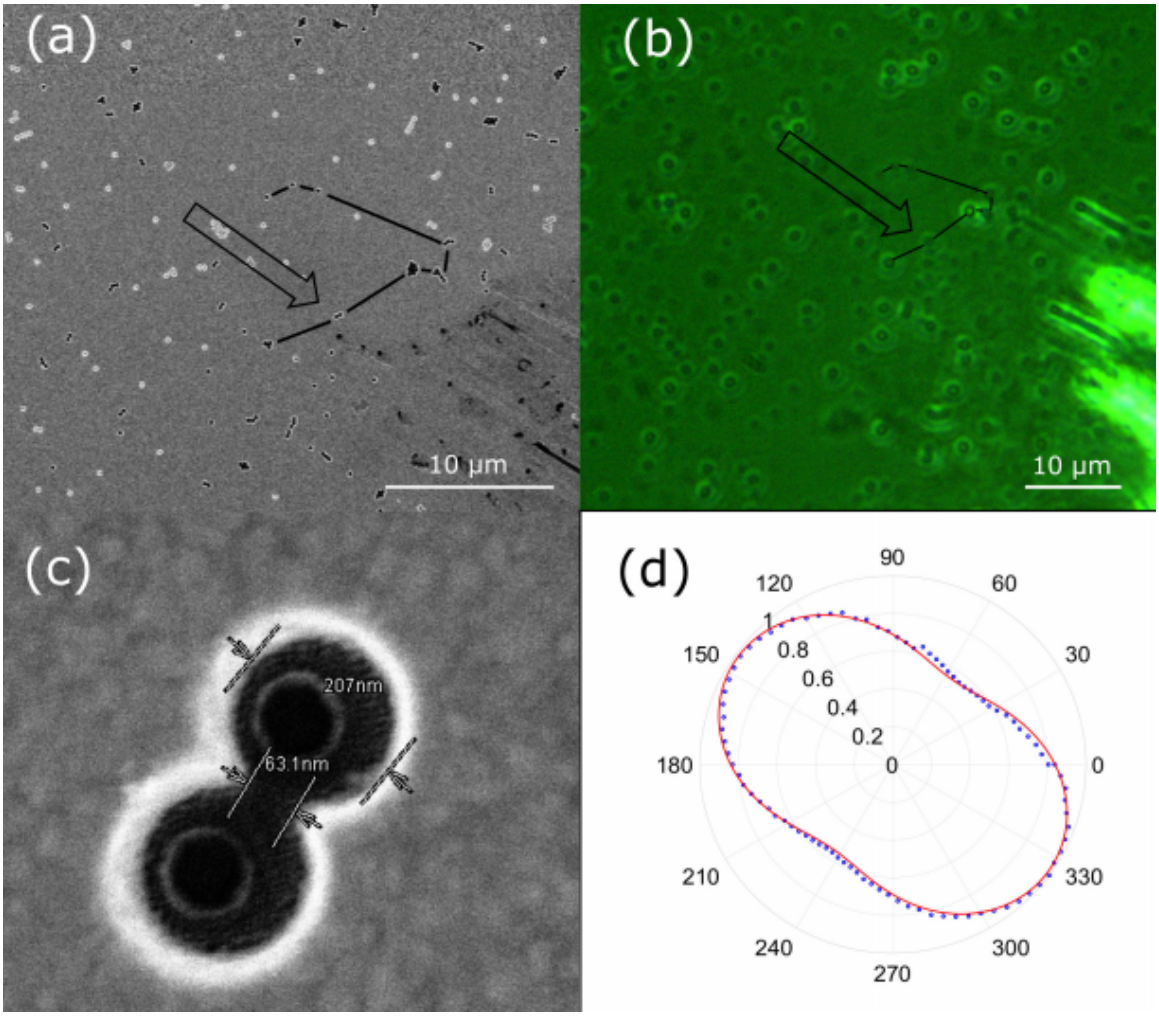

Figure B.3: Colloidal lithography double nanohole aperture collocation using images from: (a) SEM and (b) trapping setup. (c) Close up of a double nanohole with 60 nm gap size, and (d) transmission polarization dependence of a 60 nm double nanohole [8]. Copyright 2019, Optical Society of America.

(d) shows the polar plot of incident 980 nm laser transmission through the double nanohole recorded as the normalized voltage which is a function of polarization angle. The maximum transmission was obtained when the polarization of the electric field was aligned with the axis between the cusps (144°). The polarization was tuned from 0-2π using the half-wave plate. A Malus' law fit is shown to the polarization [132], giving a degree of polatization of 3.5.

B.1.5 Experimental

Figure B.4 shows a modified optical trapping setup from from Thorlabs' (OTKB). The setup consists of an inverted microscope arrangement with high numerical aperture confocal objectives. The laser used for trapping was a fiber-coupled (APC/FC) 980 nm (14-pin) butterfly package mounted on a Thorlabs LM14S2. Thorlabs LDC 210 C was used as the laser controller with a TED 200 C as the temperature controller. A PAF-X-7-B fiber port collimator was used for collimating the beam. A linear polarizer (LPNIR100) and a half-wave plate (WPH05M-980) were used to tune the polarization of the laser beam, oriented along the cusps of the double nanohole aperture for obtaining the maximum field localization favorable for trapping. A Galilean beam expander was used to expand the beam prior to entering the first objective. The power incident on the sample could be controlled using optical density filters (NE03A). The dichroic mirror (DMSP805T) allowed light from the white light source to be transmitted onto the CCD camera for imaging the sample and the apertures

while reflecting the incident laser on to the objective lens.

The expanded beam was focused onto the sample through a 100× magnifying oil immersion microscope objective with 1.25 numerical aperture. The high numerical aperture reduced the beam width of the incident laser on the sample to around 1.1 μm. The transmission through the aperture was then collected through a 10× magnifying objective with a 0.25 numerical aperture. The sample for the trapping experiment was prepared using a suitable glass cover slide with a thickness of about 150 μm (Ted Pella, Inc.), an imaging spacer (Secure Seal imaging spacer, Grace Bio-labs) was attached on the slide to create a micro-well (thickness of 120 μm and a 9 mm diameter) for the analyte. A micro-pipette was used for transferring 10μL of the analyte into the micro-well. The gold substrate with the apertures was used to seal the analyte in the micro-well.The sample was placed in between the objectives with the side of the cover slide in contact with the bottom objective using an immersion oil with refractive index of 1.51. The 3-axis piezoelectric stage allowed for a 20 nm position precision while navigating for the apertures on the sample.

A silicon-based avalanche photodiode (APD) (Thorlabs, APD120A) measured the transmission through the aperture. To limit the power incident on the APD, optical density filters were used. The voltage signal from the APD was acquired by a USB-4771A data acquisition module. The data from the APD was acquired for post processing and analysis. A single-ended 2.5V (APD limitation) mode was configured prior to acquisition. The sampling frequency was set to 100 kHz to ensure transient

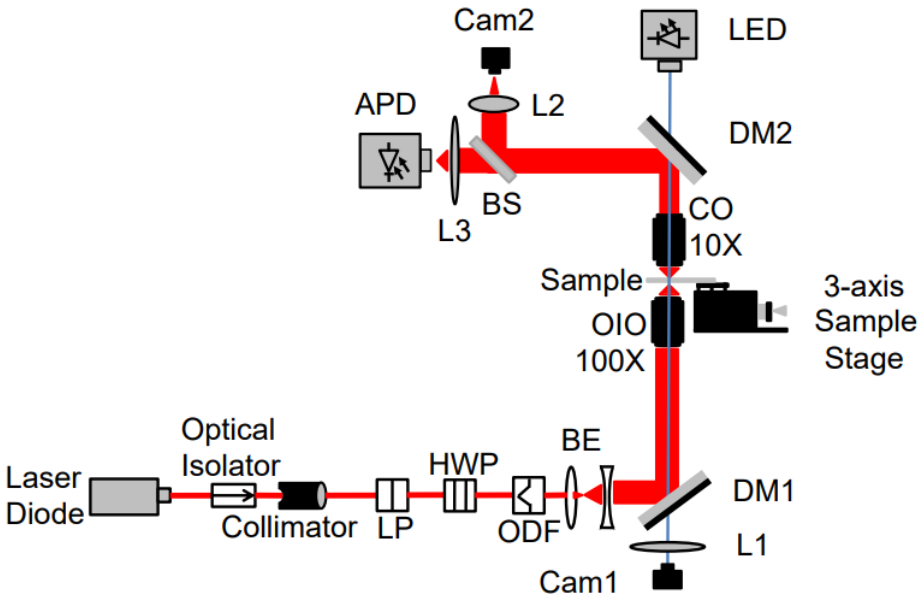

Figure B.4: Optical trapping setup schematic showing the various components: linear polarizer (LP), half-wave plate (HWP), optical density filter (ODF), beam expanding (BE) lenses, short-pass dichroic mirror (DM1), focusing Lens (L1), oil immersion objective (OIO), collection objective (CO), short-pass dichroic mirror (DM2), beam splitter (BS), focusing Lens (L2 and L3) and avalanche photodiode (APD) [8]. Copyright 2019, Optical Society of America.

data capture during a trapping event. The data was exported to MATLAB and filtered with a 101-point moving average filter (allowing RMS-noise reduction by a factor of 10) to depict accurate data for characterizing the event-the particle and the aperture. The experiment commenced once the sample was loaded onto the 3-axis piezo electric stage in between the microscope objectives. The white light source was switched on to view the location of the nano-aperture by first identifying the fiduciary marker. The marker was located and then brought into focus by adjusting the the z-height of the stage. Following this, the laser was switched on. Finally, the piezo controls were used to align the beam prior to initiating the measurement.

B.1.6 Trapping

Figure B.5 shows trapping events for 30 nm polystyrene, rubisco and bovine serum albumin (BSA). Figure B.5 (a) marker A indicates the signal recorded by the APD when the white light source for imaging the aperture was switched on. Marker B shows the signal level when the trapping laser was unblocked and illuminates the aperture. The APD signal recorded when the laser was unblocked indicates the untrapped state where there was no particle trapped in the aperture. The voltage jump at marker C was the instance when a polystyrene nanosphere was trapped. The inset shows a magnified view of the trapping event. To untrap the particle in the trapped state, the laser was blocked leaving the white light source still switched on. Subsequently the white light source was switched off and then switched on again followed by unblocking

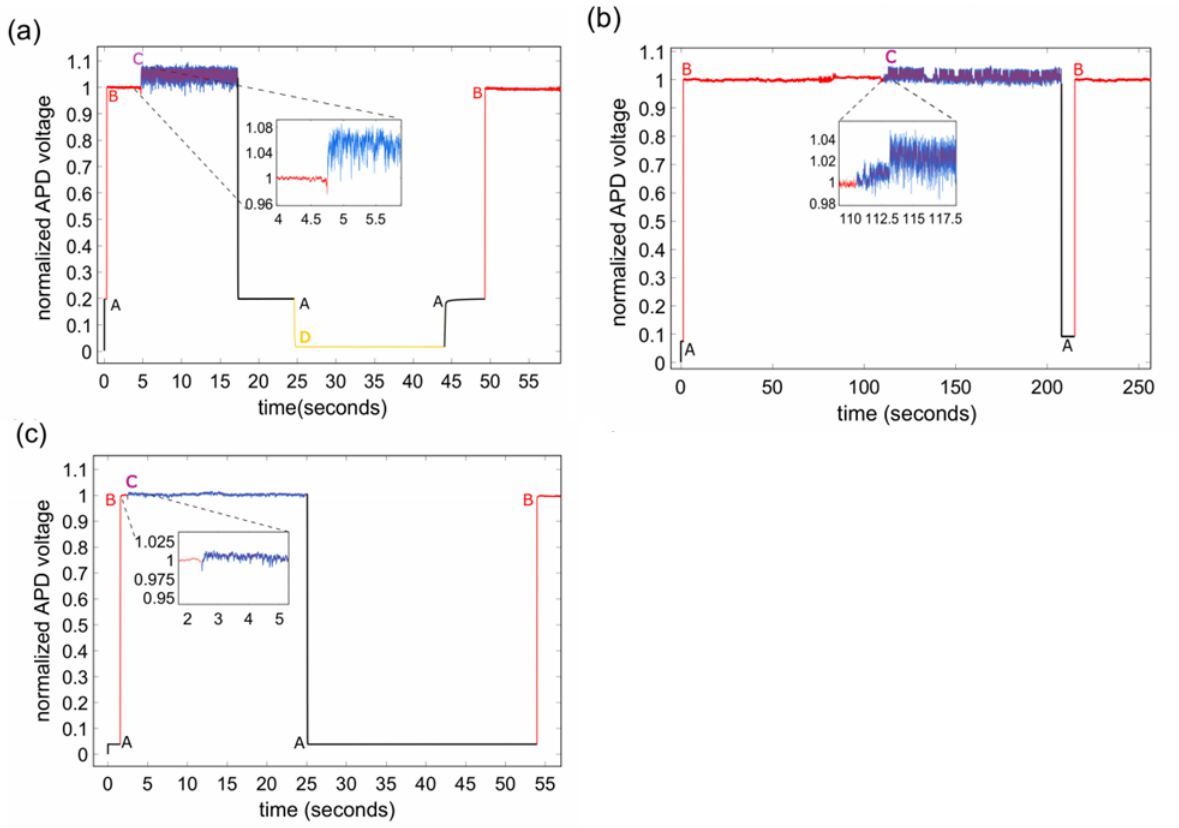

Figure B.5: Trapping of (a) 30 nm polystyrene nanosphere (b) rubisco and (c) BSA. The cusp spearation was 60 nm for (a) and (b) and 10 nm for (c) [8]. Copyright 2019, Optical Society of America.

the laser. It was necessary to block the laser to release the particle since the self-induced back action [133] comes into effect when the particle tries to move away from the trap. The change in optical transmission experienced necessitates a momentum conservation per Newton's third law ensuring that the particle is forced back into the optical trap.

In Figure B.5 (b) and (c), the white light source was switched on at A followed by unblocking the laser at B. The trapping of the respective particle is indicated by marker C, magnified in the inset. The laser was then blocked to release the trapped particle shown by the untrapped state B. This process of trapping and untrapping a particle upon unblocking and blocking the laser was seen repeatedly and reliably throughout the experiment.

B.1.7 Discussion

Here, we have effectively demonstrated a low-cost and facile method for fabricating double nanoholes in metal films. We employed plasma etching to tune the cusps separation finely from 70 nm to zero. One limitation of this approach is that the film thickness should be smaller than the radius of the colloidal particles used to allow for lift-off.

In future works, others may consider tuning the particle size used in lithography for achieving larger or smaller holes. This may lead to optimization depending on the wavelength of operation. One may also consider trapping particles with trimers or

larger assemblies. An interesting further direction of study is to combine the present approach with nanopores for complementary analysis. Nanopores have recently been integrated with apertures to analyze proteins and DNA [134, 135] as well as studying their properties by ionic flow analysis [136]. More generally, nanopores have been used in investigating single proteins [137, 138, 139], DNA [140, 141, 142, 143, 144, 145, 146] and protein-DNA interactions [147, 148] in flow-through translocation [149]. To obtain the nanopore between the cusps, one may be able to use light-assisted self-aligned breakdown, as has been done in the past for bowtie antennas[150].

B.1.8 Conclusion

Using colloidal lithography, double nanohole apertures were fabricated and used for trapping nanoparticles and proteins. The cusp separation was tuned by plasma etching the colloids prior to evaporating, and this allowed for the trapping of smaller proteins. This provides a low-cost and facile method for double nanohole fabrication that will allow others to adopt the technique. While the double nanoholes in this work are randomly located, it may be possible to use template directed assembly to place them more deterministically at a specific location by including an additional lithography (imprint or optical, for example) step [151]. Future optimization based on aperture size, or other assembly shapes, may be attempted. Also, this approach is promising for combination with nanopores by the self-aligned breakdown approach.

B.2 Supporting Information: Colloidal lithography double nanohole optical trapping of nanoparticles and proteins

Figure B.6 shows predominantly single hole nano-apertures obtained when using low concentration polystyrene in ethanol solution (approximately 0.001% w/v) in the fabrication process.

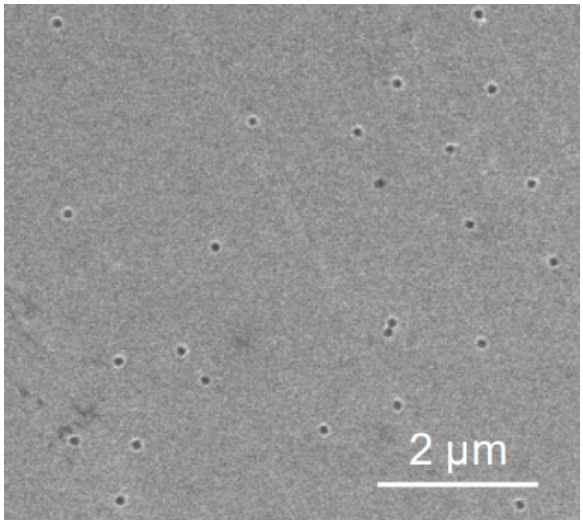

Figure B.6: Predominantly single apertures obtained for low concentration polystyrene solution in fabrication [8]. Copyright 2019, Optical Society of America.

Figure B.7 shows asymmetric apertures created after sonication when the sputter coated gold layer was greater than the radius of a polystyrene sphere. After sonication, the nanospheres seem to rip through the surface leaving behind undesired apertures.

We attempted different concentrations for the fabrication and chose the 0.01%

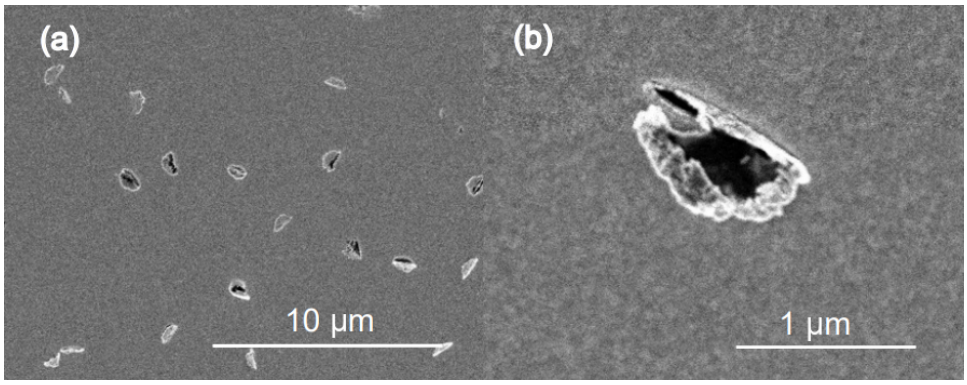

Figure B.7: (a) rips on gold surface showing multiple asymmetric apertures (b) single asymmetric aperture [8]. Copyright 2019, Optical Society of America.

w/v concentration that produced a ratio of double nanoholes to single nanoholes of $> 55\%$ (from PS of 200 nm = 76%, 300 nm = 56%, 500 nm = 140%), considering 9 samples with different particle sizes. Figure B.8 shows SEMs produced from samples with different concentrations.

Figure B.9 shows the SEM images for the wide range of apertures fabricated using the technique detailed in the paper.

Figure B.10 shows variation in the cusp separation and aperture diameter for lithography with 300 nm and 500 nm spheres, showing the ability to tune both cusp size and aperture diameter with this technique. We also trapped BSA with these different sized apertures. Figure B.10 also shows the non-monotonic transmission characteristics from apertures fabricated with 300 nm and 500 nm polystyrene spheres respectively. This behaviour is systematic regardless of aperture size and is reliably reproducible.

We performed preliminary finite difference time domain simulations to analyze

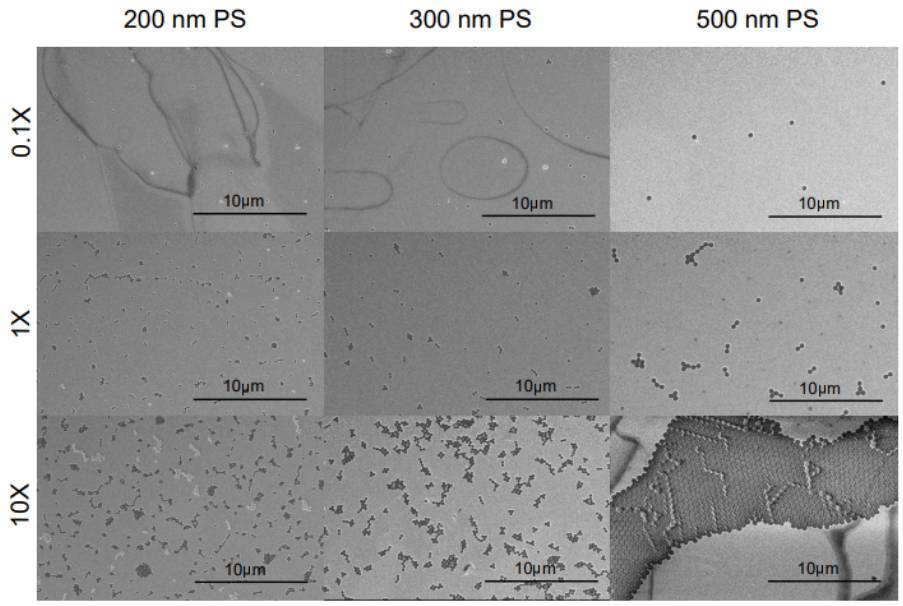

Figure B.8: SEM images for samples fabricated using various concentrations of different Polystyrene bead sizes [8]. Copyright 2019, Optical Society of America.

the transmission through the apertures (not shown). The simulated transmission gave qualitative agreement with the observe transmission for certain features. For example, the local maxima in the transmission for apertures fabricated using the 200 nm polystyrene spheres occurred for etched diameters of 185 nm, 148 nm and 114 nm, whereas the maxima in the experiment are at etched diameters of 185 nm, 161 nm and 125 nm. Similar agreement was observed when repeating the experiment and simulations for 300 nm and 500 nm polystyrene spheres. Detailed presentation of the numerical analysis and transmission spectra are planned for a future study.

The diffraction limit of our setup was approximately 1 micron and the apertures are typically well separated by a larger distance than this, so there was limited cross

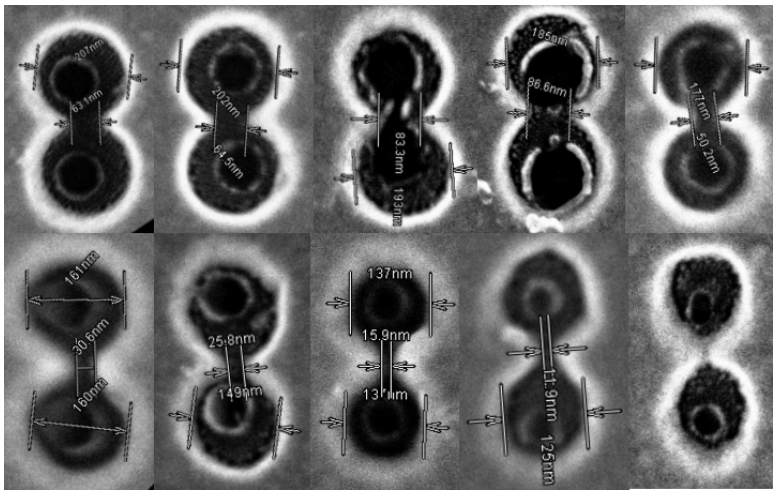

Figure B.9: SEM images of all double nanoholes fabricated using colloidal lithography and plasma etching [8]. Copyright 2019, Optical Society of America.

talk. In addition, the double nanoholes have much larger separation than the single apertures, and these let through considerably more light. The double nanoholes are typically around 10 microns apart and so we can rule out any considerable crosstalk, even through surface plasmon waves. We observed only small variation in transmission voltage (see error bars on Figure B.2 b), which also suggests that the cross talk was small. We found one particular case where there were two double nanoholes close to one another (1 micron separation) and there was crosstalk giving transmission that was 1.2 times larger than the typical isolated double nanohole in the sample.

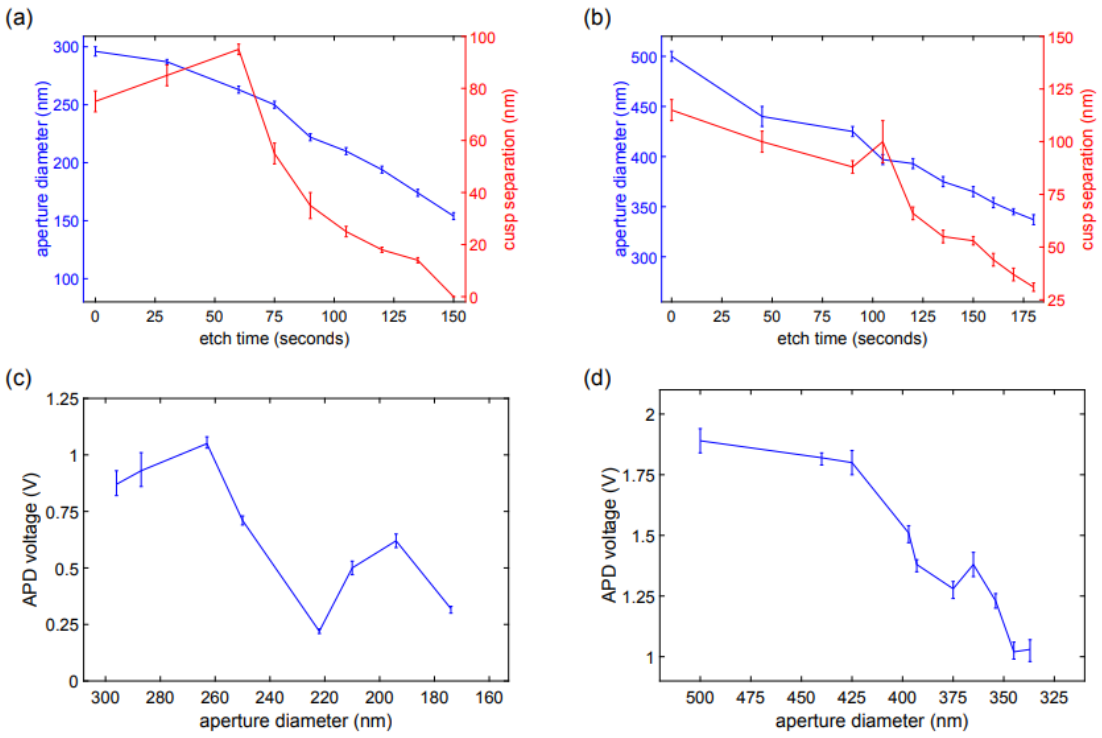

Figure B.10: (a),(b) Effect of plasma etching on the dimensions of the double nanohole aperture diameter and cusp separation for apertures fabricated using 300 nm and 500 nm polystyrene spheres. (c),(d) Transmission (APD voltage) through double nanohole apertures with dimensions varying according to respective etch times for apertures fabricated using 300 nm and 500 nm polystyrene spheres [8]. Copyright 2019, Optical Society of America.

Appendix C

Single Nanoflake Hexagonal Boron Nitride Harmonic Generation with Ultralow Pump Power [11]

Gh. Hajisalem, M. S. Shariatdoust, R. F. Ali, B. D. Gates, P. E. Barclay, R. Gordon, Single nanoflake hexagonal boron nitride harmonic generation with ultralow pump power, ACS Photonics, 2021.

C.1 Single Nanoflake Hexagonal Boron Nitride Harmonic Generation with Ultralow Pump Power

C.1.1 abstract

The strong nonlinear optical response of two dimensional materials has applications in bioimaging and integrated optical information processing; however, past experiments were on diffraction limited samples or required intense pulsed lasers, which is a detriment to potential applications due to cost, power and complexity. Here we show that second harmonic generation can be achieved from single subwavelength two dimensional material nanoflakes smaller than the diffraction limit using a plasmonic optical tweezer with a low-power (down to 3 mW) laser diode operating in continuous-wave mode. A double nanohole plasmonic tweezer enhances the local field and the local density of optical states to allow for trapping and significant nonlinear generation at the nanoscale. Also, the fact that it is a two dimensional material means that it can be positioned closer to the highest field regions, realizing two orders of magnitude higher power second harmonic generation than other nonlinear materials like lithium niobate. The ability to have simple high efficiency nonlinear generation at the nanoscale will benefit future nonlinear optics applications of these emerging materials.

C.1.2 Paper content

Nonlinear optics provides harmonic generation, frequency comb generation and all-optical switching [152, 153, 154] and has applications in information processing [155, 156] and bioimaging [157, 158, 159]. For scalable and integrated solutions, nonlinear functionality with low-power sources is desirable. Nanomaterials play a key role in enabling dense integration and high resolution imaging.

High quality factor optical resonators with micron scale dimensions address the need for nonlinear optical sources with low pump power, for example, in frequency comb generation using a battery operated laser outputting around 10 mW of power [152]. A significant challenge remains in scaling such processes down to the nanometer scale for denser integration and high resolution imaging. High quality factor cavities or waveguide based wavelength conversion devices leveraging phase matching are not possible at the nanometer scale, and can be challenging even at the micrometer scale.

Most investigations of the second order nonlinear response in thin films [160, 161, 162] and two dimensional (2D) materials [52, 53, 54, 163, 164, 165, 166] have relied on ultrafast (femtosecond) lasers to achieve a measurable signal. Ultrafast lasers compress 10 mW of continuous-wave (CW) power into short 100 fs pulses arriving every 10 ns – this increases the peak power by 100,000 times to 1 kW. As second harmonic generation (SHG) scales as the power squared, this gives 10^{10} times higher SHG during the pulse window. In addition, previous work focused on

micron scale flakes with correspondingly large generation area. While most of these works relied on using ultrafast lasers, a recent work has shown nonlinear optical response from mono- and multilayers 2D materials by using CW pump with low intensity [167]; however, that work still used a diffraction limited spot. It appears that working above the diffraction limit or using femtosecond lasers was typical for efficient nonlinear generation, and achieving similar response from nanoscale materials such as nanoflakes is a challenge.

Here we show significant SHG response from individual subwavelength flakes of hexagonal boron nitride (hBN), smaller than the diffraction limit, trapped in a double nanohole (DNH) plasmonic tweezer using a low-power (<10 mW) CW laser diode. This is similar the power intensity used in previous battery-operated demonstrations of frequency comb generation from high-quality microcavities [152] and similar to the CW pump intensity used in nonlinear imaging of micron scale 2D semiconductor flakes [167].

Figure C.1a shows the optical tweezer setup combined with a DNH plasmonic aperture as the trapping site. A CW 973 nm diode laser beam was collimated, expanded, and focused through a 100× microscope objective (1.25 NA) into the DNH gap. The transmitted signal was collected by a 10× microscope objective (0.25 NA) and measured by an avalanche photodiode (APD – Thorlabs, APD120A) (Figure C.1b). The reflected pump and the emitted SHG signals were collected by the 100 × microscope objective and by using a shortpass dichroic mirror (Thorlabs, DMSP805) routed to

a spectrometer (Ocean Optics, QE65000) and a CCD camera. A bandpass filter (Thorlabs, FGB37), and a shortpass filter (Thorlabs, FES0750) were used before the spectrometer to attenuate the fundamental peak. The laser polarization was adjusted along the short axis of the DNH to achieve maximum transmission. hBN nanoflakes were trapped for incident laser powers $\geq$7.5 mW and remained trapped when the laser power was reduced to the few mW range. Note that it is possible to obtain battery operated lasers at this power level [152].

The inset of Figure C.1a shows an SEM image of a typical DNH with aperture diameter of 300 $\pm$ 10 nm and gap size of 90 $\pm$ 10 nm. These DNHs were fabricated in a gold film on a glass substrate using the colloidal lithography method [8]. Briefly, a 30 μL solution of 300 nm diameter polystyrene spheres in ethanol was drop-coated on a glass microscope slide. After evaporation, a 5 nm titanium adhesion layer followed by a 70 nm gold film was deposited on the sample using a sputtering system (Mantis). The Au-Ti coated sample was sonicated for 5 minutes in ethanol to remove the polystyrene nanospheres and to leave DNH apertures on the film.

We used hBN nanoflakes (Graphene Supermarket) with 1 to 5 layers thickness and 50-100 nm width, many orders of magnitude smaller than microcavities and other similar structures. An atomic force microscopy image of hBN nanoflakes drop-coated on a silicon substrate is shown in the Supporting Information. The height profile shows that the hBN nanoflake was 3 to 4 layers thick and 70 nm wide (see Supporting Information). This was typical of the samples over 15 measurements. To

make a trapping chamber containing a solution of hBN nanoflakes, a spacer layer followed by a glass cover slip where placed on top of the DNH patterned gold film.

Figure C.1b shows trapping of individual flakes, observed by a jump of the signal in the APD. The signal was converted to the transmitted power (μW) by using the APD specifications: responsivity of 6 A/W at 973 nm and transimpedance gain of 50 kV/A. Simultaneous with observation of the trapping, a SHG signal at 486.5 nm was detected from the emitted signal to the spectrometer. Before trapping of the hBN flake we did not observe any SHG signal, even in high laser powers.

Figure C.1c shows the spectrum featuring both the pump laser (973 nm) and the second harmonic (486.5 nm) for an incident laser power of 13.25 mW measured before the 100 $\times$ microscope objective (see Supporting Information). Considering the shortpass dichroic mirror and the filters before the spectrometer, the fundamental peak was attenuated by a factor of 2×10^8 and the SHG peak was attenuated by a factor of 4.

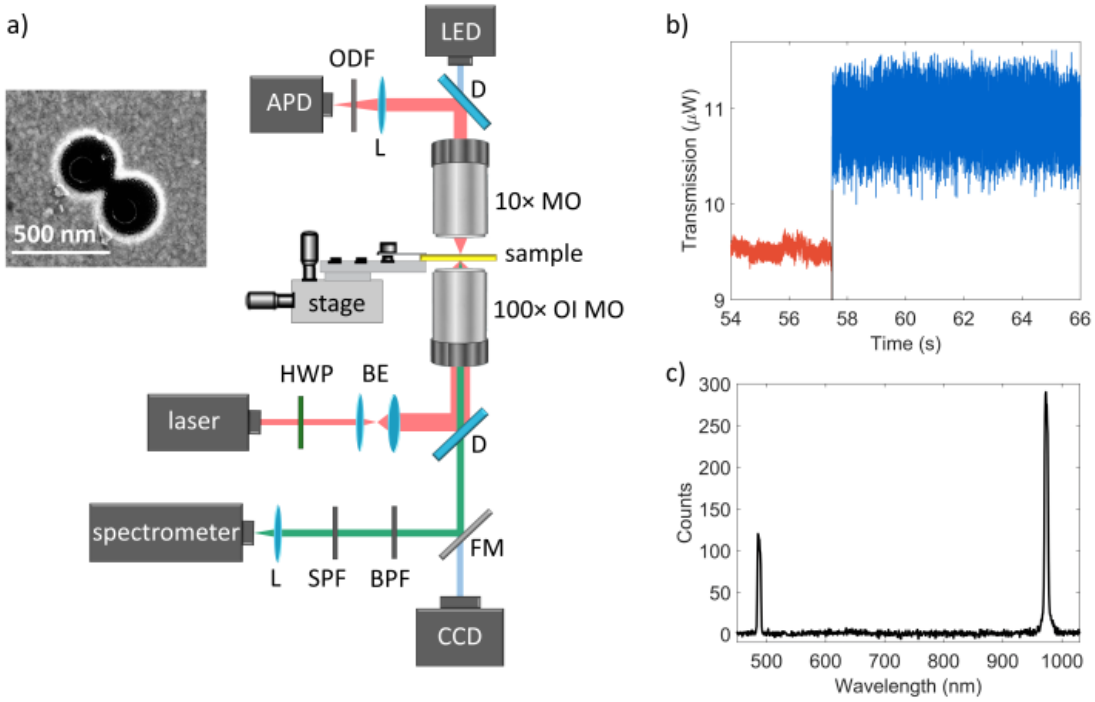

Figure C.1: Experimental setup. (a) Schematic of the DNH laser tweezer setup: charge-coupled device (CCD) camera, flip mirror (FM), shortpass filter (SPF), band-pass filter (BPF), lens (L), half-wave plate (HWP), beam expander (BE), shortpass dichroic mirror (D), 100 × oil immersion microscope objective (OI MO), piezo stage (stage), 10 ×microscope objective (MO), optical density filter (ODF), and avalanche photodetector (APD). Inset: scanning electron microscope (SEM) image of a typical DNH with aperture diameter of 300 ± 10 nm and gap size of 90 ± 10 nm. (b) Typical one-step trapping event of hBN nanoflakes: untrapped state (red), transition from untrapped to trapped (black), and trapped state (blue). Data is plotted in three colors to indicate the trapping state. (c) The spectrum of the fundamental beam at 973 nm and the SHG signal at 486.5 nm measured in a trapping event with a 3 s acquisition time. With filters, the fundamental peak was attenuated by 2×10^8 and the SHG peak was attenuated by 4. Background counts were subtracted [11]. Copyright 2021, American Chemical Society.

Figure C.2 shows the power-dependence of SHG from the trapped hBN nanoflake. Varying the incident laser power, SHG counts for the transmitted power in the APD was obtained for two paths: increasing the laser power from 7.5 mW to 13.25 mW (blue), then decreasing the laser power from 13.25 mW to 3 mW while the hBN was still trapped (red). The SHG signal was measured in the spectrometer and the transmitted power was obtained by the APD. For a DNH with 300 nm diameter and 90 nm gap size, when an hBN nanoflake was trapped, $\sim$0.5 % of the incident laser power transmitted through the DNH aperture. This value was obtained without considering the neutral density filters in front of the APD. The slope was 2.1 ± 0.2 on a log-log scale, consistent with a second order process where a slope of 2 is expected. Care was taken to ensure that the flake was stable during the measurement, and that the power-dependence did not exhibit hysteresis effects when scanning the power up and down. In some cases, the trapping showed jumps that we believe are the result of the flakes physically changing in the trap (perhaps layers shifting or being lost), resulting in a change in the harmonic generation power (see Supporting Information). Care was taken to avoid those events in the power measurements.

While we cannot definitively identify the stacking configuration, we have performed repeated measurements and found a variation of around 9 times (comparing 23 measurements) between various flakes trapped. Since we have 1-5 monolayers, we would expect a variation of around 25 if the harmonic varied with as the square of the number of layers, which is not the case and suggests that AB stacking is unlikely

and the variation is related to particle size alone [168].

We also measured tungsten disulfide (WS_2) and molybdenum disulfide (MoS_2) flakes (Graphene Supermarket), which showed SHG, albeit at a lower level (see Supporting Information). We suspect the lower signal from MoS_2 and WS_2 resulted from being away from the exciton peak where these materials give their largest enhancement (which peaks around 440 nm for the SHG) [167]. Those flakes were larger than hBN flakes and a larger aperture was used, so the lower harmonic generation may also be the result of lower plasmonic enhancement. In the past, MoS_2 showed a larger second harmonic response than hBN [169].

We measured the SHG response of lithium niobate ($LiNbO_3$) nonlinear nanocrystals to compare the above 2D materials with bulk ones at the nanoscale. The 2D material has a significantly higher response (see Supporting Information). Here we compared the SHG of trapped $LiNbO_3$ nanoparticles of two different sizes, 30 nm and 55 nm diameters [170, 171], and found that the SHG from hBN nanoflakes for the same incident laser power was $\sim$60 times and $\sim$90 times larger. This is the first time that such a signal has been seen from extremely subwavelength particles using a CW laser (low peak power). This high efficiency can be used to measure below bandgap signals by SHG upconversion followed by linear detection.

We confirmed that there was no SHG in the absence of these materials, or when trapping materials with inversion symmetry, like polystyrene (see Supporting Information). This shows that the signal was not coming from the nanostructured metal

surface.

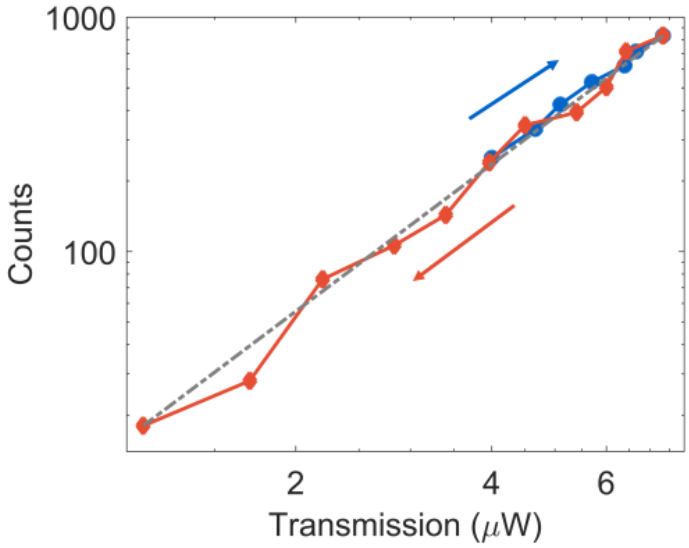

Figure C.2: SHG power-dependence measurement from a trapped hBN nanoflake. For the trapped hBN nanoflake, SHG counts for varying of laser power was measured from the transmission signal in the APD for two paths: first the laser power was increased from 7.5 mW to 13.25 mW (blue). Then, the power was decreased from 13.25 mW to 3 mW while the hBN was still trapped (red). The dashed-line is a fit to the power decreasing data. The transmission measurements are shown in the Supporting Information. The power-dependence of SHG gives a slope of 2.1 ± 0.2 on a log-log scale [11]. Copyright 2021, American Chemical Society.

We analyzed the plasmonic enhancement to understand how SHG can be observed from nanoflakes. The finite-difference time-domain (FDTD) simulations showed 500 times enhancement in the local field intensity at the fundamental wavelength, as shown in Figure C.3a. This alone is already comparable to the enhancement seen for pulsed lasers, keeping in mind that photons are being generated continuously

(whereas they arrive only at the time of the pulse in pulsed measurements). We found a Purcell factor enhancement of 450 at the second harmonic wavelength (see Figure C.3b), thereby increasing the efficiency of generation at that wavelength still further. Combined, we believe that these effects account for the strong harmonic generation observed in our experiments, even though a low-power CW laser was used and the particles were nanoflakes. The local field intensity and Purcell enhancement were localized to a region of the order of a few nanometers wide (see Supporting Information), therefore, most of the generation is coming from a small region of the sample, even smaller than the nanoflake itself.

The optical tweezer plays a role in enhancing the SHG signal as well. This is because it naturally positions the nanoparticle in the highest intensity region, thereby maximizing the harmonic generation signal [172]. In the FDTD simulations with various orientations, it appears that having the nanoflake oriented flat along one cusp gives the largest transmission change, as compared to orientations between the cusps. Therefore, we suspect that this is the preferred orientation in the trap (see Supporting Information).

We performed autocorrelation measurements on the sample and found intensity fluctuations on the timescale of $\sim$1 ms, which is comparable to past experiments on nanoparticles in the DNH setup [4], so there is similar efficiency in trapping to that previous work. Aperture based optical tweezers have been used to enhance the emission from single quantum dots [114] and upconverting emitters [9], even at the

single ion level [173]. While thermal effects can play a role in enhancing or hindering trapping as well, we do not study these effects in the present work since trapping was achieved routinely on a timescale of the order of a minute [174, 175].

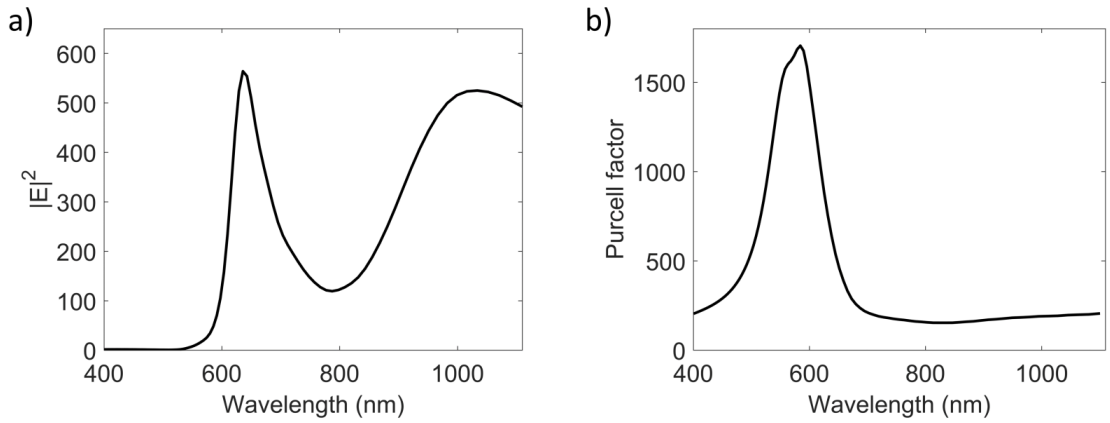

Figure C.3: Local field intensity spectrum and Purcell factor. (a) The electric field enhancement spectrum in the gap region of a DNH with 90 nm gap size and 300 nm diameter in 70 nm gold film. $|E|^2$ was normalized to the corresponding intensity of the source wave in vacuum. The dipole was oriented along the DNH cups axis where it was 2 nm away from the tip of the cusp. (b) Purcell factor enhancement obtained by the FDTD simulations in the gap region [11]. Copyright 2021, American Chemical Society.

We note that femtosecond lasers were used in previous plasmonic enhancement measurements of 2D materials [176]. In that work, perhaps as a result of the geometry, only 300 times enhancement was seen from the plasmonic structure. We also note that there is a work on nonlinear photoemission of electrons from nanostructures with a 60 mW CW laser [177].

In conclusion, we have demonstrated SHG from individual hBN nanoflakes using

a CW laser. While DNHs were used to enhance the subwavelength field in this study, they are only one example of nanostructured metals and this can be generalized to other geometries for subwavelength imaging or information processing. For example, the ability to generate SHG from hBN nanoparticles allows for doubling the frequency of photons and thereby allows detection of below bandgap photons through a second harmonic scheme using Si photonics – in other words silicon-based detectors can be used while the data is transmitted along silicon waveguides that do not absorb because the bandgap is larger than the photon energy before the frequency is doubled by SHG. We believe that these results are promising for dense integration of optical information processing on chip, and for nonlinear optical imaging using plasmon-enhanced nanoflakes as labels with a low-power and inexpensive laser source. There is also the possibility of interacting with plasmonically enhanced defect states [178] via a two-photon scheme, enhanced by the natural local second harmonic generation.

C.2 Supporting Information: Single Nanoflake Hexagonal Boron Nitride Harmonic Generation with Ultralow Pump Power

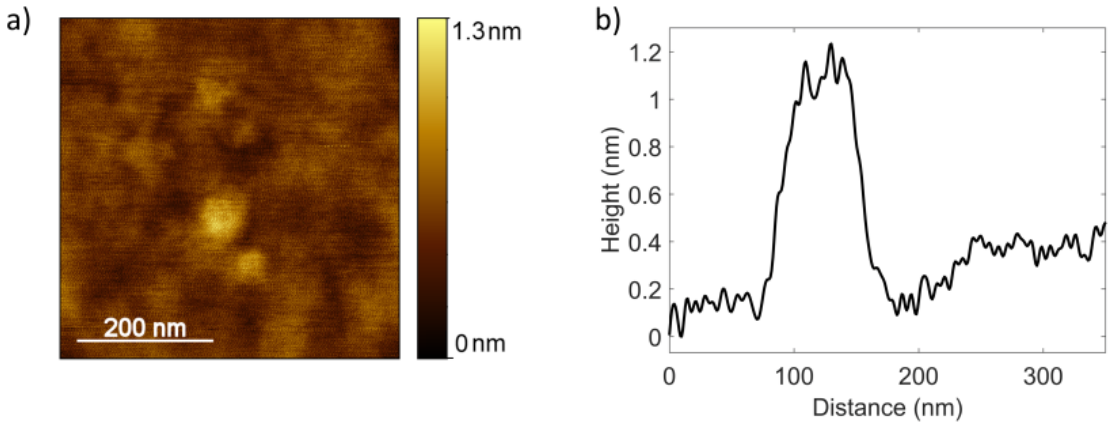

Figure C.4: (a) An AFM image of hBN nanoflakes on a silicon substrate. (b) Height profile of the hBN nanoflake shows that the hBN nanoflake [11]. Copyright 2021, American Chemical Society.

Figure C.4 shows an atomic force microscopy (AFM) image of hBN nanoflakes drop-coated on a silicon substrate. The height profile shows that the hBN nanoflake was 3 to 4 layers thick and 70 nm wide.

Figure C.5 shows the transmitted power for the data provided in Figure 2 of the main text. The transmitted power was measured for varying the incident laser power in the hBN trapping event. The measurement was conducted along two paths:

increasing the incident power from 7.5 mW to 13.25 mW. Then decreasing the incident laser power to 3 mW while the hBN was still trapped. To eliminate drift, the laser power was returned to the initial value of 7.5 mW before each change. In this measurement ∼0.5 % of the incident laser power was transmitted through the DNH aperture in the trapping event.

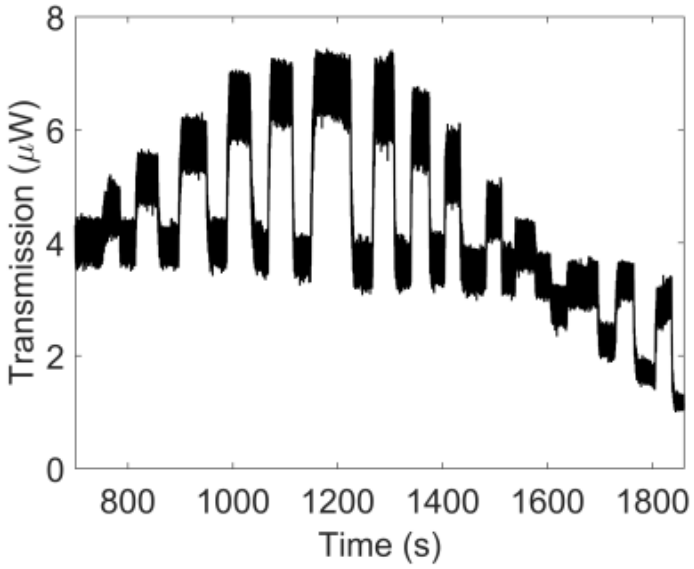

Figure C.5: The transmitted power in the APD for an hBN trapping event for varying the incident laser power. The measurement was conducted along two paths while an hBN was trapped: increasing the incident power from 7.5 mW to 13.25 mW. Then the incident power was decreased to 3 mW while the hBN was still trapped. To avoid drifting, the laser power was returned to the initial value of 7.5 mW before each change. The y-axis shows the transmitted power detected in the APD. In this measurement ∼0.5 % of the incident laser power was transmitted through the DNH aperture in the trapping event [11]. Copyright 2021, American Chemical Society.

As shown in Figure. C.6, signals from trapped hBN nanoflakes could have multiple

jumps, which we believe are the result of the flakes physically changing in the trap (perhaps layers shifting or being lost). Care was taken to avoid those events in the power measurements.

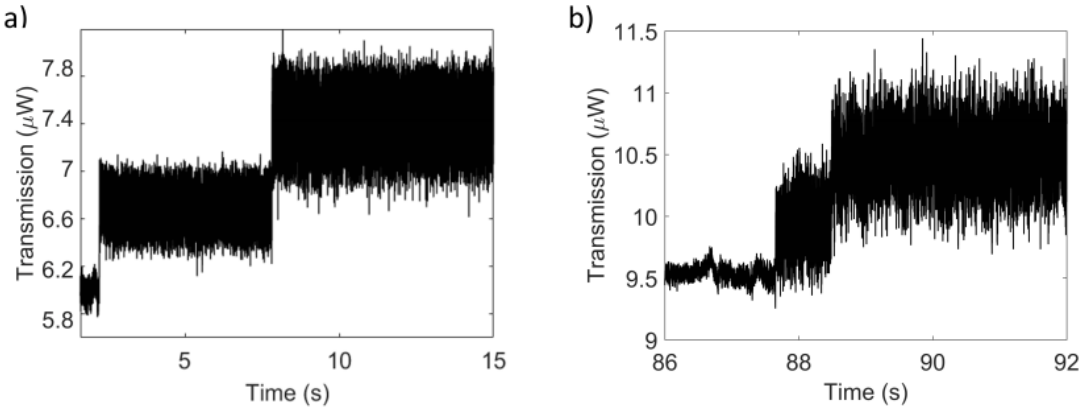

Figure C.6: Occasional jumps in trapping of hBN. (a,b) two trapping events of hBN nanoflakes with jumps [11]. Copyright 2021, American Chemical Society.

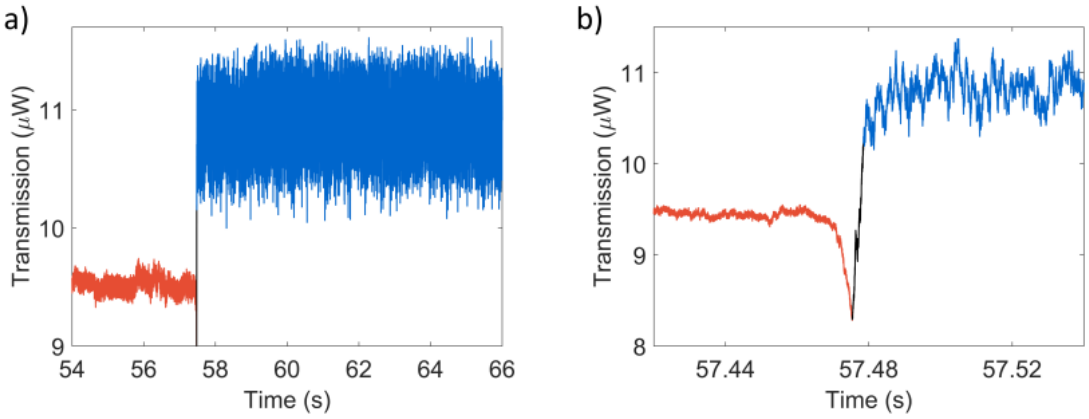

Figure C.7: Trapping of an hBN nanoflake. The untrapped state (red), transition from untrapped to trapped (black), and trapped state (blue) of one trapping event. (a) A 12 second span, (b) zoomed in section of the same measurement. Data is plotted in three colors to indicate different trapping states [11]. Copyright 2021, American Chemical Society.

Figure C.7 shows a zoomed section of the trapping measurements. Data is plotted in three colors to indicate the transition from untrapped to trapped.

Figure C.8 presents the SHG and fundamental spectra for a trapping event with applied laser power of 13.25 mW and a 3 second acquisition time.

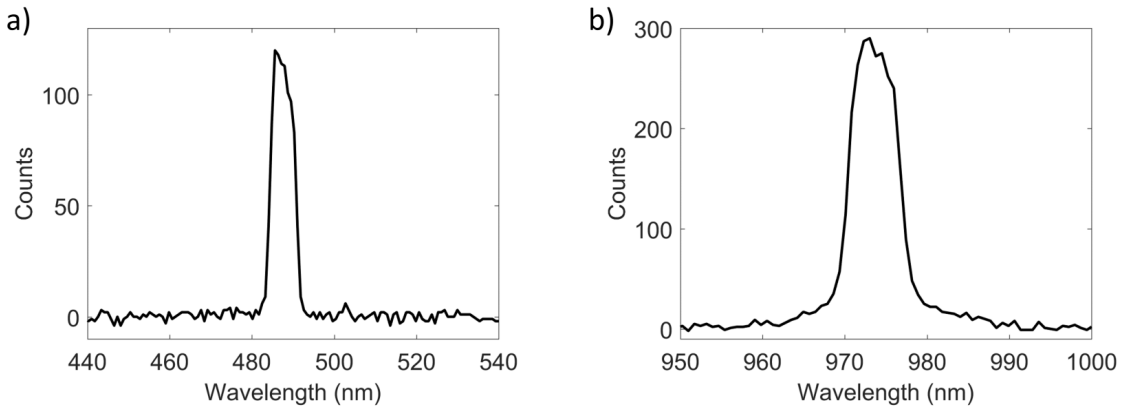

Figure C.8: Spectrum of the fundamental beam and the SHG signal form an hBN trapping. (a) Spectrum of the SHG signal. (b) Spectrum of the fundamental beam. Emitted signal was collected by the 100 × microscope objective and directed to the spectrometer and the CCD camera using a shortpass dichroic mirror. With the dichroic mirror and filters before the spectrometer, the fundamental peak was attenuated by a factor of 2×10^8 and the SHG peak was attenuated by a factor of 4. Measurement was done with 13.25 mW incident laser power with a 3 s acquisition time. Background counts were subtracted [11]. Copyright 2021, American Chemical Society.

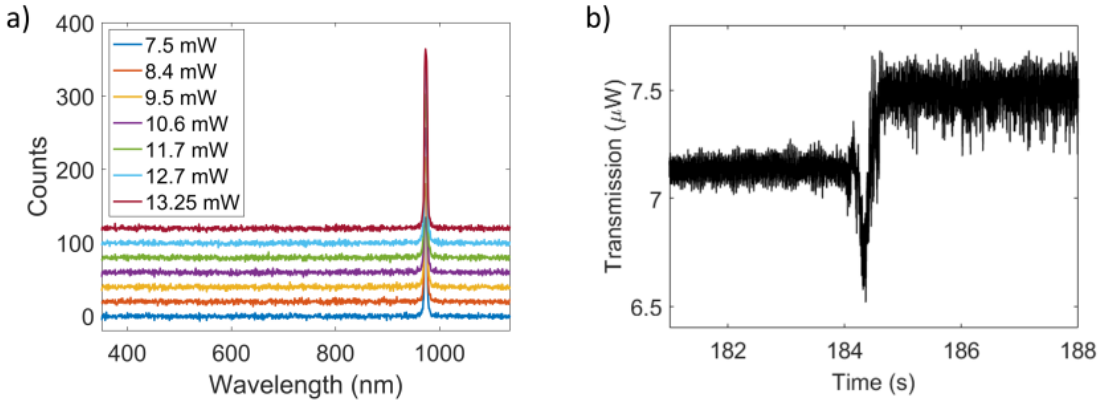

Figure C.9: Trapping polystyrene nanospheres. (a) Reflection spectrum for varying the incident laser power between 7.5 mW and 13.25 mW, for 20 nm diameter polystyrene nanospheres trapped in a DNH with 25 nm gap size. The reflection spectrum only showed the laser peak (973 nm) confirming that there was no SHG when trapping polystyrene. Spectra were shifted 20 counts in the y-axis for each laser power. (b) Typical trapping event of a 20 nm polystyrene nanoshpere with 973 nm laser [11]. Copyright 2021, American Chemical Society.

We conducted the same measurements for 20 nm diameter polystyrene nanospheres in DNH apertures with 90 nm and 25 nm gap size, confirming that there was no SHG when trapping materials with inversion symmetry. Figure C.9 shows the trapping of 20 nm diameter polystyrene nanospheres using a 25 nm gap size DNH for varying the incident laser power between 7.5 mW and 13.25 mW. In Figure C.9a spectra were shifted 20 counts in the y-axis for each laser power.

Conducting the measurement with pure water samples confirmed that there was no SHG in the absence of nanoflakes. Figure C.10 shows the reflection measurements from deionized water on a 90 nm DNH for varying the laser power. These measure-

ments show that the SHG signal is not from the gold DNH apertures. Spectra are shifted 20 counts in the y-axis for each laser power.

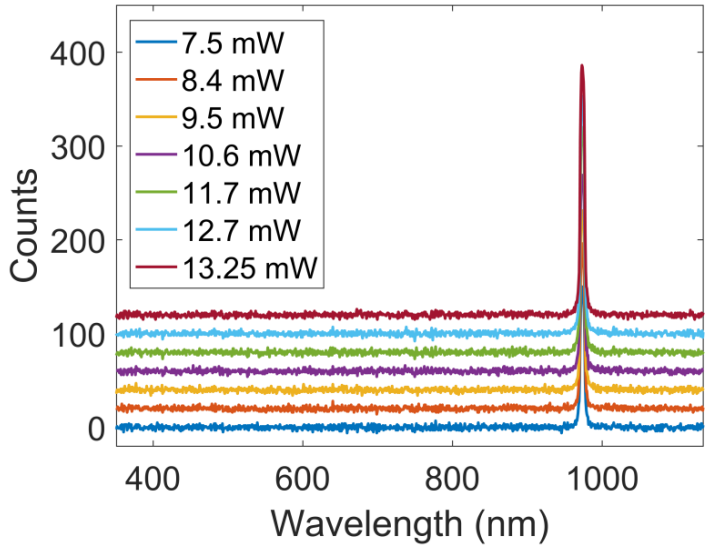

Figure C.10: The reflection spectrum of deionized water on a DNH aperture with 90 nm gap size for varying the laser power. Reflection spectra were measured for varying the laser power between 7.5 mW to 13.25 mW. The reflection spectrum showed the pump laser (973 nm) but did not have the second harmonic feature. Laser powers were measured before the 100 × microscope objective. Spectra were plotted with 20 counts shifts in the y-axis for each power [11]. Copyright 2021, American Chemical Society.

Figure C.11 shows the power-dependence SHG for trapped hBN, MoS_2, and WS_2 nanoflakes and $LiNbO_3$ nanoparticles. Comparing the SHG from hBN with MoS_2, and WS_2 nanoflakes showed higher SHG for the same incident laser power. MoS_2, and WS_2 flakes were larger and a larger aperture was used, so the lower harmonic generation was likely the result of lower plasmonic enhancement. The lower signal

from MoS_2 and WS_2 may resulted from being away from the exciton peak where these materials give their largest enhancement. Also, we compared the SHG of hBN nanoflakes with the SHG of $LiNbO_3$ nanoparticles of two different sizes of 30 nm and 55 nm diameters and showed that the SHG from hBN nanoflakes for the same incident laser power was ∼60 times and ∼90 times larger.

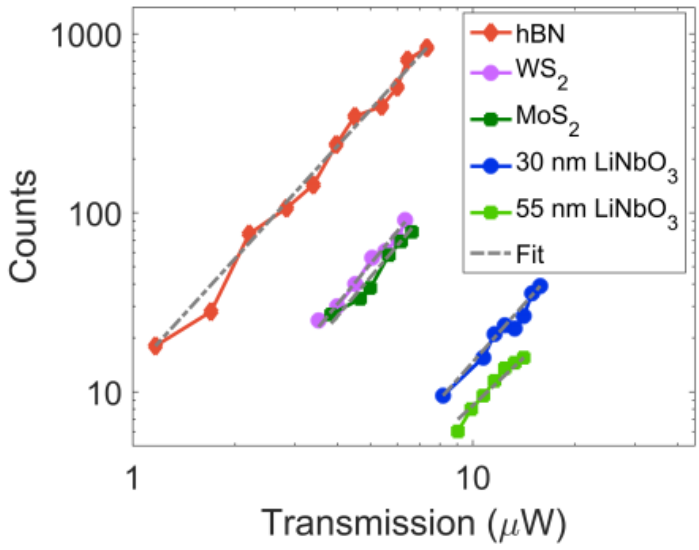

Figure C.11: SHG power-dependence of trapped hBN, MoS_2, and WS_2 nanoflakes and $LiNbO_3$ nanoparticles. SHG counts for varying of the incident laser power were obtained from the transmission signal in the APD. The dashed-lines illustrate the traces fit to the measured data. The power-dependence of SHG had a slope of 2.1 for hBN, 2.1 for WS_2, 2.1 for MoS_2, 2.1 for $LiNbO_3$ nanoparticle with 30 nm diameter size, and 2.1 for $LiNbO_3$ with 55 nm diameter size nanoparticles. Plot is on a log-log scale [11]. Copyright 2021, American Chemical Society.

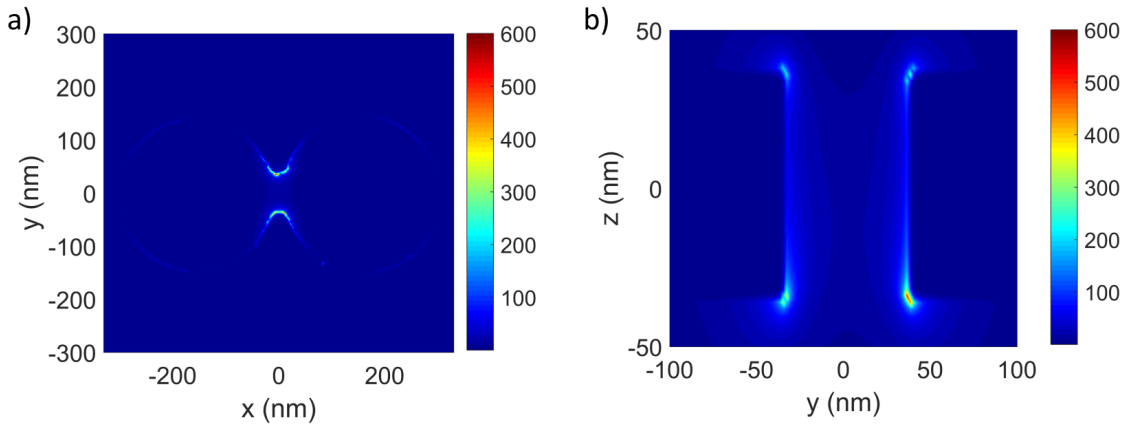

Figure C.12: Local field intensity enhancement. The FDTD simulation of the electric field distribution of a DNH with 90 nm gap size and 300 nm diameter aperture in a gold film at the fundamental wavelength, (a) the $x-y$ plane, (b) the $z-y$ plane. Figure 1a of the main text shows the electric field enhancement spectrum in the gap region. The FDTD simulations show a 500 times enhancement of the electric field intensity close to the cusps of the DNH at the fundamental wavelength [11]. Copyright 2021, American Chemical Society.

Figure C.12 shows the simulated electric field intensity distribution inside a DNH with 90 nm gap size and 300 nm aperture diameter in a 70 nm gold film predicted using the 3D finite difference time domain (FDTD) method (Lumerical Solutions Inc., version R2.3) at 973 nm wavelength. For the FDTD calculation, we used the following parameters: the simulation volume had dimensions of 1.5 μm $\times$ 1.3 μm $\times$ 1 μm in the x, y and z directions. A uniform mesh of 2 nm was used. Perfectly matched layers were used on all boundaries. A total field scattering field (TFSF) source with 400 to 1100 nm wavelength range was used illuminate to the DNH. The TFSF region dimensions in x, y, z directions were 1 μm $\times$ 1 μm $\times$ 0.2 μm and the source was

placed 100 nm away from the top of the structure. A 2D z-normal monitor was place in the middle of the film. Polarization of the TFSF source was along the short axis of the DNH. The refractive index of the background was 1.33 and the glass slide was 1.52. Johnson and Christy data [179] was used as the optical constants of the gold coating. The thickness of the gold layer was 70 nm. Figures C.12a and b show the electric field intensity profile in the $x-y$ and $y-z$ planes of the DNH inside the gap. The largest electric field intensity occurred at the at the tips of the gap of the DNH and close to the glass substrate.

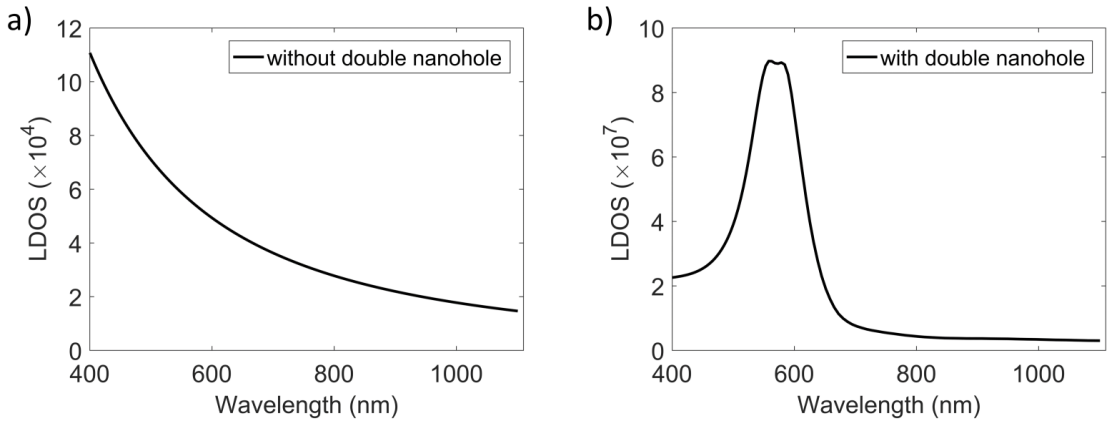

Figure C.13: Local density of optical states. FDTD simulations of the local density of optical states (LDOS) of a dipole source (a) without a DNH, (b) with a DHN at tips of the gap [11]. Copyright 2021, American Chemical Society.

The FDTD calculation showed a maximum Purcell factor enhancement of 450 at the second harmonic wavelength. This was found from the local density of optical states of a dipole source without a DNH (Figure C.13a) and with a DNH (Figure C.13b). The LDOS with the DNH was divided by the free-space LDOS to find

the Purcell enhancement factor at the second harmonic wavelength at the location of highest intensity.

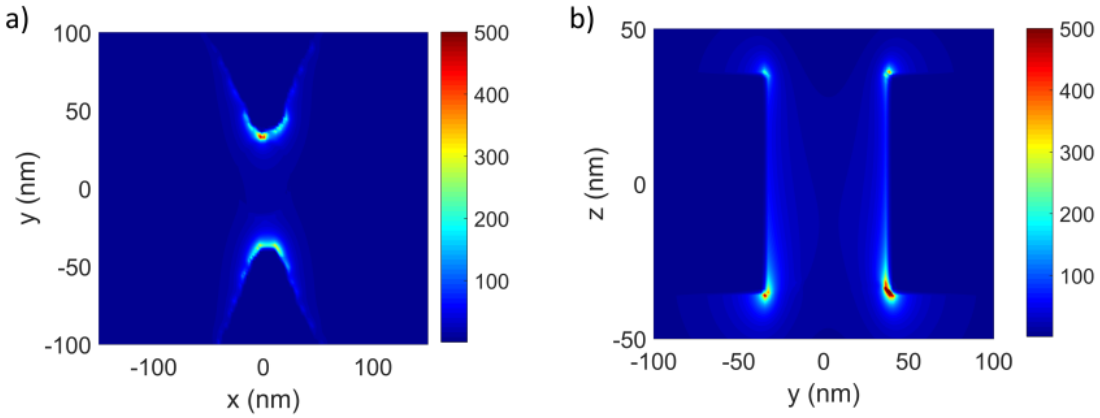

Figure C.14: Local field intensity enhancement for an hBN particle oriented in the $x-y$ plane. The FDTD simulation of the electric field distribution of a DNH with 90 nm gap size and 300 nm diameter aperture in a gold film at the fundamental wavelength with an hBN particle oriented in (a)the $x-y$ and (b) the $y-z$ plane [11]. Copyright 2021, American Chemical Society.

Figures C.14, C.15, and C.16 show the field intensity distribution and transmission (Figure C.17) spectra for an hBN nanoflake with various orientations in the trap site, obtained using the FDTD simulations. It appears that having the nanoflake oriented flat along one cusp gives the largest transmission change, as compared to orientations between the cusps. Therefore, we suspect that this was the preferred orientation in the trap [180]. For the FDTD simulations an hBN nanoflake located in the $x-z$, $y-z$, and $x-y$ planes of the cusp of the DNH. The DNH was placed in the $x-y$ plane. TFSF source was placed 0.1 μm away, on top of the DNH with polarization aligned to

the cusp axis of the DNH. The source had a wavelength range of 800 to 1200 nm. The mesh size and geometry were chosen with respect to the position of the nanoflake. A 2 nm mesh size was chosen for the axes in the plane of the nanoflake, and a 1 nm mesh size was used in the planes perpendicular to the plane of the nanoflake. The hBN nanoflake was 50 nm diameter and was 2 nm thick. The monitors were located in the $x-y$ and $y-z$ planes. A refractive index of 2.227 was used in the directions parallel to the plane of the nanoflake and a refractive index of 1.726 [180] was used in the direction perpendicular to the plane of the nanoflake, due to its anisotropic properties.

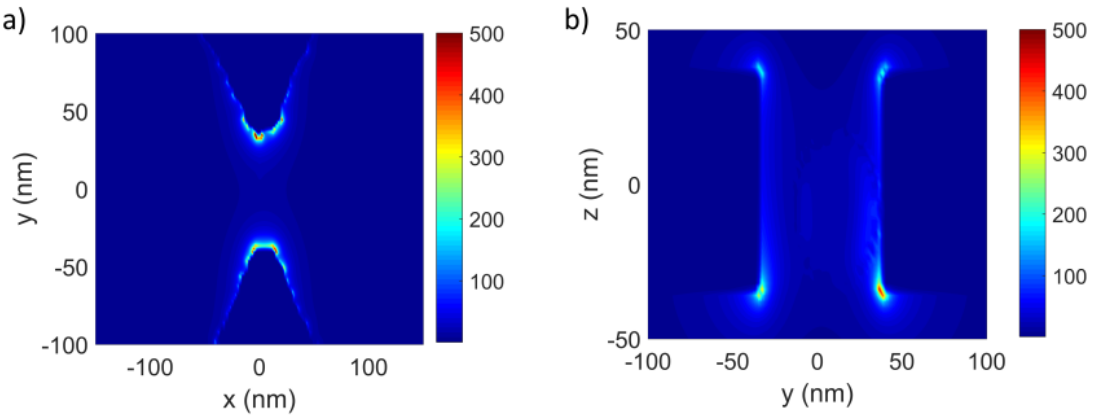

Figure C.15: Local field intensity enhancement for an hBN particle oriented in the $y-z$ plane. The FDTD simulation of the electric field distribution of a DNH with 90 nm gap size and 300 nm diameter aperture in a gold film at the fundamental wavelength with an hBN particle oriented in (a) the $x-y$ and (b) the $y-z$ plane [11]. Copyright 2021, American Chemical Society.

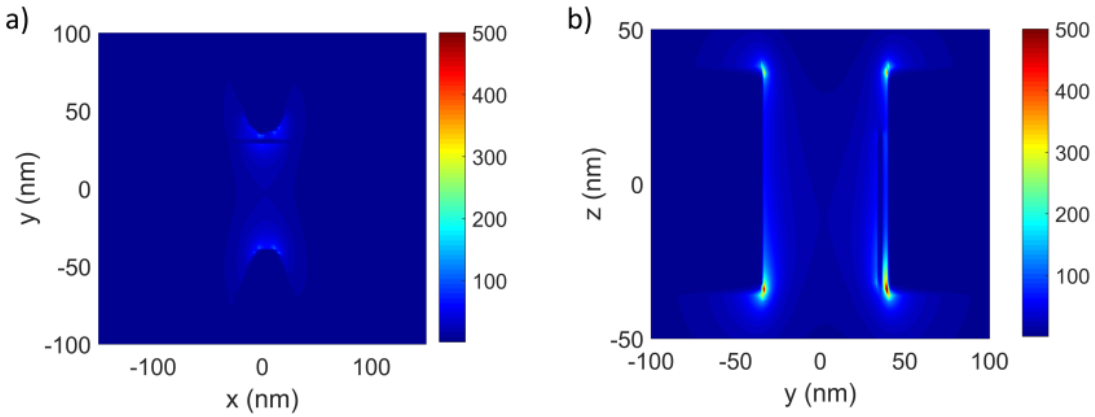

Figure C.16: Local field intensity enhancement for an hBN particle oriented in the $x-z$ plane. The FDTD simulation of the electric field distribution of a DNH with 90 nm gap size and 300 nm diameter aperture in a gold film at the fundamental wavelength with an hBN particle oriented in (a) the $x-y$ and (b) the $y-z$ plane [11]. Copyright 2021, American Chemical Society.

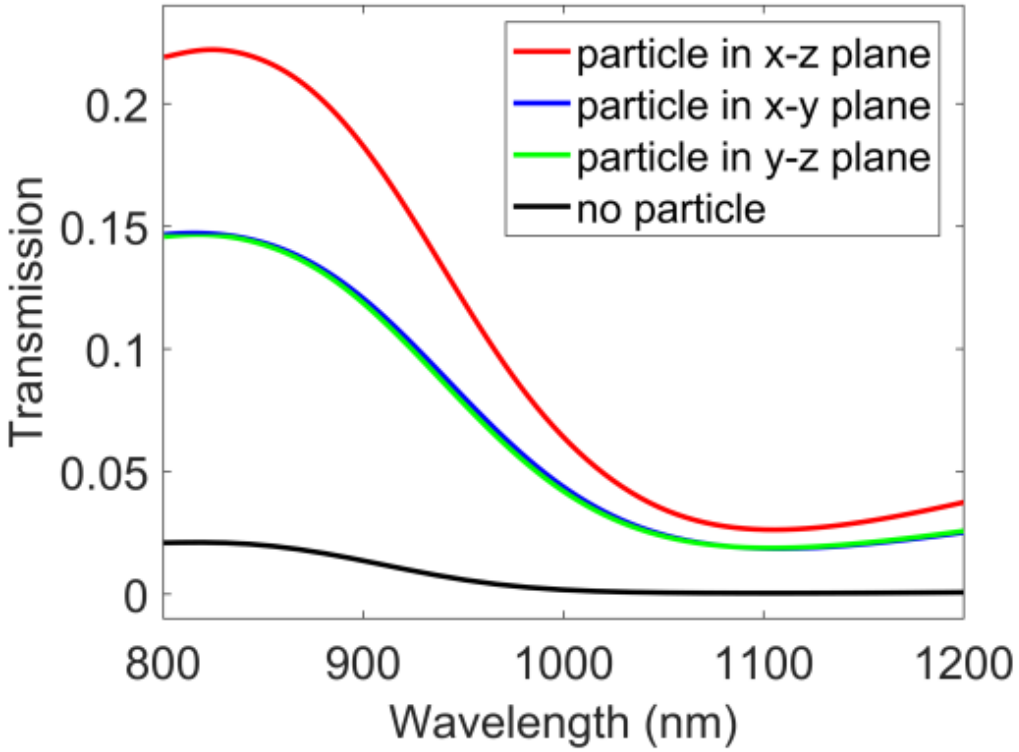

Figure C.17: The FDTD simulations of transmission for an hBN nanoflake with various orientations in the cusp of a DNH with 90 nm gap size and 300 nm diameter aperture [11]. Copyright 2021, American Chemical Society.

Appendix D

Isolating and Enhancing single-photon Emitters for 1550 nm Quantum Light Sources using Double Nanohole Optical Tweezers [12]

Z. Sharifi, M. Dobinson, Gh. Hajisalem, M. S. Shariatdoust, A. L. Frencken, F. C. J. M. van Veggel, R. Gordon, Isolating and Enhancing single-photon Emitters for 1550 nm Quantum Light Sources using Double Nanohole Optical Tweezers, The Journal of Chemical Physics, 154(18), 184204 (2021).

D.1 Isolating and Enhancing single-photon Emitters for 1550 nm Quantum Light Sources using Double Nanohole Optical Tweezers

D.1.1 Abstract

Single-photons sources are required for quantum technologies and can be created from individual atoms and atom-like defects. Erbium ions produce single-photons at low-loss fiber optic wavelengths, but they have low emission rates, making them challenging to isolate reliably. Here, we tune the size of gold double nanoholes (DNH) to enhance the emission of single erbium emitters, achieving 50× enhancement over rectangular apertures previously demonstrated. This produces enough enhancement to show emission from single nanocrystals at wavelengths not seen in our previous work i.e., 400 nm and 1550 nm. We observe discrete levels of emission for nanocrystals with low numbers of emitters and demonstrate isolating single emitters. We describe how the trapping time is proportional to the enhancement factor for a given DNH structure, giving us an independent way to measure the enhancement. This shows a promising path to achieving single emitter sources at 1550 nm.

D.1.2 Introduction

Single-photon sources are a key component for many quantum technologies and many efforts have explored using single atoms and atom-like defects as single emitters. Rare-earth ions have been found to be good candidates for single emitters as they produce stable emission and their quantum state can be controlled [181, 182, 183, 184]. The need for a stable single-photon source that has high transmission efficiency in optical fibers is only increasing as quantum communication becomes more advanced [185, 186, 187]. This motivates the search for a source of single-photons at low-loss telecom wavelengths for long-distance fiber propagation. Erbium is of particular interest as it emits in the C-band, the lowest-loss band for fiber transmission, a characteristic which is already widely used in erbium-doped fiber amplifiers for long-distance telecommunications [188]. Single erbium emitters have also been demonstrated, but a remaining challenge is finding a reliable method to isolate single emitters [189].

Methods of producing single emitters typically yield random distributions and most rely on either searching among them or using low concentrations to find the single emitters [190, 182]. Isolating single rare-earth emitters is particularly challenging as they have low emission rates due to long excited state lifetimes [181]. Some approaches have been explored to isolate rare-earth emitters by precisely implanting ions in crystals, making the process nearly deterministic but suffering from low yield [191].

Our group has previously demonstrated a scalable method of isolating single erbium emitters by measuring their discrete emission levels in an optical tweezer setup [173].

Plasmonics can be used to enhance the emission rate of single emitters and make isolating them more practical. Nanoscale structures can create plasmonic enhancement which concentrates the incident electric field, enhancing emission from luminescent particles by increasing the radiative emission and non-radiative decay rates [83, 192, 42, 193]. As applied to an Er-doped nanocrystal, this can allow a well-designed structure to increase its viability as a single-photon source [189, 194], and has other applications such as photocatalysis [195] and enabling subwavelength luminescence imaging with IR excitation [195]. Structures can also be designed with multiple plasmonic resonances, which has been shown before with aperture arrays in metal [196, 105, 9].

Plasmonic resonance not only enhances the emission, it also helps to isolate smaller particles, using the enhanced local field as optical tweezers [116, 2]. Optical tweezers are well-established and have been widely used to trap and manipulate nanoparticles [32], but trapping particles in the subwavelength scale typically requires high intensities when using conventional single beam traps. Rayleigh scattering also makes it challenging to trap and characterize small particles [32, 197]. Apertures in metal films can be used to enhance the local field through plasmonic resonance, and when applied to optical tweezers this makes it easier to trap subwavelength particles well below 100 nm with lower beam intensity [107, 197, 35, 109, 110, 111, 112]. Sev-

eral aperture designs have been evaluated in past works including double nanohole (DNH) [4, 113], bowtie [114, 115], and rectangular [116] apertures.

Our group has previously shown that using a rectangular aperture to trap Yb–Er-doped $NaYF_4$ nanocrystals enhances emission by a factor of 400 when tuned for both the excitation and emission wavelengths [9]. Rectangular apertures have also been used by our group to trap $NaYF_4$ nanocrystals with trace doping of Er, finding discrete levels of emission. The discrete levels indicate how many emitters are present in the trapped nanocrystal, allowing nanocrystals with single emitters to be reliably isolated [173]. DNH structures have been found to produce greater local field enhancement compared to rectangular apertures, which can make isolating single emitters easier [2]. These properties make DNHs useful for other applications as well, such as biosensing [198].

Here, we optically trap two different sizes of nanocrystals, made of $NaYF_4$ doped with 18% Yb and 2% Er, with plasmonic DNH aperture optical tweezers and characterize their emission spectra and trapping rate for different cusp separations. The DNH apertures exhibit multiple resonances within a single structure and further enhances the emission from individual nanocrystals by ˜50× compared to previous findings with rectangular apertures [9]. We also, for the first time, observe new resonances from nanocrystals trapped in a DNH at 400 nm and 1550 nm.

Using the DNH apertures with the best geometry, we optically trap nanocrystals made of $NaYF_4$ with low concentrations of Er^{3+}. We observe discrete emission levels

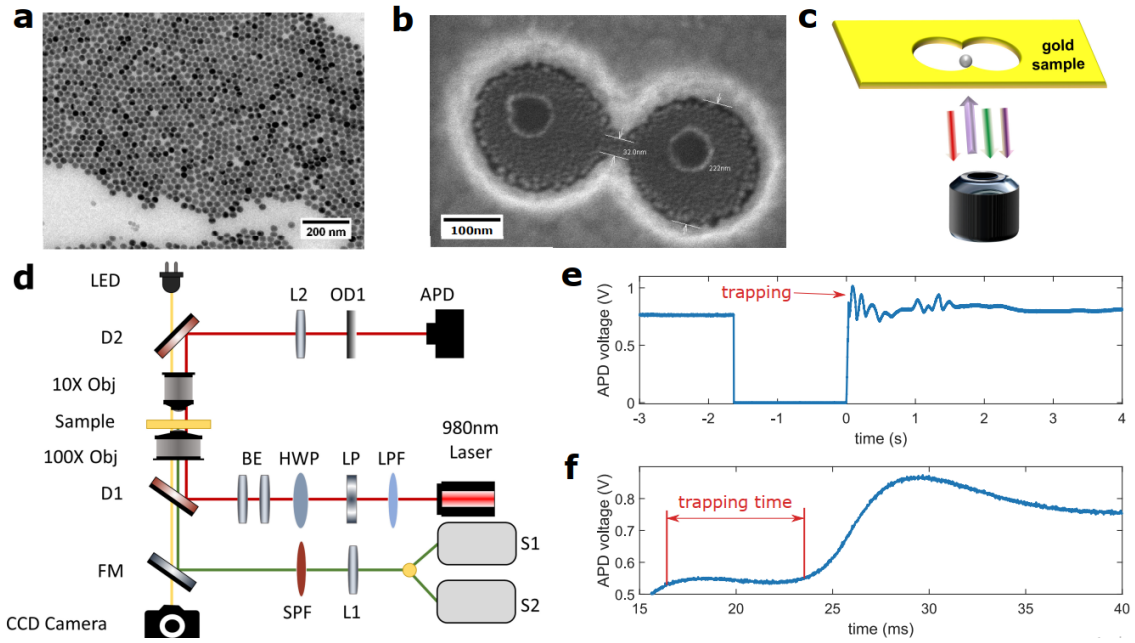

Figure D.1: Optical trapping of Yb–Er-doped $NaYF_4$ nanocrystals with DNH. (a) Image of $NaYF_4$ nanocrystals with nominal diameter of 26.2 nm. (b) Image of a fabricated DNH structure with 32 nm cusp separation and 222 nm aperture diameter, taken with scanning electron microscope. (c) Schematic of a trapped nanocrystal in a DNH aperture on a gold sample. (d) Schematic of optical tweezer setup. (e) Optical transmission through a 32 nm DNH aperture in a metal film trapping a 26.2 nm nanocrystal, as measured by the APD voltage. Laser is turned on at 0 s. (f) Magnified region showing the APD voltage change shortly after the laser is turned on and trapping time measurement. Copyright 2021, AIP Publishing LLC.

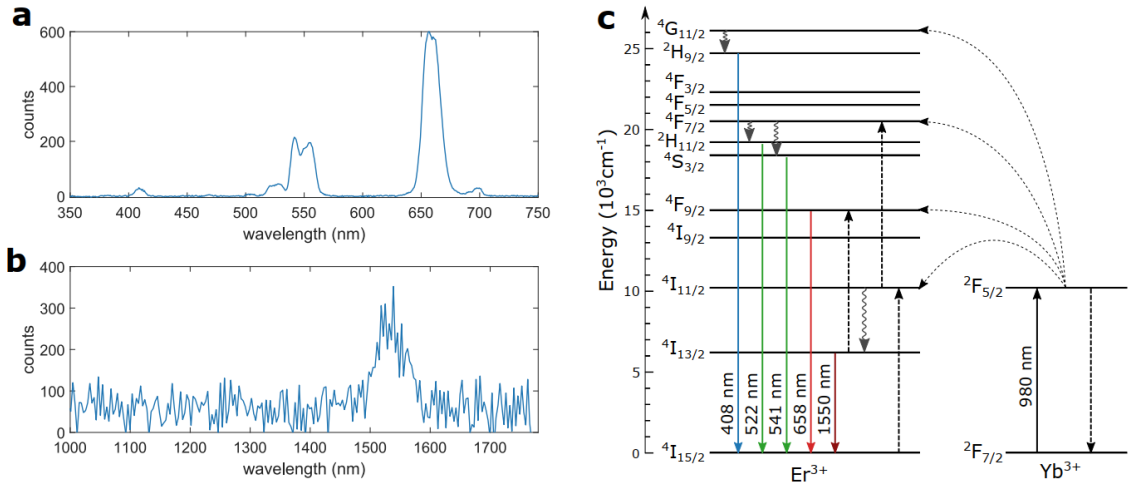

Figure D.2: Measuring the emission spectra from single nanocrystals. (a) Upconversion emission spectra from a 26.2 nm nanocrystal observed for a sample with 32 nm average cusp separation. The counts can be compared for 400, 550 and 650 nm emission peaks. Collected by a spectrometer with a 10 ms acquisition time. (b) Downshifting emission spectra from a 16.9 nm nanocrystal observed for a sample with 32 nm average cusp separation. Collected by a spectrometer with 1 s acquisition time. Copyright 2021, AIP Publishing LLC. (c) Schematic energy level diagram of Yb^{3+} sensitizer and Er^{3+} activator in nanocrystals. Radiative energy transfer (solid lines), non-radiative energy transfer (dotted lines), cross-relaxation (dashed lines), and multiphonon relaxation (curly lines). (Adapted from Suyver et al.) [199].

corresponding the different numbers of active emitters and isolate nanocrystals with single emitters. Furthermore, we explore the relation between the trapping dynamics and emission enhancement.

D.1.3 Tuning DNH Aperture to Maximize Enhancement

A range of DNH apertures with average cusp separations from 23 to 95 nm were fabricated to evaluate the emission enhancement. Cusp separation was the focus because the cusp is where DNH apertures produce the highest field intensity [200, 201]. Samples with DNH apertures are fabricated in a 70 nm thick gold film on a glass substrate using a colloidal lithography method previously reported on by our group [8]. Scanning electron microscopy was used to measure the average cusp separation of the DNH structures in each sample. Two different sizes of nanocrystals – nominally 16.9 nm and 26.2 nm in diameter, with standard deviations of 1.3 nm and 2.7 nm – were made of $NaYF_4$ doped with 18% Yb and 2% Er, dispersed in a hexane solution. Figure D.1a shows an image of the 26.2 nm nanocrystals. Figure D.1b shows an example of a DNH that was fabricated with a cusp separation of 32 nm and an aperture diameter of 222 nm. Figure D.1c shows a schematic of a nanocrystal trapped in a DNH aperture.

Figure D.1d shows a schematic of the optical tweezer setup used to trap the nanocrystals and measure the emission spectra and trapping characteristics. A single 980 nm continuous-wave laser is used for both trapping and excitation of the nanocrystals. Trapping is confirmed by the abrupt jump in the avalanche photodiode (APD) voltage which corresponds to the transmission of light through the aperture.

Figure D.1e shows the transmission of light through the DNH aperture and a

representative trapping event. The laser is briefly turned off and then turned back on at 0 s. The abrupt jump in the APD voltage, compared to before the laser was turned off, confirms the trapping event.

Figure D.1f shows how the trapping time is measured for the trapping event. After turning on the laser, there is a brief period (on the order of milliseconds) before a particle is trapped, this is the trapping time, t_t.

Figures D.2a and D.2b show the emission of a single Yb–Er-doped $NaYF_4$ nanocrystal trapped in a DNH aperture with 32 nm average cusp separation. Emission peaks are apparent in Fig. D.2a near wavelengths of 400 nm, 550 nm, and 650 nm. Figure D.2b shows the emission at 1550 nm of a single Yb–Er-doped $NaYF_4$ nanocrystal trapped in a DNH aperture, which we could not observe in our previous measurements [9].

We have not previously observed emissions at 400 nm and 1550 nm from single Yb–Er-doped $NaYF_4$ nanocrystals. The 400 nm upconversion emission is from the $^2H_{9/2} \rightarrow^4 I_{15/2}$ transition in erbium [199]. The 1550 nm downshifting emission is from the $^4I_{13/2} \rightarrow^4 I_{15/2}$ transition [188]. These transitions can be seen in the energy diagram shown in Figure D.2c. Observing these two transitions from single nanocrystals for the first time in our group is possible due to the higher enhancement achieved using the double nanoholes.

Figure D.3 shows the emission of the two sizes of Yb–Er-doped $NaYF_4$ nanocrystals using DNH apertures with varying average cusp separations. It illustrates how

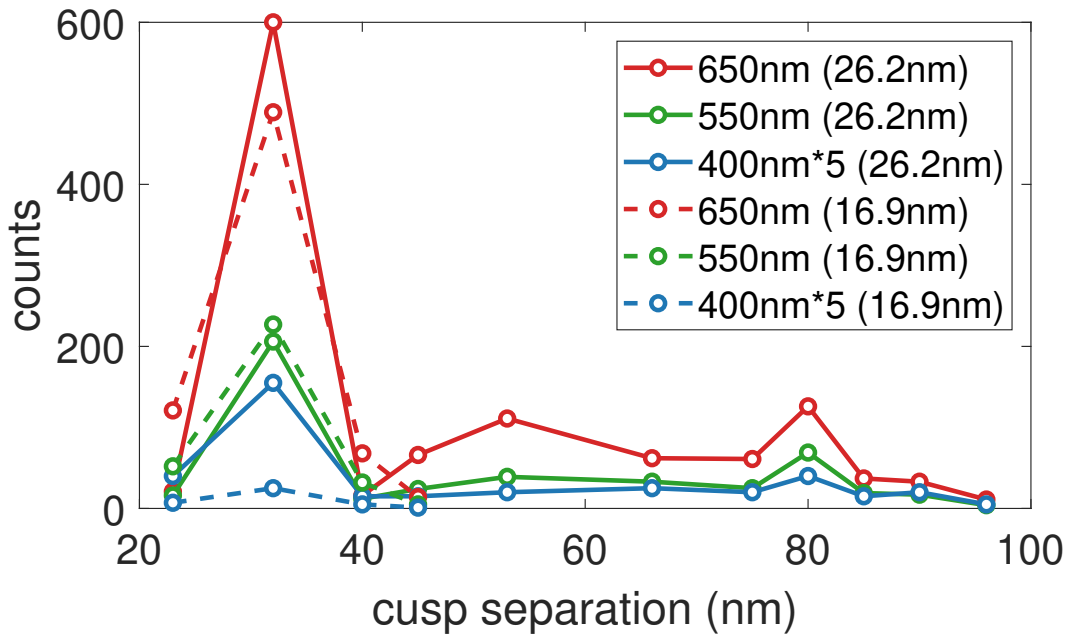

Figure D.3: Investigating the influence of the DNH cusp separation on emission enhancement. Emission from 17 nm and 26 nm nanocrystals at 400 nm, 550 nm, 650 nm for varying DNH cusp separations. Emission counts at 400 nm are multiplied by 5 for visibility.

the size and shape of the aperture can impact the overall emission. Several measurements on different DNHs within each sample were taken to confirm that the measured emission is from a single trapped nanoparticle. The average of these single trapping events is taken to form the final count. The normalized standard deviation over different measurements of a single 26.2 nm nanocrystal was 2.4%, 4.3% and 6.5% and for a single 16.9 nm nanocrystal it was 3.3%, 5.6%, and 4.8%, for the 400, 550 and 650 nm emission. The laser power is maintained at ˜9 mW (as measured before the 100× objective) to simultaneously excite the structure and trap the particle.

The emission and trapping characteristics of 26.2 nm Yb–Er-doped $NaYF_4$ nanocrystals are measured in ten different samples of DNH apertures with average cusp separations from 32 to 95 nm. We observe that the sample with 32 nm cusp separation has the largest emission and exhibits plasmonic resonance at additional wavelengths, 400 nm and 1550 nm, that are significantly larger than in apertures with other cusp separations. The emission was compared to previous results from our group which used the same experimental setup with rectangular apertures [9]. This aperture size showed additional enhancement factor of approximately 50, over the best rectangular aperture. With the 26.2 nm nanocrystals, enhancement at 400 nm can only be clearly seen in two samples–32 nm and 80 nm average cusp separation.

The 16.9 nm nanocrystals are used to probe the effect of smaller apertures as the 26.2 nm nanocrystals are too large to trap in DNHs with cusp separations under 32 nm. The 16.9 nm nanocrystals are too small to trap in DNHs larger than 45 nm,

so the measurements for these were performed for four different samples of DNH apertures with cusp separations from 23 to 45 nm. It was seen that the 32 nm cusp size remained the peak, showing that it has optimal plasmonic resonance to enhance emission at 650 nm. There was one isolated case where a nominally 26.2 nm nanocrystal was trapped in a nominally 23 nm gap, which is possible given the size tolerances.

These results show that the resonance wavelengths shifts as the cusp separation changes. The colloidal lithography method used to prepare these samples adjusts the cusp separation by changing the plasma etching time, this also affects the diameter of the apertures. Changing both the cusp separation and aperture diameter like this can impact both the enhancement factor and resonant wavelengths.

To probe this further we look at FDTD simulations (Lumerical FDTD ver. 2020 R2.3). The simulations calculated the electric field inside the cusp of the DNH structure where the particle would be trapped as shown in Fig. D.1c. The structures were modeled from SEM images similar to Fig. D.1b. A total of four different DNHs were modeled around the peak of interest at 32 nm cusp separation. Figure D.4a shows the simulated electric field intensity inside the cusp of a 32 nm DNH structure.

Figure D.4b shows the simulation result of the relationship between the near-field electric field intensity (normalized to the incident intensity) and wavelength inside the cusp of DNH structure with different cusp separations. It can be seen that the 32 nm cusp separation has the greatest overall electric field intensity. There are two main

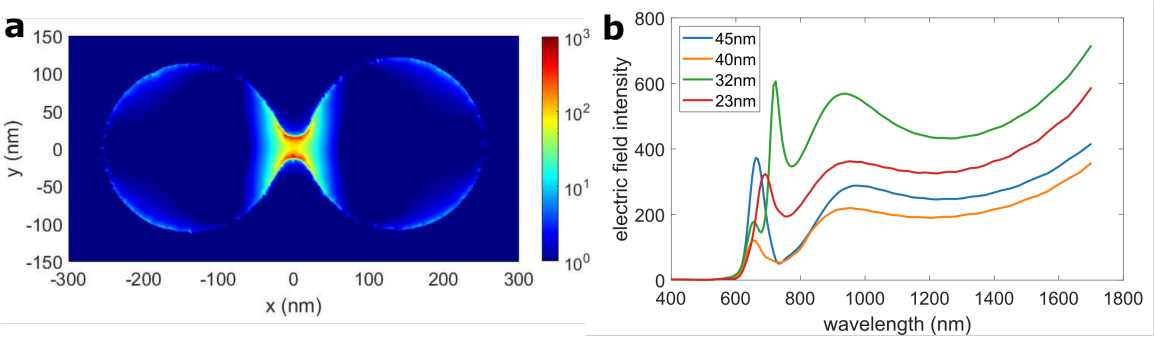

Figure D.4: Simulated electric field intensity. (a) Visualization of the electric field intensity inside of a DNH with 32 nm cusp separation. (b) Electric field intensity for DNHs with 22.7 nm, 32 nm, 40 nm, and 45 nm cusp separations. Normalized to the incident intensity. Copyright 2021, AIP Publishing LLC.

resonant peaks for each of the simulated DNH structures. The structure with 32 nm cusp separation has peaks at 720 nm and 940 nm. The simulations were performed based on single SEM images and as the resonance frequencies are sensitive to the curvature of the cusps and the exact separation it is expected that the peaks differ slightly from the experimental results. The simulations show that multiple resonances can be used to enhance both excitation and emission wavelengths. There is minimal field enhancement seen in the simulations at 400 nm, but experimental results show increased overall emission at that wavelength. This suggests that the main effect is seen at the excitation wavelength, increasing the energy transfer, with additional resonances for other wavelengths.

D.1.4 Observing Discrete Emission Levels

After finding that a DNH cusp separation of 32 nm shows the best enhancement with Yb-Er-doped nanocrystals, we applied this finding to search for and isolate nanocrystals with single erbium emitters. Dilute Er-doped $NaYF_4$ (with no Yb) nanocrystals were produced with a nominal diameter of 22.7 nm (standard deviation of 2.4 nm) and a nominal number of Er ions per nanocrystal of 2.48. It is expected that the Er^{3+} ions are statistically distributed within the $NaYF_4$ crystals following a Poisson distribution with $\lambda = 2.48$. As the nanocrystals have varying numbers of Er^{3+} ions, we expect to see emission counts with levels corresponding to the different number of ions that follows a similar distribution. Trapping was performed for 100 events using a DNH with 32 nm cusp separation, measuring the emission spectrum for each event.

Figure D.5a shows the upconversion emission from 640 nm to 680 nm of single nanocrystals as measured with a 1 s integration time. It can be seen that the emission is separated into discrete levels. We attribute these levels to the discrete numbers of erbium emitters in the nanocrystals, from zero to seven individual active emitters. The integrated emission counts give a clear way to distinguish between the distinct numbers of active erbium emitters. The experiment demonstrated a mean of 1.68 ± 0.17 active erbium emitters per nanocrystal. Compared to the expected mean from the synthesis, this gives a yield of 0.67 ± 0.07 which is consistent with previous findings

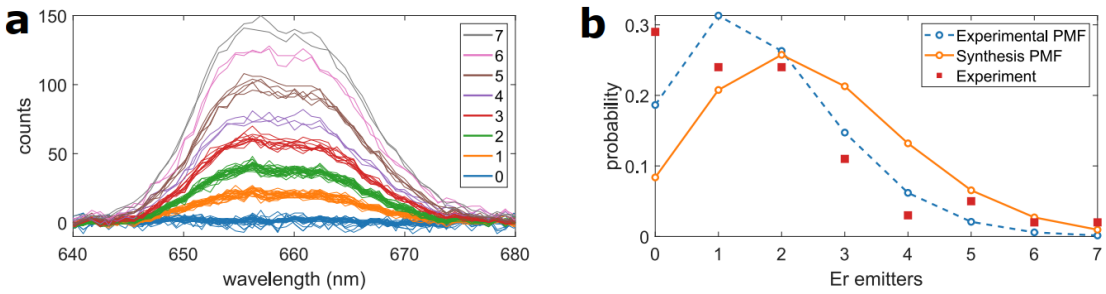

Figure D.5: Measuring discrete emission levels from low counts of erbium emitters. (a) Emission counts from nanocrystals showing discrete levels corresponding to different amounts of active erbium emitters. Collected by a spectrometer with a 1 s acquisition time. (b) Poisson probability mass functions (PMFs) for the experimental ($\lambda = 1.68$) and synthesis ($\lambda = 2.48$) and experimental probabilities for the number of Er emitters. Copyright 2021, AIP Publishing LLC.

from our group [173].

Figure D.5b shows the probability distributions of Er emitters per nanocrystal as expected from the synthesis and experimental means. This distribution makes the assumption that all Er^{3+} ions can emit photons. However, it is expected that surface quenching significantly reduces the emission from Er^{3+} ions near the surface of the nanocrystal [202]. A quenched layer of 1 nm leads to quenching of 24% of the Er^{3+} ions in the volume. This seems to be a plausible explanation considering the statistical uncertainty in the experimental results.

The emission measurements were collected with a spectrometer with a 1 s acquisition time. This is an improvement by over a factor of 40 compared to previous results from our group which required a 30 s acquisition time and produced even

fewer counts [173]. This is consistent with the finding in Section 2 and makes it clear that DNHs can be used to improve the process of isolating single emitters. We believe that this level of enhancement will allow for detecting and isolating single emitters at 1550 nm; however, improvements in the optical setup for that wavelength are required.

D.1.5 Time-to-Trap Analysis

We also measure the trapping time from the APD voltage for the different DNH cusp separations. The analysis of the trapping time has been done previously; [203, 204] here we show that the inverse of the trapping time has a similar dependence as the enhancement which we attribute to the larger trapping region with higher local field intensity.

Figure D.6 shows the trapping rate (inverse of trapping time, Γ) as a function of cusp separation size. The trapping time was measured from the APD voltage (Fig. D.1f) and the effect of DNH cusp separation on this factor was evaluated. With both the 16.9 nm and 26.2 nm nanocrystals, the trapping rate for the DNHs with 32 nm average cusp separation was also found to be much greater than other cusp separations. The uncertainty for the trapping time measurements was ± 2 ms. The trapping rate shown in this figure aligns closely with the emission enhancement seen in Fig. D.3, with both the fastest trapping and greatest emission enhancement occurring for the 32 nm cusp separation. The 16.9 nm nanocrystals were also trapped faster on

average than the 26.2 nm nanocrystals due to their smaller size and correspondingly lower Stokes' drag.

Considering possible differences in the diffusion of nanoparticles for each aperture, multiple experiments for each sample and aperture were performed. The measurements were performed for a minimum of four DNHs in each sample and the measurements were repeated three times for each DNH.

These results demonstrate that samples with more emission enhancement also experience faster trapping, and the intensity of the emission can show how fast a particle can be pulled into trapping. While the emission enhancement and trapping dynamics are separate physical processes, they can be related to one another. It should be noted that for the enhancement seen in this experiment, it is the square of the trapping rate that is related to the emission enhancement as the emission (at 650 nm) is a two-photon process.

In the case of trapping nanocrystals, greater emission enhancement corresponds to greater intensity on the sample to excite it. Having more intensity makes the trapping region larger so the particle needs to travel less distance to get into the trap, resulting in a faster trapping time. Thermophoretic forces may also be contributing to this effect as higher local field enhancement can cause additional heating at the structure which can attract thermophilic nanoparticles to the trap [175].

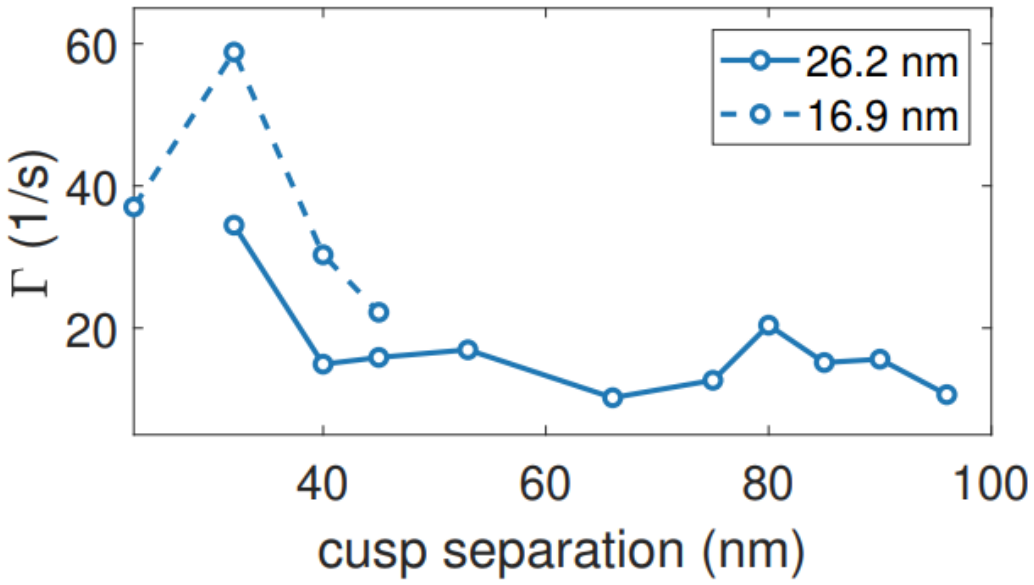

Figure D.6: Investigating the influence of the DNH cusp separation on trapping rate for 16.9 nm and 26.2 nm nanocrystals. Copyright 2021, AIP Publishing LLC.

D.1.6 Conclusion

In conclusion, we demonstrated that the plasmonic resonances of a DNH aperture in gold film can be tuned to further enhance the emission of erbium emitters compared to rectangular apertures. The greatest enhancement for Yb–Er-doped nanocrystals was found when using DNHs with 32 nm cusp separation. The emission of single nanocrystals at 400 nm and 1550 nm was also observed for the first time. Using this finding we demonstrated isolating $NaYF_4$ nanocrystals with single active Er^{3+} emitters as determined by the discrete levels of emission. The trapping rate for varying cusp separations was measured and was found to be fastest at the same separations that produced the greatest enhancement. The increased enhancement corresponding to the higher local field intensities increases the effective size of the trap, increasing the trapping rate and giving us an independent method to measure enhancement. These results show that DNHs can be tuned to significantly enhance emission, improving the method to reliably isolate single erbium emitters. This result can be applied to isolate and measure the characteristics of single erbium emitters at 1550 nm. It is a step towards deterministically isolating single-photon emitters for future single-photon sources at low-loss fiber optic wavelengths. This approach can also be used for looking at other properties of lanthanide based nanoparticles such as photon avalanche at the single particle level [205].

D.2 Appendix: Methods

Nanocrystal Synthesis and Characterization.

Chemicals. Yttrium(III) chloride hexahydrate (99.99%), erbium(III) chloride hexahydrate (99.995%), ytterbium (III) chloride hexahydrate (99.998%), ammonium fluoride (99.99%), tech grade oleic acid (90%), tech grade 1-octadecene (90%), and hexanes were purchased from Sigma-Aldrich. Anhydrous ethanol from Commercial Alcohols, methanol from Caledon, and sodium hydroxide from Bio Basic Canada inc. were used. All chemicals were used as received.

Characterization. Transmission electron microscopy images were obtained using a JEOL JEM-1400 microscope operating at 80 kV. Hexane dispersions of the NPs were drop-cast on a Formvar carbon-coated grid (300 mesh Cu) and air-dried before imaging. Size analysis of NCs from the images was performed digitally by measuring the surface area of at least 1000 particles with the program ImageJ (v. 1.52p) and calculating the corresponding diameter. X-ray diffractograms with a resolution of 0.0263 °2θ were collected using a PANalytical Empyrean X-ray System with a Cu source (Kα radiation, $\lambda = 1.54060$ Å) operating at 45 kV and 40 mA.

Synthesis (26.2 nm, $NaYF_4$: 18% Yb, 2% Er). To a 100 mL 3-neck roundbottom flask, 240.3 mg $YCl_3\bullet(H_2O)_6$, 77.8 mg $YbCl_3\bullet(H_2O)_6$ and 8.7 mg $ErCl_3\bullet(H_2O)_6$ were added together with 15 mL ODE and 5 mL oleic acid. The mixture was heated to 160 °C under vacuum and kept at that temperature for 30 minutes before cooling to

room temperature. Once cooled, a solution of 107 mg NaOH and 152 mg NH_4F in 10 mL MeOH was added dropwise while stirring. The mixture was heated to 65 °C 120 minutes to evaporate the MeOH. The temperature was then raised to 298 ∘C over 20 minutes (11.75 °C/min.) Temperature was kept at 305-307 °C for 90 minutes. The mixture was then cooled, washed with 30 mL EtOH, centrifuged at 1800 g for 10 min, and washed with 30 mL EtOH again before redispersion in 20 mL hexanes. TEM and XRD were performed.

Synthesis (16.9 nm $NaYF_4$: 18% Yb, 2% Er). To a 100 mL 3-neck roundbottom flask, 240 mg $YCl_3\bullet(H_2O)_6$, 80 mg $YbCl_3\bullet(H_2O)_6$ and 8 mg $ErCl_3\bullet(H_2O)_6$ were added together with 16 mL ODE and 5 mL oleic acid. The mixture was heated to 140 °C under vacuum and kept at that temperature for 60 minutes before cooling to room temperature. Once cooled, a solution of 102 mg NaOH and 150 mg NH_4F in 10 mL MeOH was added dropwise while stirring. The mixture was heated to 70 °C 120 minutes to evaporate the MeOH. The temperature was then raised to 280 °C. Temperature was kept at 280 °C for 135 minutes. The mixture was then cooled, washed with 30 mL EtOH, centrifuged at 1800 g for 10 min, and washed with 30 mL EtOH again before redispersion in 20 mL hexanes. The sample was then centrifuged again at 8694 g for 60 minutes and the sediment was redispersed in 10 mL hexanes. TEM and XRD were performed.

Synthesis ($NaYF_4$: 2.48 Er/NP). To a 100 mL 3-neck roundbottom flask, 300 mg $YCl_3\bullet(H_2O)_6$ and 0.3 mL 0.1×10^{-3} M $Er(OA)_3$ were added together with 16 mL

ODE and 5 mL oleic acid. The mixture was heated to 140 °C under vacuum and kept at that temperature for 60 minutes before cooling to room temperature. Once cooled, a solution of 102 mg NaOH and 150 mg NH_4F in 10 mL MeOH was added dropwise while stirring. The mixture was heated to 70 °C 120 minutes to evaporate the MeOH. The temperature was then raised to 280 °C. Temperature was kept at 280 °C for 135 minutes. The mixture was then cooled, washed with 30 mL EtOH, centrifuged at 1800 g for 10 min, and washed with 30 mL EtOH again before redispersion in 20 mL hexanes. TEM and XRD were performed.

DNH Apertures Fabrication.

Colloidal lithography was used to fabricate double nanohole apertures. Microscope slides were cleaned using plasma for 15 minutes and sonicated for 10 minutes in an ethanol bath. 30 L of 300 nm 0.01% w/v polystyrene spheres in ethanol drop-coated on the microscope slides uniformly. While the solution dries out through evaporation, the polystyrene spheres attach to the slides. The prepared slides were plasma etched with 5 to 15 seconds difference in etching time to get different cusp separation on each sample. Using 5 nm of titanium as an adhesive layer followed by 70 nm of gold, the samples were sputtered (MANTIS Sputtering System). The sputtered samples were sonicated for 1 minute in a toluene bath to remove polystyrene beads. SEM was performed.

Optical Trapping.

The optical tweezer setup (Fig. D.1d) consists of a single 980 nm continuous-wave

laser (JDS Uniphase SDLO-27-7552-160-LD) which is collimated, filtered, polarized, and expanded, before being focused on the sample with a 100× oil immersion microscope objective (1.25 numerical aperture). This single beam is used for both trapping, and to excite the nanocrystals. A 10× microscope objective is used to collect the light transmitted through the sample which is measured by an avalanche photodetector (Thorlabs APD120A). The polarization of the beam is set by the half-wave plate (HWP) and the linear polarizer (LP). A three-axis sample stage with piezoelectric adjustment aligns the apertures to the beam with 20 nm precision. A 750 nm short-pass filter (Thorlabs FES0750) reduces the trapping beam intensity and a bifurcated fiber splits the signal between two spectrometers, one for visible wavelengths (Ocean Optics QE65000) and one for NIR wavelengths (BaySpec NIRS-0900-1700). The gold DNH aperture samples were attached to #0 coverslips with an adhesive spacer containing 17.6 L of nanocrystals in hexane with concentrations of 1.3×10^{12} nanoparticles/cm^3, 5×10^{12} nanoparticles/cm^3, and 4×10^{12} nanoparticles/cm^3 for the 16.9 nm, 22.7 nm, and 26.2 nm nanocrystals.

Abbreviations used in Figure D.1d: APD, avalanche photodetector; BE, beam expander; CCD, charge-coupled device; D, dichroic mirrror; FM, flip mirror; HWP, half-wave plate; LP, linear polarizer; LPF, long-pass filter; Obj, objective lens; OD, optical density filter; S, spectrometer; SPF, short-pass filter.

Appendix E

Probing dark mode resonances of a gold nanorod

Using the circuit model for predicting the plasmonic resonances of a gold nanorod considering the end reflection was discussed in chapter two of this thesis. This model enables to calculate the field intensity profile around a gold nanorod at multiple resonances.

Figure E.1 shows the electric field profile around the nanorod for the first and second whole number resonance order. The diameter of the nanorod was 25 nm and its length was 119 nm. The Fabry-Perot model for the nanorod calculates the electric field profile along the cylinder. The average electric field amplitude at the interface of the cylinder and the sphere is calculated and it is assumed that the field inside the nanosphere is constant and equal to this value. Then, the field around

the nanosphere is obtained within the quasi-static approximation. In this model, the sphere is modeled as a dipole. The related dipole moment is obtained from Equation E.1 [192, 23].

$$\mathbf{p} = 4\pi\epsilon_0\epsilon_m a^3 \frac{\epsilon_d - \epsilon_m}{\epsilon_d + 2\epsilon_m} E_{avg} \tag{E.1}$$

E_{avg} is average field at the interface of the rod and the half sphere. The total field around the rod is calculated by adding the generated fields of the cylinder and the nanosphere. Figure E.1 (a) and (b) show the electric field profile of the first resonance from the model and FDTD results. The mesh size for FDTD simulation is 2 nm and a dipole source with range of 400-1500 nm is applied. The dipolar localized surface plasmon resonance can be resolved here. The dipolar LSPR is responsible for strong radiation. Figure E.1 (c) and (d) show multipolar LSPRs known as dark modes, obtained from the results of the model, and FDTD results, respectively. For dark mode resonances, the coupled energy is stored at the rod rather than coupling to the radiation [26].

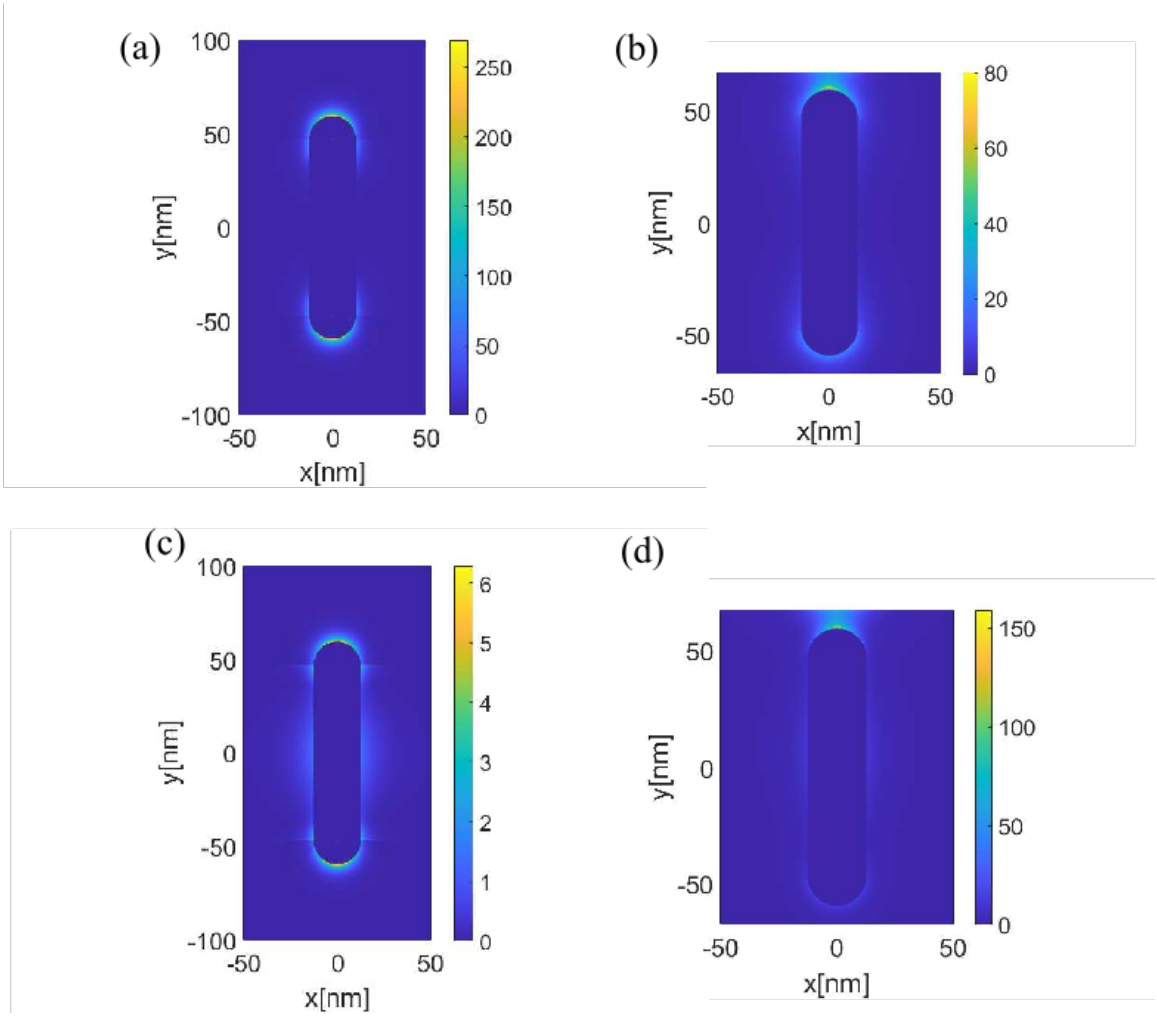

Figure E.1: (a) is the electric field from the model and (b) from the lumerical results around the nanorod at its bright mode resonance (m=1). (c) is electric field from the model and (d) from the lumerical results around the nanorod at its dark mode resonance (m=2).

Purcell factor calculation

Here we present a model to calculate the Purcell factor for the dark mode resonance of a nanorod. In this method, the Purcell factor is obtained by calculating the amount of power coupled to the dark mode resonance of the nanorod in comparison to the

power that is emitted to all free space modes by a dipole. The photon emission rate of the dipole can be obtained by dividing the dipole radiation power to the energy of each photon at the dark mode resonance frequency using Equation E.2.

$$\frac{\frac{c^2k^4}{12\pi}\sqrt{\frac{\mu_0}{\epsilon_0}}\frac{J^2}{\omega^2}}{\hbar\omega} = \frac{1}{\tau} \tag{E.2}$$

c is the speed of light in free space, k is the wave vector of light at the frequency of interest, J is the current density of the emitting dipole and τ is the relaxation time of the electrons from the excited energy state. The current density of the emitting dipole can be calculated if τ is known. We know τ is around 9 ms for an erbium atom at the emitting wavelength [206]. In order to obtain the coupled electric field of the dark mode resonance, Equation E.3 should be used for a nonmagnetic dispersive media [207].

$$\frac{\partial u_{eff}}{\partial t} + \nabla \cdot S = J \cdot E - \omega_0\epsilon_0\epsilon_i E^2 \tag{E.3}$$

$$u_{eff} = \frac{1}{2}Re[\frac{d(\omega\epsilon)}{d(\omega)}(\omega_0)]E^2 + \frac{1}{2}Re[\frac{d(\omega\mu)}{d(\omega)}(\omega_0)]H^2 \tag{E.4}$$

u_{eff} is the effective electromagnetic energy density, S is the Poynting vector, and ϵ_i is the imaginary part of the relative permittivity of gold. Since the energy flow out of the cavity is almost negligible due to the nature of the dark mode resonances [26],

$\nabla \cdot S$ term is absent. The effective electromagnetic energy density of the cavity does not change with time after it reaches the steady state. Then, the coupled electric field of the dark mode resonance can be obtained using Equation E.5 knowing that coupling power to the dark mode is equal to the loss power in that mode of the nanorod.

$$\int J.E_m dV = \int \omega_0 \epsilon_0 \epsilon_i {E_m}^2 dV \tag{E.5}$$

E_m is the electric field coupled to the dark mode.

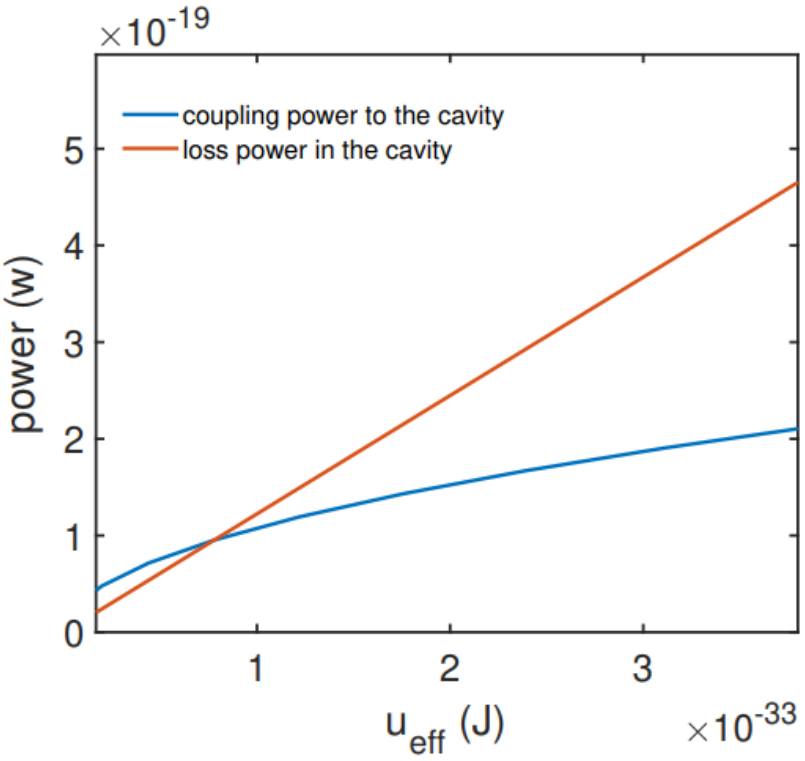

Figure E.2: Power coupled to the nanorod cavity and the loss power realted to dispersive media in the nanorod normalized to effective electromagnetic energy denisty in the nanorod cavity.

Figure E.2 shows the coupled power to the nanorod cavity associated with the dipole emitter 20 nm away from the tip of the nanorod and the loss power in the dispersive gold nanorod obtained from the left hand side and right hand side of Equation E.5, versus the stored energy in the cavity using Equation E.4.

It is also required to determine the electric field coupled to all free space modes. This can be calculated using Equation E.6 which shows the dipole radiation power [207] equals to the power of the same dipole coupled to all possible modes in free space.

$$\int J.E_{fs}dV = \int \frac{C^2k^4}{12\pi}\sqrt{\frac{\mu_0}{\epsilon_0}}\frac{J^2}{\omega^2}dV \tag{E.6}$$

E_{fs} is the electric field coupled to the free space mode. Equation E.7 calculates the Purcell factor for the dark mode of the nanorod using the power coupled to the dark mode resonance and the power coupled to free space obtained from Equation E.5 and Equation E.6.

$$Purcell factor = \frac{\int J.E_m dV}{\int J.E_{fs}dV} \tag{E.7}$$

The calculated Purcell factor using this method for an erbium atom 20 nm away from the tip of the nanorod at the dark mode resonance (652 nm) is 34.

To validate the method used in this research, the FDTD software, Lumerical is used. It is shown that placing an emitter near a resonant cavity can alter its spontaneous emission with a factor of $\frac{Q}{V}$ [208]. Calculating the Purcell factor for the

nanorod scheme can diverge since the volume of interest is uncertain. An alternative approach is obtaining the local density of states using Green's function calculations.

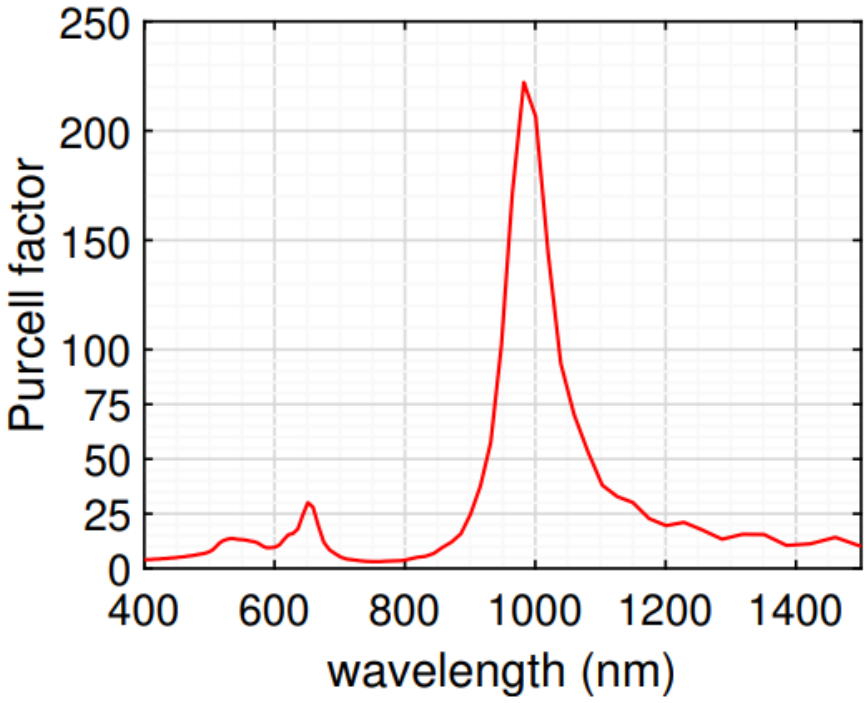

Figure E.3: Purcell factor obtained using Green's functions.

Figure E.3 shows a FDTD simulation results for the Purcell factor obtained by calculating the partial density of local states (PDLS) of an erbium atom as an emitting dipole. The dipole source is placed 20 nm away from the tip of along the long axis of the nanorod. A 2 nm uniform mesh is chosen for the FDTD calucaltions. Figure E.3(a) shows the increase of the Purcell factor at 980 nm and 651 nm with the presence of a gold nanorod acting as a resonant cavity. The peak at 980 nm is associated with the bright mode of the nanorod. There is also a peak in the Purcell factor spectrum at 652 nm related to the dark mode resonance of the nanorod. The

Purcell factors obtained from this method are 30 and 222 for the dark and bright mode resonances, respectively. There is a good agreement between the results obtained from our model and the results from FDTD simulations at the dark mode resonance.

In conclusion, This method is able to predict Purcell factor for the dark mode resonances of a gold nanorod. Developing this technique to predict bright mode resonance can be promising to have a model that can calculate all resonances of a nanorod; at the same time, avoid time consuming FDTD simulations.